ATOMISTIC SIMULATION STUDIES OF NICKEL AND COBALT DOPED MANGANESE-BASED CATHODE MATERIALS

By

Nkgaphe Tebatjo Tsebesebe

DISSERTATION

Submitted in fulfilment of the requirements for the degree of

Master of Science (MSc)

in

Physics

in the

Faculty of Science and Agriculture,

(School of Physical and Mineral Sciences)

at the

UNIVERSITY OF LIMPOPO

SUPERVISOR: Dr R. S. LEDWABA

Co-SUPERVISOR: Prof P. E. NGOEPE

2021

Declaration

I declare that the dissertation hereby submitted to the University of Limpopo, for the degree of masters in Physics has not previously been submitted by me for a degree at this or any other University; that it is my work in design and execution, and that all material contained herein has been duly acknowledged.

_____. 10/04/2021

TSEBESEBE N.T Date

Abstract

The stead-fast demand for sustainable lithium-ion batteries (LIB) with competitive electrochemical properties, safety, reduced costs, and long-life cycle, calls for intensive efforts towards the development of new battery cathode materials. The layered transition metal oxides formulated $LiMO_2$ (M: Mn, Ni and Co) have attracted considerable attention due to their capability to optimize the discharge capacity, cycling rate, electrochemical stability and lifetime. The transition metals Mn, Ni and Co (NMC) have been reported to contribute towards enhancement of the performance of NMC based lithium-ion batteries.

In this work, the electronic properties of transition metal oxides $LiMO_2$ (M: Mn, Ni and Co) as individual crystal structures are studied using density functional theory (DFT+U) in the local density and generalized gradient approximation (LDA and GGA). The Hubbard U values together with the low spin transition metal in 3+ charge state (Mn^{3+}, Ni^{3+} and Co^{3+}) predicts the electrical conductivity of the materials. The conductivity is associated predominantly with 3d states of the transition metals (Mn, Ni and Co) and 2d character in oxygen. The $LiNiO_2$ material is high in conductivity, while both $LiMnO_2$ and $LiCoO_2$ are low in electrical conductivity. All independent elastic constants satisfy the mechanical stability criterion of orthorhombic materials implying stability of the materials. However, the phonon dispersion curves display imaginary vibration along high symmetry direction for $LiCoO_2$. The heats of formations predict that the $LiNiO_2$ is the most thermodynamically stable material while the $LiMnO_2$ is the least thermodynamically stable material.

The derived interatomic potentials produced NiO and CoO structures with a difference of less than 1% and 9% respectively, from the experimental structures. The structures were melted at temperatures close to their experimental values from molecular dynamics. The radial distribution curves and Nano architectures presented the melting point of NiO and CoO at 2250K and 2000K respectively. All independent elastic constants satisfy the mechanical stability criterion of cubic materials implying stability of the materials. The high electrical conductivity and thermodynamic favourability $LiNiO_2$ suggests that the material can be the most recommendable material as a cathode material and further improved through doping. This will add the overall enhancement of the electrochemical performance while stabilizing structural stability of the cathode material in high energy density Li-ion batteries.

Acknowledgements

I would like to direct my gratitude to all mighty God to have made this project to be a success, my family for their never-ending support, my supervisors Prof. E. Ngoepe, Dr. RS Ledwaba and K.M Kgatwane for their insightful research assistance, the materials modelling team for their help. This project was carried out at the University of Limpopo Materials Modelling Centre. The Centre for High-Performance Computing (CHPC) is being appreciated for the resources and the National Research Foundation (NRF) is highly appreciated for funding this project.

Table of Contents

Declaration i

Abstract ii

Acknowledgements iii

Table of Contents iv

List of Figures ix

List of Tables xi

Chapter 1: Introduction and Background 1

1.1. General Background 1

1.1.1. Brief Description of a Battery 2

1.1.2. Operation of Lithium-ion Batteries 3

1.1.3. Examples of Applications of Lithium-ion Batteries 4

1.2. Structural Properties 4

1.2.1. $LiMnO_2$ Structure 6

1.2.2. $LiCoO_2$ Structure 7

1.2.3. $LiNiO_2$ Structure 7

1.3. Literature Review 7

1.3.1. Doping the Lithium Transition Metal Oxides 9

1.3.2. Structural Parameters 10

1.3.3. Band Gaps 11

1.3.4. Magnetic and Electronic Properties 12

1.3.5. Challenges Encountered in Other Studies 13

1.4. The rationale of the Study 14

1.4.1. Research Questions 14

1.4.2. Aims 15

1.4.3. Objectives 15

1.4.4. Overview of the study 16

1.5. Outline of the Study 17

Chapter 2: Research Methodology 19

2.1 Computer Modelling 19

2.2 Energy Minimization 21

2.3 Ab Initio 22

2.4 Density Functional Theory 23

2.5 Molecular Dynamics 26

2.5.1 Aims of Molecular Dynamics 27

2.5.2 The Molecular Dynamic Approach is as Follows 27

2.5.3 Force Field 28

2.5.4 Limitations 28

2.5.5 Molecular Dynamics Ensembles 29

(i) Micro Canonical (NVE) Ensemble 29

(ii) Canonical (NVT) Ensemble 29

(iii) Isothermal–isobaric ensemble (NPT) 29

2.5.6 Molecular Dynamics Properties 29

(i) The Temperature 30

(a) Melting Temperature (Tm) 30

(ii) Radial Distribution Function (RDFs) 31

(iii) Diffusion Coefficients 32

2.6 The Potential Model 33

2.6.1 Born Model of Solids 33

(i) Long-Range Interactions 33

(a) Ewald Summation 34

(ii) Short Range Interactions 34

(a) Buckingham potential 35

2.7. Simulation codes 36

2.7.1. GULP 36
2.7.2. DL_POLY 36
(i) INPUT FILES 36
(ii) OUTPUT FILES 37
2.8 Approximation Methods 37
2.8.1 Local Density Approximation 38
2.8.2 Generalised Gradient Approximation 40
2.9. Plane-wave Pseudopotential 41
2.9.1 Plane-wave Basis Sets 42
2.9.2 Pseudopotentials 43
(i) Norm-conserving Pseudopotentials 45
(ii) Ultrasoft Pseudopotentials 45
2.10. Implementation of Plane-wave Pseudopotential Codes 46
2.11. Theoretical Background of the Calculated Properties 47
2.11.1 Heats of Formations 47
2.11.2 Density of States 47
2.11.3 Phonon Dispersion Curves 48
2.11.4 Elasticity 49
(i) Elastic Stability Criteria 51
Chapter 3: Structural, Electronic and Vibrational Properties of $LiMO_2$ (M: Mn, Ni and Co) 53
3.1 Introduction 53
3.2 Structural Properties of $LiMO_2$ (M: Mn, Ni and Co) 54
3.3 Method 55
3.3.1 Convergence Test 55
(i) Kinetic Energy Cut-off 55
(ii) K-Points 56

3.4 Results 57
3.4.1 Geometry Optimization 57
3.4.2 Derivation of Hubbard U Parameters 58
3.4.3 Structural Properties of $LiMO_2$ (M: Mn, Ni and Co) 59
(i) $LiMnO_2$ 59
(ii) $LiNiO_2$ 60
(iii) $LiCoO_2$ 61
3.4.4 Electronic Properties 62
3.4.5 Band Structures 63
3.4.6 Density of States 65
(i) The density of States for $LiMnO_2$ 66
(ii) The density of States for $LiNiO_2$ 66
(iii) The density of States for $LiCoO_2$ 67
3.4.7 Mechanical Stability 68
(i) Phonon Dispersion Curves for $LiMnO_2$, $LiNiO_2$, and $LiCoO_2$ 69
(ii) Elastic Properties 70
(iii) Total Density of States 73
3.5 Discussion 74
Chapter 4: Derivation and Validation of Interatomic Potentials for NiO and CoO 76
4.1 Introduction 76
4.2 Procedure 77
4.3 Structural Properties of NiO and CoO 77
4.4 Derivation of Interatomic Potentials 79
4.4.1 Introduction 79
4.5 Results 79
4.6 Validation of the Interatomic Potentials 81

4.6.1 Comparison Between Calculated and Experimental Results 81
4.7 MD Study of NiO and CoO Using the Derived Potentials 83
4.7.1 NiO Bulk Structure 83
4.7.2 CoO Bulk Structure 85
4.8 Radial Distribution Function 87
4.8.1 NiO Structure 88
4.8.2 CoO Structure 89
4.9 Discussion 91
Chapter 5: Summary and Conclusions 93
References 96

List of Figures

Figure 1.1 The charge and discharge mechanism of the rechargeable lithium-ion batteries……..……..3
Figure 1.2 Representation of lithium-ion batteries' applications……...4
Figure 1.3 Structural representation of (a) $LiMnO_2$, (b) $LiNiO_2$, and (c) $LiCoO_2$ bulk in $R\bar{3}m$ space group……..…….6
Figure 1.4 A bandgap diagram showing the different sizes of band gaps for conductors, semiconductors, and insulators ……...11

Figure 2.1 The steps in ved in developing a simulation model, designing a simulation experiment, and performing simulation analysis……...20
Figure 2.2 Schematic representation of simulation and experimental studies……....21
Figure 2.3 The schematic representation of computational energy minimisation procedure…….……..22
Figure 2.4 A comparison of the methodology for solving the many-body Schrodinger equation and effective one-electron Kohn-Sham equation……...……..…26

Figure 2.5 The graphical (a) and schematic (b) representation of radial distribution function (RDF)……...……...32

Figure 2.6 Schematic representation of DL_POLY input and output files…..…..…...37

Figure 2.7 Schematic representation of an atomic all-electron wave function and the corresponding atomic pseudo wave functions……..……..….45

Figure 3.1 (a) The 3D layered parent bulk of $LiMO_2$ (M: Mn, Ni and Co) with Bravais lattice of rhombohedral cantered hexagonal and (b) magnification representation of co-ordinated sites for $LiMO_2$ (M: Mn, Ni and Co).....54
Figure 3.2 Graphical representation of total energy per atom versus kinetic cut-off energy of (a) $LiMnO_2$, (b) $LiNiO_2$ and (C) $LiCoO_2$……..57
Figure 3.3 Graphical representation of final energy versus k-points for (a) $LiMnO_2$, (b) $LiNiO_2$ and (c) $LiCoO_2$……...57
Figure 3.4 Graphical representation of band structures for (a) $LiMnO_2$, (b) $LiNiO_2$ and (c) $LiCoO_2$ material with low spin state…….……....65
Figure 3.5 Graphical representation of the total and partial density of states for (a) $LiMnO_2$, (b) $LiNiO_2$, and (c) $LiCoO_2$……..…..70

Figure 3.6 The graphic representation of phonon dispersions for (a) $LiMnO_2$, (b) $LiNiO_2$, and (c) $LiCoO_2$……70
Figure 3.7 The comparisons of the total density of states……...73
Figure 4.1 Body-cantered cubic unit cells of (a) NiO and (b) CoO……78
Figure 4.2 Representation of molecular dynamics results with the derived interatomic potentials in different temperatures. (a) NiO structure with 20 000 atoms in a crystalline form (before the melting point), (b) the structure at the melting temperature, and (c) the amorphous structures (after melting point).....84
Figure 4.3 Energy vs temperature plot for NiO structure……85
Figure 4.4 Representation of molecular dynamics results when run with the derived interatomic potentials in different temperatures. (a - c) CoO structure with 20 000 atoms at different temperatures. (a) the CoO structure with signs of state change (melting), (b) C CoO structures in an amorphized state, and (c) the amorphous structures (after melting point).....86
Figure 4.5 Energy vs temperature plots for CoO structure……87
Figure 4.6 representation of the radial distribution curves for NiO in the crystalline state (a) and the snapshot of the bulk structure (b), the redial distribution function curves for NiO in amorphous forms and (d) its bulk structure……88
Figure 4.7 The radial distribution function curves for NiO under different temperatures; and the magnified portion on the top right corner……...89
Figure 4.8 representation of the radial distribution curves for CoO in the crystalline state (a) and the snapshot of the bulk structure (b), the redial distribution function curves for CoO in amorphous forms and (d) its bulk structure……...90
Figure 4.9 The radial distribution function curves for CoO under different temperatures; and the zoomed portion on the top right corner……..……..91

List of Tables

Table 1.1 Lattice parameters and ume of $LiMO_2$ (M: Mn, Ni, and Co).....5
Table 1.2 Fractional coordinates and atomic positions of $LiMO_2$ (M: Mn, Ni, and Co) 5
Table 2.1 Critical k-points in the first Brillouin zone……...49
Table 3.1 Structural properties of $LiMO_2$ (M: Mn, Ni, and Co).....53
Table 3.2 Fractional coordinates and atomic positions of $LiMO_2$ (M: Mn, Ni, and Co)55
Table 3.3 The parameters for optimised structures……..58
Table 3.4 Representation of Hubbard U parameters per transition metal…….59
Table 3.5 Calculated and experimental lattice parameters, volume and heats of formation for orthorhombic $LiMnO_2$……..……..……60
Table 3.6 Calculated and experimental lattice parameters, volume and heats of formation for orthorhombic $LiNiO_2$……..61
Table 3.7 Calculated and experimental lattice parameters, volume and heats of formation for orthorhombic $LiCoO_2$…….……..….61
Table 3.8 The comparisons of simulated and experimental band gaps (eV) using the density functional theory…….…….63
Table 3.9 the elastic constants (C_{ij}), bulk (B), and Young's (E) moduli of $LiMnO_2$, $LiNiO_2$, and $LiCoO_2$. The experimental values are represented in brackets…..…..…72
Table 4.1 Structural properties of NiO……..78
Table 4.2 Structural properties of CoO…….……....79
Table 4.3 The derived Buckingham interatomic potentials for NiO……...……..80
Table 4.4 The derived Buckingham interatomic potentials for CoO.…….……..…80
Table 4.5 The partial charges used in deriving the interatomic potentials……...80
Table 4.6 The calculated elastic properties and bulk modulus NiO……...81
Table 4.7 The calculated elastic properties and bulk modulus for CoO……....81
Table 4.8 Comparison of initial and final parameters generated from the derived interatomic potentials in NiO……..……..82
Table 4.9 Comparison of initial and final parameters generated from the derived interatomic potentials in CoO……..….82

Table 4.10 Comparison of experimental and derive elastic constants and bulk modulus for NiO……..……...82
Table 4.11 Comparison of experimental and derive elastic constants and bulk modulus for CoO…….……..83
Table 4.12 Comparisons of the melting temperatures for NiO structure……...84
Table 4.13 Comparisons of the melting temperatures for CoO structure……..86

Chapter 1: Introduction and Background

This chapter contains a detailed introduction to the research work, the background and the purpose of this work. The structural description and literature review of cathode materials being studied will be highlighted. Moreover, the objectives as well as the significance of this study are herein discussed.

1.1. General Background

The popularization of portable electronics and electric vehicles worldwide stimulates the development of energy storage devices, such as batteries which significantly depends upon the advancement of new materials used in these devices [1]. To achieve global clean and sustainable energy, a transformation of energy production and storage technologies is required. Hence, the discovery and optimisation of high-performance materials are critical to future breakthroughs for the next generation of rechargeable batteries. These advances depend on exploring new classes of compounds and gaining a better understanding of the fundamental science of functional materials that underpin applied research [2]. Rechargeable lithium-ion batteries have emerged as the dominant energy storage source for consumer electronics, automotive, and stationary storage applications, due to their high energy density in contrast to all other secondary batteries [2].

The lithium element tarnishes and oxidizes rapidly. Moreover, it reacts easily to water. However, the lithium element does not occur freely in nature; As such, the element has the highest specific heat of any solid element and is mainly used in heat transfer applications. Hence, many recent studies have carried out various methods to estimate whether lithium production can meet increasing demand, particularly in the transportation sector where lithium-ion batteries are the technology of interest for electric vehicles [2].

Lithium-ion batteries are multi-component devices, with performance that has been reported to be significantly enhanced by restructuring the cathodes of the batteries from various materials [3]. As such layered materials have surfaced as a very promising family of materials [17, 18, 19]. However, the limiting factor of energy contents in Lithium-ion batteries is the cathode materials of the batteries. The positive electrode (cathode) plays a key role in the capacity, safety, and cycle life of the

batteries [4, 5]. That is, a lithium-ion battery with a Li metal oxide-based cathode and carbon-based anode which can exhibit a capacity of greater than 270mAh/gram (~1 electron per metal utilization of material) with little or no capacity fade for hundreds of discharge/charge cycles is of great interest [5]. As such, mixing different transition metals (TM) in layered materials can be beneficial [13, 14] for improving these battery materials. For instance, in Ni-Co-Mn layered materials, Ni has been reported to provide favourable capacity, Co improves kinetics and Mn stability [15, 16].

The transition metal oxides layered type cathodes have been attracting considerable attention to serve as a cathode material for Li-ion batteries due to their capability to optimize the capacity, cyclic rate, electrochemical stability, and lifetime [6, 7]. As such, more intense studies have been carried out with the $Li_xNi_yMn_zO_2$ (x+y+z=1) compound being the state-of-art choice in the cathode materials for the ideal batteries. This compound incorporates characters of Mn, Ni and Co (NMC) transition metals, to improve the electrochemical performance while reducing the material cost [8, 9]. Moreover, the NMC rich compositions demonstrate high discharge capacity, maintain a better life cycle and thermal safety, and provide excellent rate capacity, respectively [8].

1.1.1. Brief Description of a Battery

A battery is a device that converts chemical energy into electrical energy utilizing an electrochemical reaction called oxidation-reduction (redox). It is composed of one or more cells (basic electrochemical units), each containing a positive electrode (cathode; electrode being reduced), a negative electrode (anode; electrode undergoing oxidation), a separator and an electrolyte. The cells are divided into two major classes, namely: primary and secondary. Primary cells are not rechargeable and must be replaced once the reactants are depleted. However, the secondary cells are rechargeable and require a direct current charging source to restore reactants to their fully charged state [10]. The voltage rating is based on the number of cells connected in series and the nominal voltage of each. The ampere-hour (Ah) capacity available from a fully charged battery depends on its temperature, rate of discharge, and age. Moreover, the maximum power available from a battery depends on its internal construction [10].

Lithium-ion battery is constructed by connected basic lithium-ion cells in parallel (to increase current), in series (to increase voltage) or combined configurations. A basic lithium-ion cell consists of a cathode (positive electrode) and an anode (negative electrode). These electrodes are contacted by an electrolyte containing lithium ions, and they are being isolated from each other by a separator (typically microporous polymer membrane) that allows the exchange of lithium ions between the two electrodes but not electrons. Figure 1.1 is the illustration of a basic operating principle of a typical lithium-ion battery cell. Consequently, the lithium-ion technology as the root in secondary lithium-ion batteries give rise to high power, high capacity, high charging rate, long life, improved safety, performance, and low-cost batteries [10].

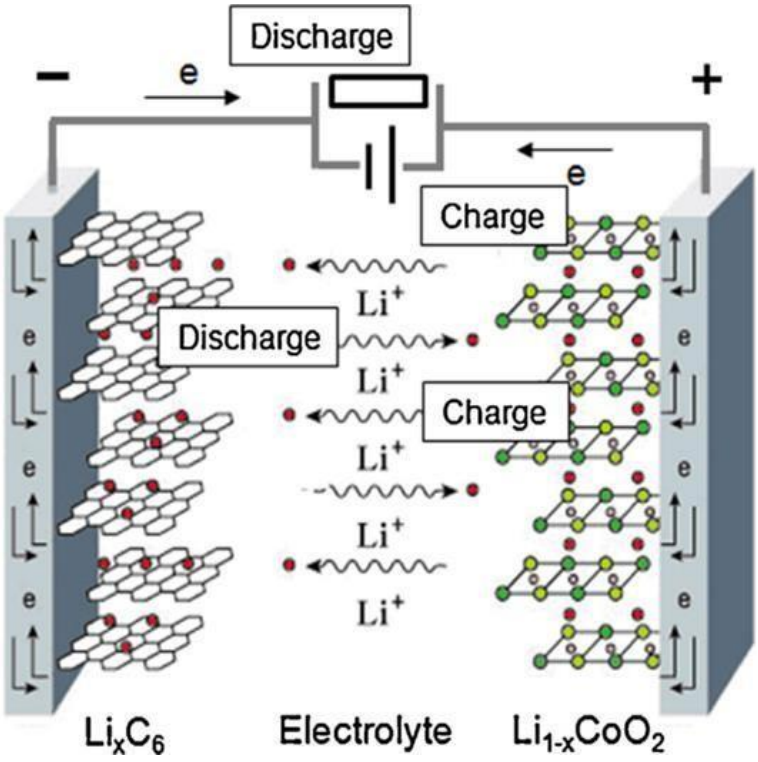

Figure 1.1 The charge and discharge mechanism of the rechargeable lithium-ion batteries [5].

1.1.2. Operation of Lithium-ion Batteries

The commercial cells of the lithium-ion batteries are typically assembled in a discharged state where the discharged cathode materials (e.g., $LiCoO_2$) and anode materials (e.g., carbon) are stable in the atmosphere [11]. During the charging process, the two electrodes are connected externally to an external electrical supply. The electrons are forced to be released at the cathode and move externally to the anode. Simultaneously the lithium ions move in the same direction, but internally, from

cathode to anode through the electrolyte. In this way, the external energy is electrochemically stored in the battery in the form of chemical energy in the anode and cathode materials with different chemical potentials [11]. The opposite occurs during the discharging process, where the electrons move from anode to the cathode through the external load to do work, and Li ions move from anode to the cathode in the electrolyte [11]. The charge and discharge mechanism of the rechargeable lithium-ion batteries are shown in figure 1.1.

1.1.3. Examples of Applications of Lithium-ion Batteries

As another type of power source, lithium-ion batteries (LIBs) have received significant attention. As such the applications for lithium-ion batteries have currently expanded to a broader field such as electric vehicles and stationary energy storages. Moreover, the high specific capacity and relatively low cost of the batteries has made a breakthrough in electric transportation, such as plug-in hybrid electric vehicles (PHEVs) [12]. The typical representation of the lithium-ion batteries applications is depicted in figure 1.2.

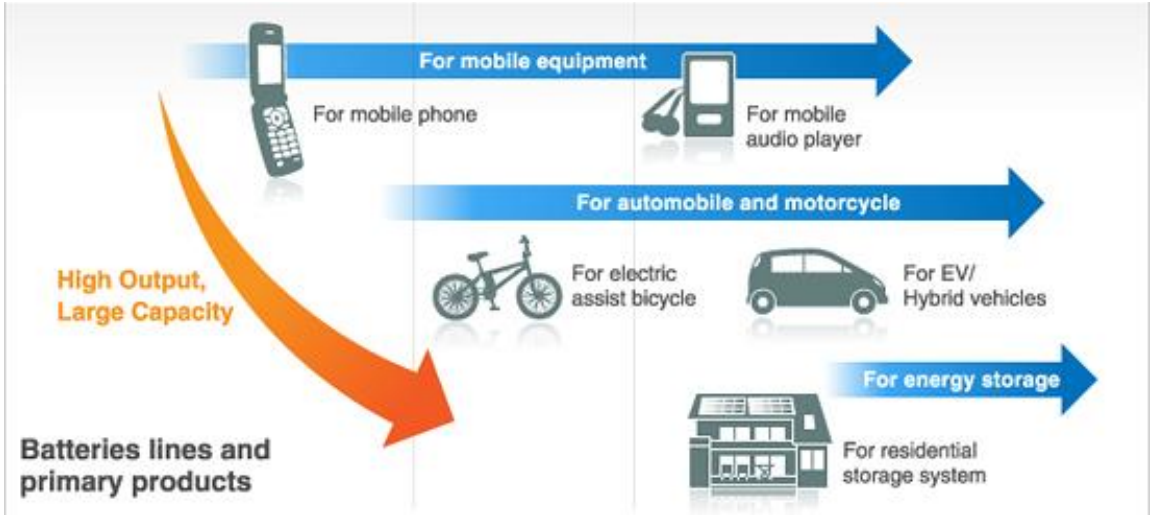

Figure 1.2 Representation of lithium-ion batteries' applications [12]**.**

1.2. Structural Properties

The structures of $LiTMO_2$ consists of a hexagonal sodium iron dioxide (α-$NaFeO_2$) ($R\bar{3}m$) cathode material containing lithium, oxygen and transition metals (TMs: manganese, nickel, and cobalt) wherein TMs occupy alternating atomic layers and transition metal elements residing at the centre of the oxygen octahedron [8]. The $LiMO_2$ (M=3d transition metal) crystal structures can also be described as different

ordered superstructure arrangements of the Li and M cations on the $LiMO_2$ (M= Mn, Ni, and Co) parent rock salt lattice [13]. The crystal structures of the materials have oxygen atoms in the close-packed FCC, and the cations filling all the octahedral interpositions in support of known active $LiMO_2$ cathode materials. Moreover, the structures have an ordered cation, where the cations are arranged in an ordered superstructure that provides tunnels to allow the deintercalation and re-intercalation of lithium atoms. The unit cells of the $LiMO_2$ (M: Mn, Ni, and Co) is illustrated in figure 1.3 below. The structural properties of the structures are tabulated in table 1.1, and the vectors that describe the positions of atomic nuclei within the crystal structure are illustrated in table 1.2.

Table 1.1 Lattice parameters and volume of $LiMO_2$ (M: Mn, Ni, and Co) [138]

Structures	**Lattice parameters**				**Volume ($Å^3$)**
	a(Å)	**b(Å)**	**c (Å)**	**z**	
$LiMnO_2$	3.00	3.00	14.55	0.256	105.35
$LiNiO_2$	2.88	2.88	14.20	0.256	102.06
$LiCoO_2$	2.80	2.80	14.12	0.26	96.47

Table 1.2 Fractional coordinates and atomic positions of $LiMO_2$ (M: Mn, Ni, and Co) [190]

Atoms	**Positions**	**x**	**y**	**z**
Li	3b	0	0	1/2
Mn	3a	0	0	0
Ni	3a	0	0	0
Co	3a	0	0	0
O	6c	0	0	0.2584

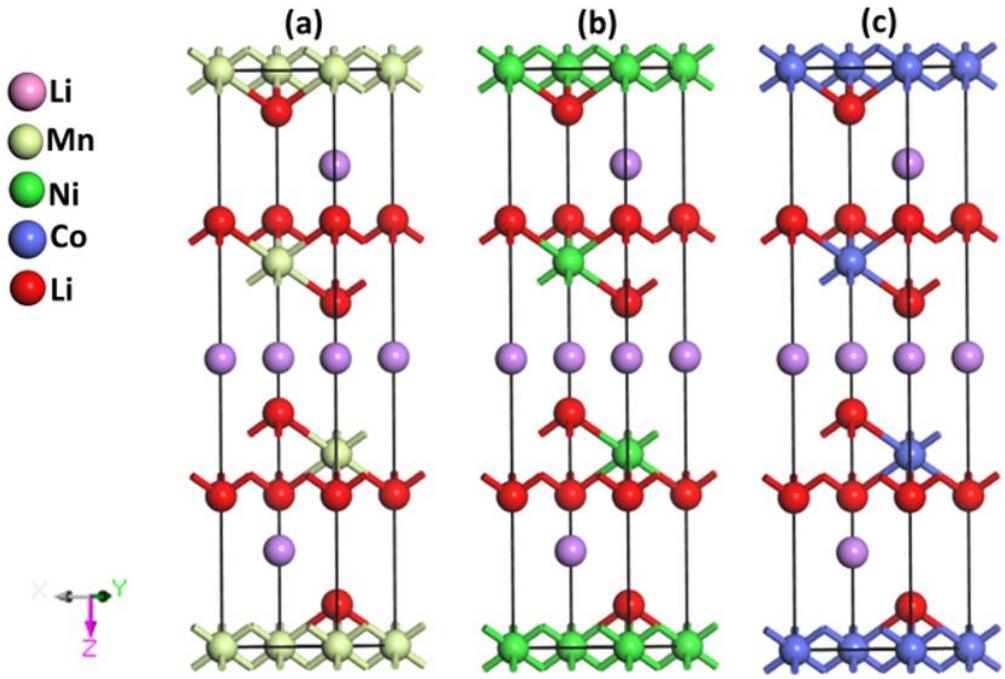

Figure 1.3 Structural representation of (a) $LiMnO_2$, (b) $LiNiO_2$, and (c) $LiCoO_2$ bulk in $R\bar{3}m$ space group

1.2.1. $LiMnO_2$ Structure

The $LiMnO_2$ structure has two competing ordered-rock salt structures, that are orthorhombic $LiMnO_2$ (o-$LiMnO_2$, $Pmnm$) and monoclinic $LiMnO_2$ (m-$LiMnO_2$, $C2/m$). The o-$LiMnO_2$ has an ordered-rock salt structure in which MnO_6 and LiO_6 octahedral are arranged in corrugated layers. The m-$LiMnO_2$ has a cation ordering structure in which Li ions are located in the layers of O_h sites between MnO_2 sheets [14]. In the absence of a Jahn Teller (JT) effect, the $LiMnO_2$ is expected to be stable in the α-$NaFeO_2$ structure (space group $R\bar{3}m$) [15]. Conversely, when the cooperative JT distortion is introduced by Mn^{3+} ($t_{2g}^3e_g^1$), the symmetry is reduced; to monoclinic ($C2/m$). The m-$LiMnO_2$ is relatively unstable compared to the o-$LiMnO_2$, which is attributed to the collective distortion of the octahedron in the corrugated-layer structure reducing the elastic energy and its 3d spin ordering caused by the interaction between these moments [16, 17].

The o-$LiMnO_2$ is synthesised by high-temperature methods [18], while the undoped m-$LiMnO_2$ has only been prepared by metastable synthesis and hydrothermal reaction [18]. However, the doped $LiMnO_2$ has been produced in the monoclinic

phase, such as the $LiAl_xMn_{1-x}O_2$ which is attributed to the non-JT effect of Al^{3+} [19]. The properties of $LiMnO_2$ structures used in this work are illustrated in table 1.1 above.

1.2.2. $LiCoO_2$ Structure

The $LiCoO_2$ structure exhibits two forms, a hexagonal structure, and a cubic structure, which are the low temperature (LT-$LiCoO_2$)-cubic form, and high temperature (HT-$LiCoO_2$) - hexagonal form. The hexagonal and cubic structures are based on the same oxide sublattice, and they are distinguished by the spatial arrangement of cations. The structure of LT-$LiCoO_2$ is not ideally layered, and 6% of the cobalt ions reside in the octahedral (8a) sites of the lithium layers. LT-$LiCoO_2$ adopts a spinel relate structure (space group $Fd3m$) based on a cubic closed packed oxygen network with alternating cation layers of 0.75 Co, 0.25 Li, 0.75 Li, and 0.25 Co composition perpendicular to each of the four cubics [111] direction. The aspect ratio of the spinel (c/a in the range 4.900–4.914) is close to that of the ideal cubic close packing oxygen array (c/a = 4.899) [20]. The structure of HT-$LiCoO_2$ belongs to the trigonal system (space group $R\bar{3}m$, O3 phase) in which Co and Li planes alternate in the ABCABC oxygen stacking. The value of c/a ratio is in the range of 4.98–5.00 and is significantly larger than that of an ideal cubic closed packed lattice (c/a = 4.899) [20]. The properties of $LiCoO_2$ structures used in this work are illustrated in table 1.1 above.

1.2.3. $LiNiO_2$ Structure

$LiNiO_2$ is isostructural with $LiCoO_2$, which crystallizes with a rhombohedral layered rock-salt structure. Metal ions occupy the octahedral sites of a cubic close-packed network of oxygen ions to form alternate ordered layers of Li and Ni ions parallel to the (111) plane of the cubic rock-salt structure [21]. The lithium nickel oxide ($LiNiO_2$) has octahedron slaps formed by cobalt and oxygen atoms. Moreover, it is composed of lithium layers lying between the slaps where each oxygen in the slap coordinates both lithium and cobalt in an octahedral fashion [22]. The edge-sharing octahedrons have direct metal-metal interaction properties with a 90° angle amongst metal-oxygen-metal interactions tilted relative to the layered structure [22]. The properties of $LiNiO_2$ structures used in this work are illustrated in table 1.1 above.

1.3. Literature Review

A wide range of studies have been conducted on the layered lithium mixed metal oxides $LiMO_2$ (M=Mn, Co, Ni) cathodes and much of the focus was on the structural

and electronic properties. The $LiNi_{0.33}Mn_{0.33}Co_{0.33}O_2$ was first proposed by Ohzuku et al. in 2001 [23]. Lee et al. in 2004 [24, 25] performed a synthesis optimization on the material in a similar DFT+u study. They reported high discharge capacity, good cycling ability and excellent thermal stability. It was later reported that at high current density, the rate capability and cycling performance were not satisfactory. The radius of the ions Ni^{2+} (0.63 Å) and Li^{+} (0.76 Å) [26], causes cation mixing and as a result, degrade the electrochemical performance of the material. The drawbacks of the material have reportedly been due to the nature and the reactions in the structures forming up the doped material.

Similarly, a first-principles study was conducted on the electrochemical, thermal and mechanical properties of the material and reported that the material has a maximum theoretical specific energy (high capacity and high voltage) which yields a good electrochemical performance [22]. Furthermore, the $LiCoO_2$ depicted a stable capacity during different cycles. However, the cobalt (Co) has been classified as being toxic and reported to be more reactive due to its state of being thermodynamically unstable [27, 22] at higher temperature operation (>130 °C) or during overcharging. That is, the $LiCoO_2$ decomposition generates oxygen which as a result reacts exothermally with the organic materials in the cell.

On the other hand, previous studies on Jahn–Teller Distortion in lithium nickel oxide ($LiNiO_2$) delineated that the material crystallizes with rhombohedral layered rock-salt structure with alternate ordered layers of Li and Ni ions parallel to the (111) plane of the cubic rock-salt structure formed by the metal ions occupying the octahedral sites of the cubic closed packed network of oxygen [28]. The Ni atom in the compound is located at the 3b site of the $R\bar{3}m$ lattice with six oxygen atoms at equal Ni-O distances [28]. The compound has been reported to have a higher initial capacity (200 mAh/g) and more adventitiously its value is relatively low [27]. However, the material has been reported to suffer from poor cyclability and low reversible capacity. As a result, this makes it more difficult to synthesize it as a cathode material due to the Jahn-Teller (JT) effect of active Ni^{3+} ions in the lattice, which causes the poor structural stability of the $LiNiO_2$ [27]. This effect is due to the presence of NiO_6 distortion (two Ni-O bond lengths: two bonds at 2.09 Å and four bonds at 1.91 Å) in $LiNiO_2$ [28].

The manganese-based oxides are comparatively less toxic, costs less, and have a high theoretical discharge capacity (258 mAh/g). However, the $LiMnO_2$ undergoes a capacity fading, phase instability and structural transformation during cycling [29]. The solid-state reactions for preparing the $LiMnO_2$ requires higher temperatures. Hence, it results in the formation of an O3 structure with a close-packed structure (ccp) from the stacked O atoms [29]. Moreover, it induces a formation of by-product, non-layered and stable spinel phase such as a spinel $LiMn_2O_4$.This is a result of a minor cationic rearrangement occurring during the first removal and intercalation of the Li atom. The process leads to the degradation of the electrode performance of the structure [29]. The structure as a result becomes unstable at high temperatures [29]. Hence, the $LiMnO_2$ structure turns to be complex, which makes it difficult for practical applications [27]. The layered Li_xMnO_2 with O2 structure and asymmetric hexagonal space group $P6_3/mmc$ to be thermodynamically metastable in comparison with the O3 –$LiMnO_2$ having the space group of $C2/m$, and more reliable to be used in doping.

1.3.1. Doping the Lithium Transition Metal Oxides

Considering the properties of the basic lithium transition metal oxide ($LiCoO_2$, $LiNiO_2$ and $LiMnO_2$) structures, much of the attention has been paid to the modification of the commercial cathode material $LiCoO_2$. The $LiCoO_2$ material is modified in the sense that the Co is partially substituted by the transition metals ions such as Ni or Mn, to improve the capacity and structural stability [27]. The main purpose of doping is to synthesise the material in a relatively short time and at low temperatures [29]. Previous studies reported that the result of the charge/discharge curve of the doped material has a similar shape to that of the spinel structure with two plateaus different from the ones of the existing layered $LiNiO_2$, $LiCoO_2$ and $LiMnO_2$ [29]. Through the applications of solid-state chemistry and electrochemistry methods, research was performed to investigate the effects of Ni and Li doping where they mixed $LiNiO_2$ with $LiCoO_2$ at a unit cell level to form a solid solution phase of $LiCo_{1-x}Ni_xO_2$ [29]. The method was experimentally shown to enhance the thermal stability and cycling performance since the Co replacement with Ni ions in $LiCo_{1-x}Ni_xO_2$ suppress the JT distortion of Ni^{3+} [29]. Conversely, the stability and the capacity of $LiNiO_2$ were also improved by replacing Ni with Mn and Co. This is effective, according to the theoretical studies which show that the JT distortion in $LiNiO_2$ is suppressed by Co atoms that replace Ni atoms in the lattice [27], leading to $LiNi_{0.5}Mn_{0.5}O_2$ to exhibit a reversible

capacity of 150mAh/g [30]. This comes from a reversible Ni^{2+}/Ni^{4+} redox reaction, with Mn^{4+} in a fixed oxidation state [30].

In previous experimental research, $LiNi_{0.6}Co_{0.2}O_2$ powder was prepared and heated at 750°C, 850°C and 950°C [31]. The sample according to the experiment showed a hexagonal layered structure above the 885 °C heating temperatures with an increase in the primary particles' sizes. In addition, it was reported that $LiNi_{0.6}Co_{0.2}O_2$ exhibits uniform particle size when calcined at 850 °C. Moreover, they added that increasing a heating temperature increases the particle size leading to higher crystallinity which as a result affect the uniformity of the material. However, the heating temperature of 850 °C enhances the electrode reaction reversibility. This is because the utilization of the $LiNi_{0.6}Co_{0.2}O_2$ material is increased by a uniform depth of charge (DOC) of each particle in the homogenous particle [31]. Each annealed cell of the material at 850 °C as a result delivers 148 mAh/g discharge capacity at 0.2C for the first cycle.

1.3.2. Structural Parameters

The electrochemical properties of electrode materials depend significantly on the changes in structural parameters during cycling. The research based on the SCAN Metta-GGA density functional on $LiNiO_2$, $LiCoO_2$, and $LiMnO_2$ predicted that *a* parameter changes slightly during delithiation, whereas the orthogonal vector, c, changes considerably [32]. This effect may be attributed to differences in the structure of LiMnO (orthorhombic), and LiNiO and LiCoO (rhombohedral). It was inferred in the study that *a* parameter represents the in-layer distance between two transition metals (TMs) in $LiNiO_2$ and $LiCoO_2$, and it decreases with delithiation since the ionic radius of the TMs decreases with an increasing oxidation state of the TMs [32]. Moreover, the study reported a systematic monotonous increase in the *c* lattice vector for $LiNiO_2$ and $LiCoO_2$. The parameter represents the interlayer distance between two TM layers in $LiNiO_2$ and $LiCoO_2$, and it initially increases with delithiation due to electrostatic repulsion between adjacent O-layers, while close to the fully delithiated limit there is a decrease in interlayer slab distance [33]. The changes in volume with delithiation is a combined effect of *a* and c parameters, however, the c parameter provides a dominating effect. As such, the stability of a structure, and the capacity of a lithium-ion battery cell depends significantly on the c parameter [33].

1.3.3. Band Gaps

A bandgap is a distance between the valence band and the conduction band of electrons. It is a representation of the minimum energy that is required to excite an electron up to a state in the conduction band where it can participate in conduction [34]. The lower energy level is the valence band, and thus if a gap exists between this level and the higher energy conduction band, energy must be input for electrons to become free. The size and existence of this band gap allow one to visualize the difference between conductors, semiconductors, and insulators [35]. Figure 1.4 shows a band diagram that presents the distance between the valence and conduction bands.

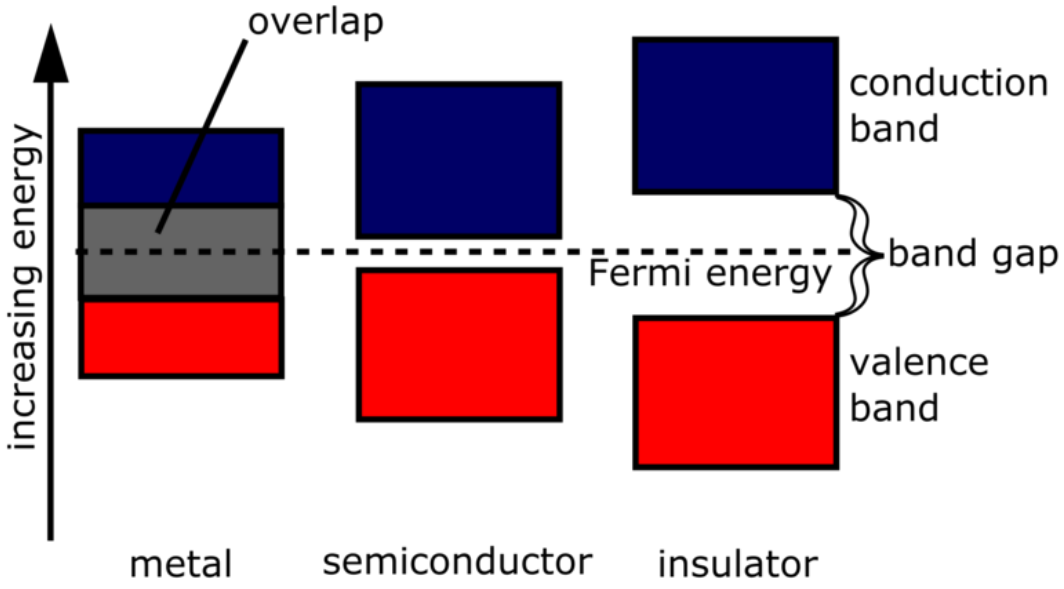

Figure 1.4 A bandgap diagram showing the different sizes of band gaps for conductors, semiconductors, and insulators [36]

In conductors, the valence band overlaps with the conduction band. The overlapping causes the valence electrons to be essentially free to move into the conduction band and participate in conduction. Since it is not a full overlap, only a fraction of the valence electrons can move through the material, but this is still enough to make conductors conductivity [37].

In semiconductors, the gap is relatively small enough that it can be bridged by some excitation. The gap is essentially some size that of a conductor or insulator. In this, a

finite number of electrons can reach the conduction processes to occur as a result of the electron-hole left behind [34].

In insulators, the electrons in the valence band are separated by a large bandgap from the conduction band. That is there is a large forbidden gap in conduction. This as a result provides a clear reason for insulators not conducting electricity [38].

1.3.4. Magnetic and Electronic Properties

On the recent PBE work [30] the electronic and magnetic properties of $LiNiO_2$ were examined considering both parallel and antiparallel configuration for the Ni ion. The total energy calculations presented that the ferromagnetic (parallel), configuration is energetically favourable by 16 meV per formula unit [30]. This was the case due to that in fully lithiated $LiNiO_2$, all the Ni ions are in a 3+ oxidation state and the low-spin (LS) electronic configuration for Ni^{3+} $t_2{}^6{}_g(|\uparrow\downarrow|\uparrow\downarrow|\uparrow\downarrow|)e_g{}^1(|\uparrow|)$. As such, the calculated local magnetic moment of Ni in $LiNiO_2$ is expected to be ~1 μB [34, 37]. However, the presence of Ni^{4+}, which has $t_2{}^6{}_g$ $(|\uparrow\downarrow|\uparrow\downarrow|\uparrow\downarrow|)$ $eg^0(|\ \ |\ \ |)$ configuration makes the local magnetic moments of Ni sites in partially and fully delithiated states different [37, 34]. Conversely, the observation of hybridization between Ni-d and O-p states have been made, together with a finite density of states (DOS) at the Fermi level. That is from the DOS it was discovered that both up and down t_{2g} spin channels are completely occupied, while the up channel of e_g is partially occupied, indicating that Ni^{3+} is in Low Spin. On the other hand, the experimental valence electron XPS for $LiNiO_2$ showed that the band near the Fermi level (at ~ -1.4 eV) is composed of Ni-3d, while O-2p states were found at ~ -3.8 eV [30].

Similar work disposed of that the local magnetic moment on Co sites in the fully lithiated. This is due to the Co^{3+} ions in a low-spin state (LS) with $t_2{}^6{}_g$ $(|\uparrow\downarrow|\uparrow\downarrow|\uparrow\downarrow|)$ $eg^0(|\ \ |\ \ |)$ [30]. Moreover, the electronic structure (DOS) brought to attention a strong hybridization between Co-3d and O^{-2}. Hence the t_{2g} band of Co is completely occupied in both spin channels, while e_g is unoccupied, reflecting more evidence of the LS state of Co. Esling et al. [38] performed valence XPS of $LiCoO_2$ and noted a dominant contribution of Co-3d states in the upper valence band region (~ -1-3 eV). As a result, they suggested broadband near 2.5-7.5 eV has prevalent O-2p character, but with some Co 3d admixtures.

For the $LiMnO_2$, the antiferromagnetic (AFM) spin configuration is energetically favourable [30]. That is, the difference of total energy between antiferromagnetic and ferromagnetic configurations per formula unit is 0.125 meV, and a local magnetic moment of Mn (~ 3.6 μB). This suggests that Mn is in a high spin state with $t_2{}^3{}_g$ (| ↑ | ↑ | ↑ |) eg^0(| ↑|) configuration. On the other hand, strong hybridization between Mn-d and O-p near the Fermi level has been observed computationally and from experimental XPS [30, 39]

1.3.5. Challenges Encountered in Other Studies

Commercial cathode materials in lithium-ion batteries are synthesized by conventional solid-state methods. However, it is difficult to control the morphology and element distribution of cathode materials synthesized by these methods [39]. On the other hand, it is difficult to attain nano-sized materials by traditional precipitation, due to quite a long precipitation time that is usually needed to synthesize materials [39]. It has been reported that the mixed oxide $LiMO_2$ (M: Mn, Ni, and Co) inherits characteristics of mono metal oxide $LiCoO_2$, $LiNiO_2$ and $LiMnO_2$. However, the $LiMO_2$ (M: Mn, Ni, and Co) mixed oxides introduce challenges such as low initial coulombic efficiency, poor rate capacity and poor cyclability [40]. The electrochemical behaviour of the material is extremely dependent on the synthesis method because the crystallinity, phase purity, grain size, and cation mixing in the structure all rely on the synthesis method and influences the electrochemical performance of this material. Conversely, it is hard to prepare the $LiMO_2$ (M: Mn, Ni, and Co) mixed compound by solid-state methods, as it often results in a nonstoichiometric or impure product [40].

High-temperature treatment of $LiNiO_2$ leads to the decomposition from $LiNiO_2$ to $Li_{1-x}Ni_{1+x}O_2$ which has a partially disordered cation and it distributes at the lithium sites. The stoichiometry of $LiNiO_2$ affects the electrochemical properties of the material. Hence, little information about factors influencing the $LiNiO_2$ structure is yet been published [41].

It was reported that the existence of Ni^{2+} in the 3a site belonging to the lithium ions in the stoichiometric $LiNi_{1x}Co_xO_2$ imposed difficulty in the preparation of the compound and the cycling stability of the material, thus in more cycles, it became an obstacle due to the appearance of Li-branch on the surface of Li anode after many cycles [39]. Furthermore, $LiNiO_2$ as cathode material has been reported to be difficult to synthesize and suffers from poor cyclability. This is mainly due to the poor structural

stability of the $LiNiO_2$ compound caused by the Jahn-Teller (JT) effect of active Ni^{3+} ions in the lattice [42, 43]. The activity of Mn^{3+} ions, however, poses challenges towards the full exploitation of these materials. This Jahn-Teller activity is responsible for distortions of the MnO_2 octahedral in the orthorhombic and metastable layered dioxides of composition $LiMnO_2$, resulting in crystallographic phase transformation of $LiMnO_2$ to spinel structure during charge/discharge cycling, which imposes low reversible capacity and poor cyclability. The magnitude of the cooperative Jahn-Teller distortion varies widely and discontinuously at structural phase transitions, during the redox cycles that accompany Li insertion/extraction. These variations often cause a breakup of the material, which is detrimental to the capacity retention of a battery [42, 43].

1.4. The rationale of the Study

The NMC cathode materials are potential high energy density electrode materials that could penetrate the market and elevate functionality of lithium ion batteries at multiple scales of energy storage. However, there have been several challenges with their individual structural performances and attainment of the perfectly functional combination of a layered cathode material composed of all three transition metals i.e. manganese, cobalt and nickel. One of the key interests in the current study is to deduce the conductivity of $LiMnO_2$, $LiNiO_2$ and $LiCoO_2$ materials, and to determine the stable material which may not undergo the structural change during cycling. Furthermore, the study is directed towards derivation of interatomic potentials to enable large scale atomistic simulations of the individual $LiMO_2$ (M: Mn, Co, Ni) and later the microstructural evolution of doped $LiMnO_2$ with co and Ni to enhance the performance and structural stability.

Computational modelling including atomistic simulations and ab-initio techniques have shed critical insight on in-depth understanding of various material properties. As such, this work makes use of both computational approaches to investigate the electronic and atomistic level properties of these materials i.e. structural and electronic properties, and stability of NMC cathode materials.

1.4.1. Research Questions

The layered transition-metal oxides $LiMO_2$ [M: Ni, Mn and Co] exhibit rich defect physics emanating from the ability of the transition-metal ions to exist in different

charge and spin states; the strong coupling between charge, spin and local atomic structures [43]. These cathode materials exhibit two problems: the capacity fades on repeated cycling or holding in the charged state, particularly at elevated temperature, and they generate flammable gases during charging that create safety concerns [42]. The research is driven by the following questions:

1. How does these materials behave in their parent bulk form?
    a. Electrically.
    b. Mechanically.
2. Which elements of the structures affects mainly the performance of the structures at their bulk form?
3. What are the new and possible ways to come up with in attempt to improve the materials?

Limited studies have been carried out using atomistic simulations on the systems of interest hence the need to begin with understanding of individual systems in this study ($LiMnO_2$, $LiNiO_2$ and $LiCoO_2$). Therefore, there is a high necessity for deriving such interatomic potentials to enable a future work of doping the $LiMO_2$ (M: Mn, Ni, and Co) systems, validating the interactions, and utilising them to predict bulk and nanostructural properties of these materials.

1.4.2. Aims

The aim of the study is to investigate the structural and electrochemical performance of layered $LiMnO_2$, $LiNiO_2$ and $LiCoO_2$ nanoarchitecture materials.

1.4.3. Objectives

The objectives of this study will be to:

- generate nanoarchitectures of pure $LiMO_2$ (M: Ni, Mn, Co) structures.
- investigate their structural and electrochemical properties.
- develop interatomic potentials for Li, Mn, Ni and Co interactions.
- perform high temperature molecular dynamics simulations driven by the developed interatomic potentials.

1.4.4. Overview of the study

The primary aim of the study is to probe the electronic properties of the $LiMO_2$ (M: Mn, Ni, and Co). This is preceded by the determination of the Hubbard U parameters which produce comparable electronic structures to the experimental data. The band gaps are calculated from electronic band structures and their atomic contribution to the band gaps at the Fermi level are investigated for the systems. The electronic properties are important for enabling better understanding about the electronic contribution and electron valence states of the materials. Moreover, the ionic state and electrical conductivity of materials are essential for Li+ diffusion and electron transportation, respectively during the charge/discharge of the battery [44]. The conduction and electron contributions will be determined from the electronic band structures and density of states, respectively. The electronic band structures make it possible to determine the synthesizing routes $LiMO_2$ (M: Mn, Ni, and Co). Furthermore, the bonding properties of the materials in the band structures are split by the ligand field (Fermi level, E_f at 0 eV) into upper antibonding e_g bands and nonbonding t_{2g} bands with distinct energy gap Δ_0 which gives detail information about the conductivity of a material [45, 46, 47]. On the other hand, the density of states (DOS) describes the number of states per interval of energy at each available energy level. The DOS indicates how densely packed quantum states are in a system. They give detailed electron contributions particularly at the energy gap of a material to facilitate the conductivity of a material.

The study also investigates the mechanical properties of $LiMO_2$ (M: Mn, Ni, and Co). The mechanical properties of transition metal materials control the thermodynamic properties to determine their electrochemical performance. The crucial aspect of the mechanical properties in the study is the elastic constants. The elastic constants describe materials' response to the externally applied strain required to maintain a given deformation and provide useful information on the strength of the material. Another aspect of the mechanical properties is the stability criterion of a material. The stability criteria are a set of conditions on the elastic constants that are related to the second-order change in the internal energy of a crystal under formation. They help to prove information about the stability of a material. The stability of a material is determined from an indication of an excited state in the quantum mechanical quantization of the modes of vibrations of elastic structures of interacting particles by

phonon dispersion curves. The behaviour of phonon dispersion branches reflects specific features of the crystal structure and the interatomic interactions and, therefore, gives the most comprehensive and detailed information about the dynamical properties of crystals [48, 49]. Lastly, with respect to electronic scale simulations, the stability of the $LiMnO_2$, $LiNiO_2$, and $LiCoO_2$ systems are investigated from the total density of states, phonon dispersion curves and elastic constants.

The second aspect of interest is the derivation of interatomic potentials or force field for NiO and CoO. The derivation of model parameters is critical to molecular dynamics simulations. The approach is to adjust the parameters until they fit or are comparable to some parameters of experimental data. Simulations in the current study are based on atomistic technique which will employ empirically derived equations to describe the interatomic interactions. Atomistic simulation technique makes it is possible to simulate large systems with thousands of atoms and this renders it a desirable method for producing accurate statistical data from molecular dynamics simulations, to allow efficient use of large simulation cells and long simulation time. Moreover, the accuracy and reliability of the generated force fields rely on the quality of the interatomic potentials

Procedurally, the DFT+U method will be deployed to investigate the thermodynamic, electronic and mechanical properties of $LiMnO_2$, $LiNiO_2$ and $LiCoO_2$. Moreover, the interatomic potential interactions that can adequately model structural and thermodynamic properties of NiO and CoO systems are derived. The Co-Co, Co-O, Ni-Ni, and Ni-O interactions will be derived. Furthermore, the molecular dynamics (MD) simulations in conjunction with the derived interatomic potentials will be employed, to simulate the NiO and CoO systems at different temperatures. The transformation temperature is compared with the available experimental temperature in each structure to validate the newly derived interatomic potentials.

1.5. Outline of the Study

Chapter 1 is the general background of lithium-ion batteries and their applications. The structural aspects of the battery's cathode materials, thus the $LiMnO_2$, $LiNiO_2$, and $LiCoO_2$ structures are discussed in this chapter. Chapter 1 gives a detailed background of the study. The rationale and objectives of the study are outlined. Chapter 2 discusses the theoretical aspects and methodologies used in this study.

These include computational techniques such as energy minimisation, electronic structure methods, and molecular dynamics.

In chapters 3, 4, and 5 we outline the results of the work and our conclusion. That is, chapter 3 is the structural and electronic properties calculations performed on the $LiMnO_2$, $LiNiO_2$, and $LiCoO_2$ systems. Chapter 4 is the derivation of the interatomic potential model for NiO and CoO structures; and the validation of the potentials through molecular dynamics (MD). Lastly, in chapter 5 we give a summary of the main results presented in this work and recommendations for future research.

Chapter 2: Research Methodology

This section provides a theoretical background of the methods used in this study. Computational simulations have become a reliable approach in science research and engineering-related problems. As such, the impact of computer simulations has shown potential growth in modern technical days. We discuss in detail the molecular dynamics simulations and quantum mechanical density functional theory (DFT).

2.1 Computer Modelling

Computational modelling is the use of computers to simulate and study the behaviour of complex systems using mathematics, physics and computer science embodied in computer applications. Modelling is the representation of model construction and working of some system of interest [50]. It contains numerous variables that characterize the system being studied, yet it is but simpler than the system it represents. It offers a close approximation to the real system and incorporates most of its salient features. An important attribute in modelling is the simulation of a model under known input conditions and the comparison of the model output with the system output (model validity). The simulation is performed by adjusting each of the variables alone or in combination and observing how the changes affect the outcomes of the model [50].

Predominantly, a model intended for a simulation study is a mathematical model developed with the help of simulation software. A mathematical model classification includes deterministic (input and output variables are fixed values) or stochastic (at least one of the input or output variables is probabilistic); static (time is not taken into account) or dynamic (time-varying interactions among variables are taken into account). A simulation experiment is a test or a series of tests in which meaningful changes are made to the input variables of a simulation model [50]. They are used before an existing system is altered or a new system is built, to reduce the chances of failure to meet specifications, to eliminate unforeseen bottlenecks, to prevent under or over-utilization of resources and to optimize system performance. A good model is a judicious trade-off between realism and simplicity making it possible to understand and to perform experiments with. Hence, properties concerning the behaviour of the actual system or its subsystem can be inferred [50].

Computer simulations act as a bridge between microscopic length, time scales and the macroscopic world of the laboratory. Figure 2.1. shows the steps involved in developing a simulation model, designing a simulation experiment, and performing simulation analysis and figure 2.2 is a representation of simulations and real experiments.

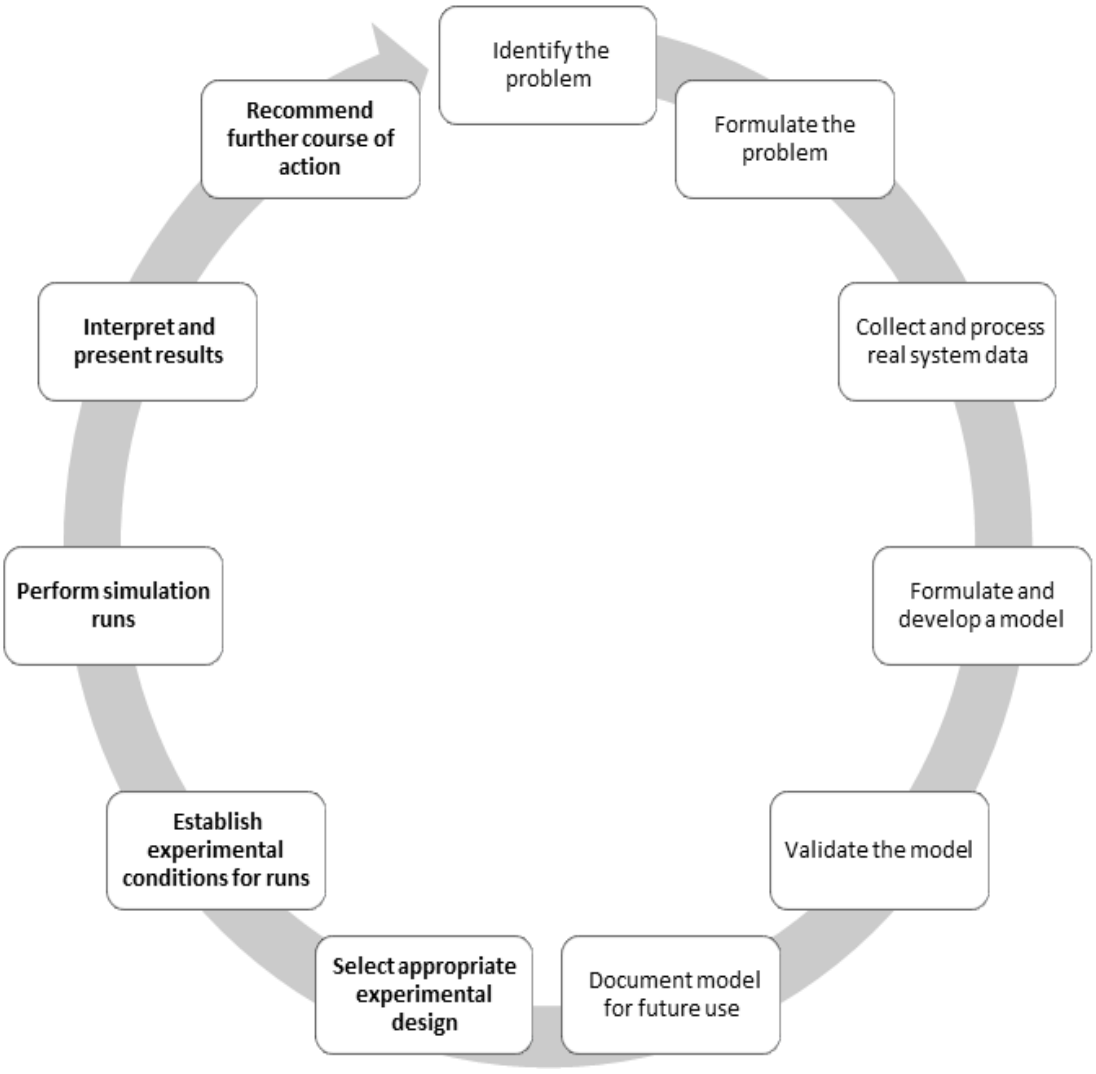

Figure 2.1. The steps in involved in developing a simulation model, designing a simulation experiment, and performing simulation analysis [50]

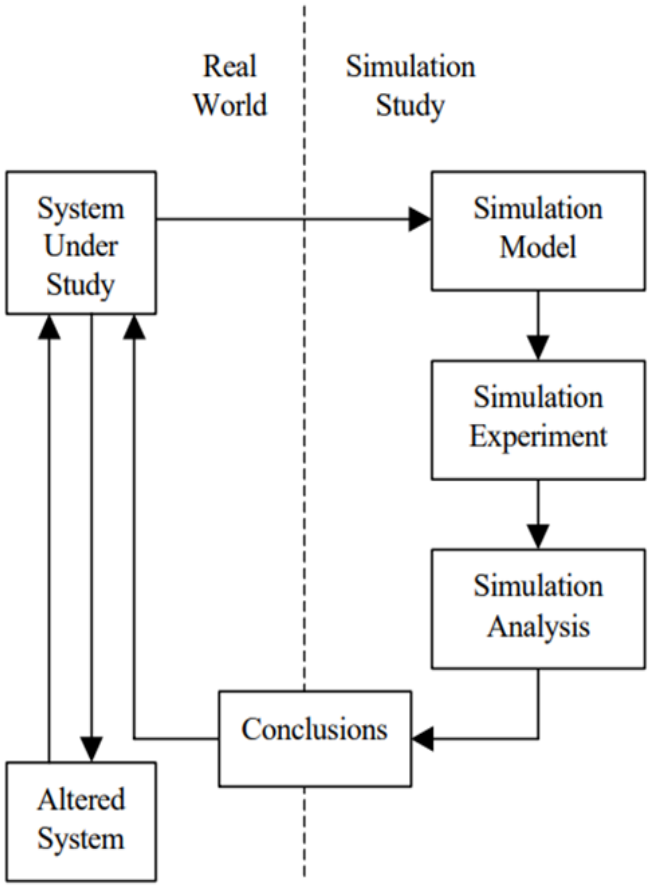

Figure 2.2 Schematic representation of simulation and experimental studies [50]

2.2 Energy Minimization

In molecular modelling, much of the interest is in the minimum points of the energy surfaces. The minimum energy configuration corresponds to the stable state of the system. Energy minimization (geometry minimization or energy optimization) is used to compute the equilibrium configuration of molecules and solids [51]. The stable states of molecular systems correspond to global and local minima on their potential energy surface. Hence, starting from a non-equilibrium molecular geometry, energy minimization employs the mathematical procedure of optimization to move atoms to reduce the net forces (the gradients of potential energy) on the atoms until they become negligible [51]. During the energy minimization process, the geometry is changed in a stepwise fashion so that the energy of the molecule is reduced. After several steps, a local or global minimum on the potential energy surface is reached. This final state of the system corresponds to a local minimum of potential energy,

where the temperature of the system is approximately zero. The procedure for energy minimization is shown in figure 2.3 below [51],

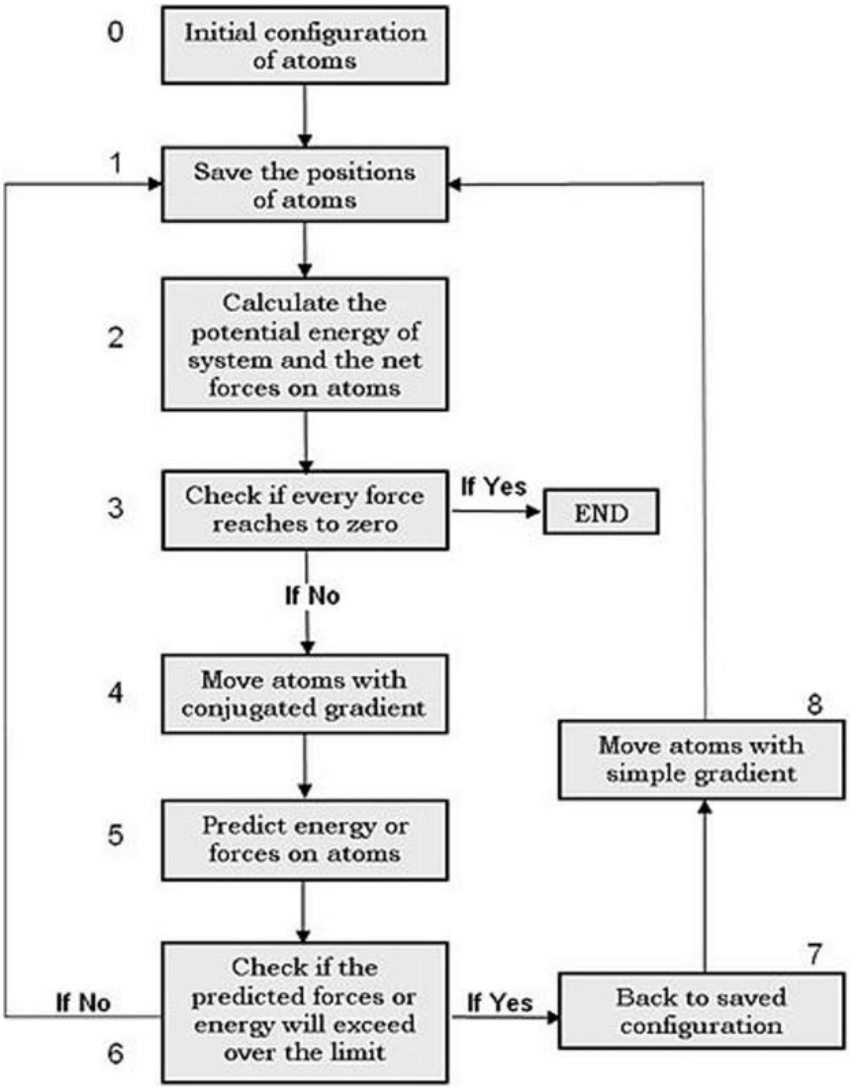

Figure 2.3. The schematic representation of computational energy minimisation procedure [51]

2.3 Ab Initio

Ab initio is a group of methods in which properties of materials, that is the values of the fundamental constants and the atomic number of the atoms present can be calculated using the Schrodinger equation. These equations include density functional theory (DFT), Hartree-Fock (HF) methods and post-Hartree-Fock (PHF) methods [52]. The first principle ab initio methods for self-consistent calculations of electrons density distribution around moving ions, use electrons, nuclei, and their interactions to perform calculations. They do not require empirical input and therefore they can accurately

describe the interatomic interactions in a different environment. As such, they provide accurate modelling techniques [52]. The methods consider local chemical and magnetic effects to provide significant potential for predicting material properties. Ab initio calculations are used with success in applications where the properties are limited to the nanoscale [52].

Several factors have contributed to the present success of *ab initio* calculations for exceptional materials systems. The first is the availability of modern high-speed computers. This has made it possible to carry out calculations on materials in complex situations with sufficient accuracy [53]. They provide a meaningful detailed comparison with experimental measurements. The second is the advert of density functional theory (DFT) and continuing development of approximations to the DFT formalism for electron exchange and correlation. The third is the refinement in the band structure calculation techniques and the invention of the *ab initio* pseudopotentials [53], which leads to rapid computation of total energies. The density functional methods have made it feasible to calculate the ground state energy and charge density with remarkably accurate results for real solids. Finally, there have been significant new developments in experimental technique and materials preparation that are making it possible to investigate the structure of matter. In advance is the ability to create high pressure and explore the properties of matter over a wide range of densities [54]. This is an ideal experimental tool to provide information that can be compared directly with current theoretical calculations.

2.4 Density Functional Theory

The density functional theory (DFT) is a quantum mechanical theory used mainly in physics, material sciences, and chemistry to probe electronic properties and ground-state properties of many-body systems, particularly molecules, condensed phases, and atoms. DFT is based on the concepts of Thomas [55] and Fermi [56]. It was developed by Hohenburg, Kohn and Sham [57] employing the two theorems. The theorems are stated as follows: the first theorem states that for any system of interacting particles in an external potential V (r), the external potential is uniquely determined (with a constant excluded) by the ground state density p_0(r) [57]. The theorem provides a foundation for reducing the many-body system using electron density functional. Hence the electron density depends on 3 spatial coordinates instead of 3N [57]. The second theorem describes that a universal function for the

density energy could be defined for all-electron systems. Although the exact ground state is the global minima for a given external potential. Conversely, the density which minimises the function is the exact ground state density [58].

Moreover, the DFT determines properties of many-electrons systems using a function of function (functional), which is dependent on the density of electrons. The DFT method was recognised to be accurate for quantum chemistry calculations in the early 90s, following the enhancement of the approximations involved in the method in modelling the exchange and correlation interactions [59]. Although the DFT approach still has challenges to describe properly the intermolecular interactions, such as Van der Waals forces, excitations during charge transfer, transition states, bandgap in semiconductors, global potential energy surface and strongly correlated systems [60, 61]. It has been proven by Kohn and Sham that the properties of the total ground-state of an interacting electron gas may be described by introducing a certain functional of the electron density ρ(r), which depends on the positions of atoms [58].

$$E(\rho) = \int \rho(r) v_{ext}(r) dr + \frac{1}{2} \iint \frac{\rho(r)\rho(r')}{|r-r'|} dr dr' + G[\rho], \quad (2.1)$$

where $v_{ext}(r)$ is the external field integrating with the field of the nuclei; the functional G(ρ) comprises the kinetic and exchange-correlation energy (E_{XC}) of the interacting electrons. G(p) is universal and is independent of the external fields. Moreover, the expression is a minimum for the correct density function $\rho(r)$. The equation made it possible for both Kohn and Sham to further develop the concept and make a suggestion of G(p) form as follows [62]

$$G(\rho) = T(\rho) + E_{XG}(\rho), \quad (2.2)$$

where T (ρ) is the kinetic energy of the non-interacting electrons with density $\rho(r)$ and the functional $E_{XG}(\rho)$ encompassing the many-electron effects of the exchange and the correlations. The exact many-body and correlation interaction are unknown, hence there is an approximation that the exchange-correlation is then taken from the known results of an interacting electron system of constant density (homogeneous electron gas), and it is assumed that the exchange and correlation effects are not strongly dependent on inhomogeneities of the electron density away from the reference point r. Therefore, it is necessary to determine the set of wave function ψ_i that minimises the Kohn-Sham energy functional. The electron density is denoted as follows:

$$\rho(r) = \sum_{i=1}^{N} |\psi_i(r)|^2 \ , \tag{2.3}$$

where N represents the number of electrons. The Kohn-Sham energy function is then given by a self-consistent solution.

$$\left[- \nabla^2 + \sum_I \frac{2Z_I}{|r-R_I|} + \int 2 \frac{\rho(r')}{|r-r'|} dr' + V_{xc}(r) \right] \psi_i = \varepsilon_i \psi_i \ , \tag{2.4}$$

where R_i is the position of the nucleus I of charge Z_i and ε_i is the Lagrange factor. The exchange-correlation potential, V_{xc} is given as a functional derivative:

$$V_{xc}(r) = \frac{\delta E_{xc}[\rho(r)]}{\delta \rho(r)} \ , \tag{2.5}$$

It is applicable for ground-state and the exchange-correlation energy, the DFT is only known by approximation. This theory can hardly be overemphasised. It reduces the many-electron problem to an essentially single-particle problem with the effective local potential,

$$V(r) = \sum_I \frac{2Z_I}{|r-R_I|} + \int 2 \frac{\rho(r')}{|r-r'|} dr' + V_{xc}(r), \tag{2.6}$$

However, a critical concern in DFT application is the way the functional E_{xc} is defined. The energy functional, $E_{xc}(\rho)$ for inhomogeneous electron gas is expressed as Coulomb interaction between the electron and its surrounding exchange-correlation hole [63];

$$V_{xc}[\rho] = \frac{1}{2} \int dr \rho(r) \int dr' \frac{(r,r'-r)}{|r-r'|}, \tag{2.7}$$

The critical drawback about the DFT is that the exact functionals for exchange and correlation are not known beside for the free electron gas, contrary, the approximation method can resolve the problem. The two commonly used approximations include generalised gradient approximation (GGA) and local density approximation (LDA). The methodology for solving the Schrodinger equation and the DFT Kohn-Sham equation respectively are depicted in figure 2.4 below.

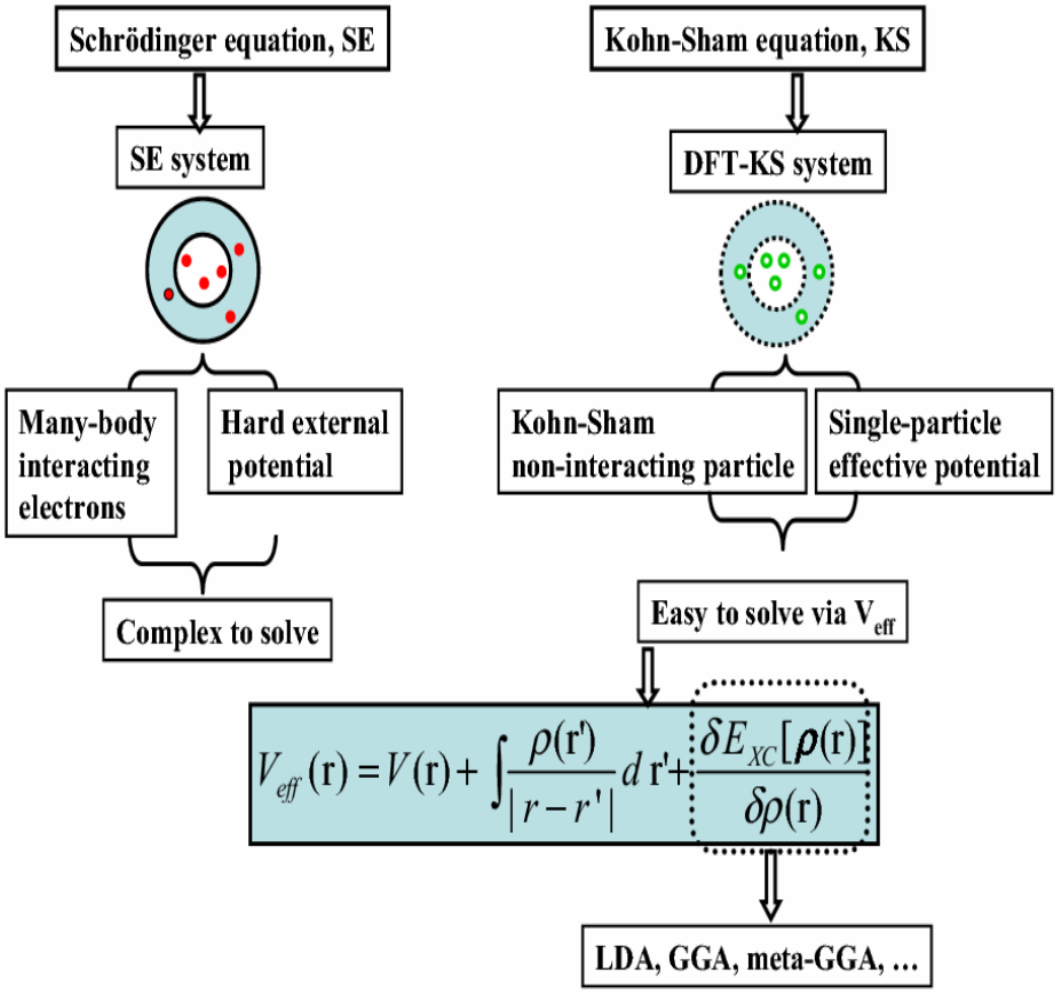

Figure 2.4 a comparison of the methodology for solving the many-body Schrodinger equation and effective one-electron Kohn-Sham equation [63]

2.5 Molecular Dynamics

Molecular dynamics simulation is a technique for computer simulation of complex systems, modelled at the atomic level. It is used to study the motions of atoms in a given system to understand and predict the structural, dynamic, kinetic and equilibrium properties under the chosen conditions (compositions, temperatures, and pressures) [64] in the same manner as experiments. It can provide details of atomistic processes in microstructural evolutions. However, it is limited to full functionality within a certain range of length and time scales. Consequently, it needs to be integrated with other computational methods to span the length and time scales of interest [65].

2.5.1 Aims of Molecular Dynamics

A molecular dynamics simulation aims to present a simple model for the appropriate many-body problem and to use that model to gain insight into the possible behaviour of the real system. It provides an understanding of the properties of assemblies of molecules in terms of their structure and the microscopic interactions between them. The model under study is best based on a minimum number of adjustable parameters, and these are not to be continually altered to improve the fit with the experiment. This serves as a complement to conventional experiments, enabling a researcher to learn something new, something that cannot be found out in other ways [66].

2.5.2 The Molecular Dynamic Approach is as Follows

First during sample preparations: a model system consisting of N particles is selected and Newton's equations of motion for this system are solved until the properties of the system no longer change with time (equilibration of the system). After equilibration, the actual measurement is then performed. It uses assumptions like the Born-Oenheimer approximation [67], where the nuclei are assumed to be stationary. The atomic positions and velocities are accrued from the variation and integration of the following equations with time steps chosen accordingly.

$$V\ (t\ +\ \delta t) =\ v(t) + \frac{1}{2}[a(t) +\ a(t\ +\ t)]\delta t \tag{2.8}$$

$$r(t\ +\ \delta t) =\ r(t) +\ v(t)\delta t\ + \frac{1}{2}a(t)\delta t2 \tag{2.9}$$

The atomic acceleration is obtained from Newton's 2nd law of motion, which states as:

$$a_i = \frac{F_i}{m_i} \tag{2.10}$$

To measure an observable quantity in a molecular dynamics (MD) simulation, the observable first must be expressed as a function of the positions and momenta of all particles in the system. The average volume of the system is determined by the balancing between the internal pressure and the externally set pressure. The enthalpy of the system is approximately conserved, so this method generates constant enthalpy, constant pressure (NPH) ensemble [64].

Molecular dynamics simulation is advantageous in the sense that it gives a route to dynamical properties of the system: transport coefficients, time-dependent responses to perturbations, rheological properties, and spectra. It is described by a force field

(inter-atomic potential) allowing researchers to examine the effect of temperature on a system [64].

2.5.3 Force Field

Force field (interatomic potentials) refers to the functional form and parameter sets used to calculate the potential energy of a system of atoms in molecular dynamics simulations. It describes physical systems as collections of atoms kept together by interatomic forces, with the interaction law specified by the potential U (r_1,…, r_N), which represents the potential energy of N interacting atoms as a function of their positions $r_i = (x_i, y_i, z_i)$. The force acting upon ith atom is determined by the gradient (vector of first derivatives) for atomic displacements.

$$F_i = -\nabla U(r_1, \dots, r_N) = -(\frac{\partial U}{\partial x_i}, \frac{\partial U}{\partial y_i}, \frac{\partial U}{\partial z_i}) \quad (2.11)$$

A force field or interatomic potential is made up of a set of equations that defines the variation of the potential energy of a molecule or a crystal with the locations of its component atoms, where the type of the atom depends on hybridization, charge, and the types of the atoms to which a reference atom is bonded to. The force constants and structural parameters such as bond lengths and angles are defined by the parameter sets.

Molecular dynamics simulations models polarizability can introduce induced dipoles through different methods, such as fluctuating charges. This allows for dynamic redistribution of charge between atoms which respond to the local chemical environment.

2.5.4 Limitations

There are numerous drawbacks associated with molecular dynamics. That is, a force field can achieve excellent results only for a limited class of molecules or solids, related to those for which it was parameterised. The results are relatively not as good as the force field used. Molecular dynamics methods cannot treat chemical problems in which electronic effects predominate due to the neglected electrons. However, several methods are available for controlling temperature and pressure where specific ensembles are selected to calculate the structural, energetic, and dynamic properties of a system.

2.5.5 Molecular Dynamics Ensembles

A system is described using an ensemble, particularly described as a statistical ensemble which is an idealization consisting of many copies of a system [68]. Considering all at once, each of which represents a possible state that the real system might be in. The ensembles provide a way to derive the properties of real thermodynamic systems from the laws of classical and quantum mechanics [68]. The molecular dynamics calculations consider different systems with different degrees of separation from their surroundings. MD considers three main ensembles namely, microcanonical, canonical and isothermal-isobaric ensembles [68].

(i) Micro Canonical (NVE) Ensemble

The microcanonical ensemble, represent the possible states of a mechanical system that has an exactly specified total energy. The system is isolated from changes in moles (N), volume (V), and energy (E). The system cannot exchange energy or particles with its environment. Furthermore, if no time-dependent external forces are considered, the system's Hamiltonian is constant.

(ii) Canonical (NVT) Ensemble

The canonical ensemble is an ensemble where the number of particles (N), the volume (V) and the temperature (T) are fixed to prescribed values. The temperature T is, in contrast to N and V, an intensive parameter and the energy of endothermic and exothermic processes is exchanged with a thermostat.

(iii) Isothermal–isobaric ensemble (NPT)

The isothermal–isobaric ensemble, is a statistical mechanical ensemble where the amount of substance (N), pressure (P) and temperature (T) are conserved. It corresponds most closely to laboratory conditions with a flask open to ambient temperature and pressure.

2.5.6 Molecular Dynamics Properties

Computer simulations can calculate different types of thermodynamic properties, this is done by employing the molecular dynamics technique. The simulations produce comparative results with experiments making it possible to quantify the potential models used and to validate the obtained results.

(i) The Temperature

A temperature in a many-body system makes use of the equipartition of energy overall degrees of freedom that enter quadratically in the Hamiltonian of the system.

The temperature in a simulation is calculated from the standard expression of statistical mechanics, relating it to the kinetic energy of the atoms and given by:

$$T_{inst} = \frac{2}{gk_B} E_{kin} \tag{2.12}$$

where E_{kin} is the kinetic energy at present, g is the number of degrees of freedom of the system and k_B is Boltzmann's constant. The expression gives the instantaneous temperature of the simulation with the value being different at different time steps represented by:

$$< T >= \frac{1}{N} \sum_n T_{inst}(n) \tag{2.13}$$

where the summation is over all time steps (or a subset) of the simulation, N. If an appropriate equilibration period has been undertaken before the actual simulation, the temperature of the simulation will be close to the desired target temperature, i.e., < T > ≈ T_{target} [69]. The temperature, the same as the pressure, depends on the type of ensemble used for a simulation. In a canonical ensemble, the total temperature is constant whereas it can fluctuate in the microcanonical ensemble. The temperature is usually related to the kinetic energy of the system as follows:

$$K = \sum_{i=1}^{N} \frac{|P_i|}{2m_i} = \frac{K_B T}{2} (3N - N_C) \tag{2.14}$$

where P_i is the total momentum of a particle i and m_i is its mass and N_C is the number of constraints on the system. Each degree of freedom contributes $\frac{K_B T}{2}$ according to the theorem of equipartition of energy. If there are N particles, each with three degrees of freedom, then the kinetic energy is assumed to be equal to $\frac{3NK_B T}{2}$ [69].

It is a crucially important parameter in almost all systems and its speciation is not necessarily straightforward, particularly for atomistic systems. The temperature-based results that are within a tolerable precision limit depends on the temperature dependence of another parameter.

(a) Melting Temperature (Tm)

Melting temperature is a temperature at which under specific pressure, the liquid and solid phases of a substance coexist in equilibrium. In general, the melting temperature

of most substances is the same as their freezing temperature, due to the evidence that the substance melts at a similar temperature as that at which it freezes.

In computer simulations, the pressure and temperature can be kept constant while allowing the energy to fluctuate until a stable value is reached. The melting temperature for spherical particles of radius R is determined from Gibbs free energies of solids and liquids, with assumptions of constant pressure conditions given by:

$$\frac{T_m^b - T_m(R)}{T^b{}_m} = \frac{2}{\rho_s L^b{}_R}\left[\gamma_{sv} - \left(\frac{\rho_s}{\rho_l}\right)^{\frac{2}{3}}\gamma_{lv}\right] \quad (2.15)$$

where ρ_s and ρ_l are the solid and liquid densities, L_b is the bulk latent heat of melting, γ_{sv} and γ_{lv} are the solid-vapour and liquid-vapour interface energies, respectively.

(ii) Radial Distribution Function (RDFs)

The radial distribution function (RDF) defines the probability of finding a particle at a distance r from another tagged particle compared to a homogenous distribution [70]. It is denoted by:

$$g(r)_I = 4\pi r^2 \rho\, dr\,, \quad (2.16)$$

where $\rho\ is$ the number density, r is the radial distance between atoms and g(r) is the probability of finding an atom a distance r from another atom (or molecule) compared to the ideal gas distribution.

The radial distribution function (RDF) is constructed as a histogram of the distances between an atom and its neighbours during the simulation. It is a useful way of describing the structure of a system and the type of matter. It consists of multiple numbers of sharp peaks whose separation and heights are characteristic of the lattice structure, used to differentiate between solids, liquid, and gas phases. They are also used to calculate noticed change in structural phases. Lastly, they give the probability of finding the centre of a particle or atom at a given distance from the centre of another particle. In figure 2.5. (b) below the central atom is a reference atom. It is drawn with radius r. Figure 2.5. (a) below simplifies the demonstration of atom interactions in different orbitals in a different matter.

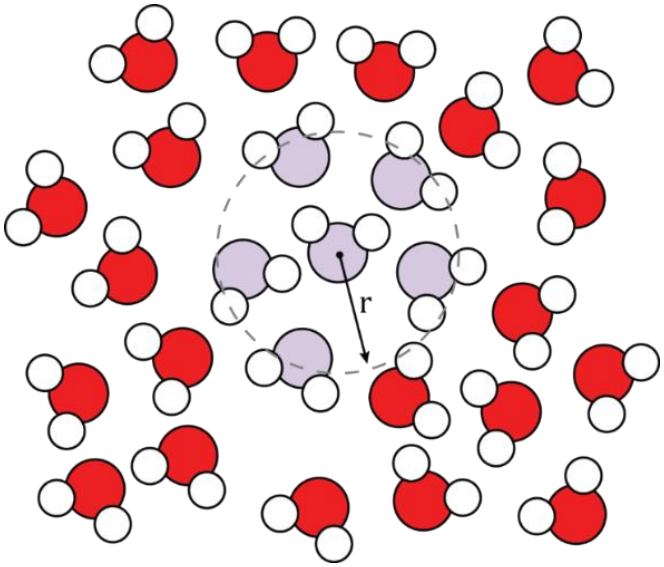

Figure 2.5. The schematic representation of radial distribution function (RDF)

Each peak represents a coordination shell for the solid, with the nearest neighbours being found in the first coordination shell, the second nearest neighbours being found in the second and so on.

(iii) Diffusion Coefficients

A diffusion coefficient is a proportionality constant between the molar flux due to molecular diffusion and the gradient in the concentration of the species (driving force for diffusion). Diffusivity coefficient in solids at different temperatures is predicted by Fick's law given as:

$$D = D_0 e^{\frac{-E_A}{RT}}, \tag{2.17}$$

where D is the diffusion coefficient, D_0 is the maximum diffusion coefficient (at infinite temperature), T is the temperature in units of [absolute temperature (kelvins or degrees Rankine)], R is the gas constant in dimensions of [energy temperature^{-1} (amount of substance)$^{-1}$] and E_A is the activation energy for diffusion in dimensions of [energy (amount of substance)$^{-1}$].

The diffusion coefficient can be estimated from the integral of the velocity autocorrelation function as:

$$D = \frac{1}{3}\int_0^{\infty} < v_i\,(t) \cdot v_i\,(0) > dt, \tag{2.18}$$

Alternatively, from the slope of mean-square displacements plots using Einstein relation as by:

$$D = \frac{1}{6}\frac{d}{dt} < \left| r_i\,(t) - r_i\,(0) \right| >, \qquad (2.19)$$

It is a physical constant dependent on molecule size and other properties of the diffusing substance as well as on temperature and pressure. It implies that the mass of the substance diffuses through a unit surface in a unit time at a concentration gradient of unity [71]

2.6 The Potential Model

The potential model considers one or more interaction terms for a physical system, it is used to investigate particle and high energy systems by describing the variation in the energy of the molecule or solid as a function of atomic coordinates [72]. It depends solely on the quality and accuracy of the potential model; considering various experimental and theoretical aspects of the potential model as related to particle and high energy physics. Various Coulombic summation schemes that have been employed are described below [72].

2.6.1 Born Model of Solids

The Born Model of Solids with the assumption that the energy and its derivatives are defined as the simulation of all interactions between the atoms in the system, giving rise to the total interaction and total net force acting on each atom due to others [73]. In this model, the atoms of a system are represented as point charge particles that interact through long-range electrostatic forces and short-range interactions. As such the interaction energy between the atoms is represented by:

$$U_{ij} = \frac{1}{4\pi\epsilon_0}\frac{q_i\,q_j}{r_{ij}} + \Phi(r_{ij}), \qquad (2.20)$$

where term one represents long-range coulombic interactions, q_i and q_j are the ionic charges, ϵ_0 is the permittivity of vacuum, and r_{ij} is the interatomic distance. The second term, $\Phi(r_{ij})$ describes short-range interactions between ions, which includes the repulsion between the electron charge clouds and the Van Der Waals attraction forces [73].

(i) Long-Range Interactions

A long-range include charge-charge interactions between ions and dipole-dipole interactions between molecules. Hence, the ionic system with a pair of ions i and j, separated by a distance r_{ij}, possess the coulombic interaction energy between them.

The long-range interaction energy of two ions (ion i and ion j) with charges q_i and q_j is given by:

$$\Phi_{lr}\left(r_{ij}\right) = \sum \frac{1}{4\pi\varepsilon_0} \frac{q_i q_j}{l+r_{ij}}, \tag{2.21}$$

where r_{ij} is the displacement separating the two ions, ε_0 is the permittivity of free space and l is the set of lattice vectors representing the periodicity of the crystal lattice. Contrary to ionic systems, this interaction will not be present in a non-ionic system and only short-range interactions will be considered. This is because long-range interactions describe the coulombic summation only [73].

(a) Ewald Summation

Ewald summation is a method for computing long-range interactions (electrostatic interactions) in periodic systems. It calculates the electrostatic energies of ionic crystals together with the electrostatic potential acting on an object ion in a lattice. The lattice is made up of ions acting as an array of positive and negative charge points. The total potential, φ, acting on the object/ion by the array of point charges are separated into two components. One part in real space, φ_1, and the consecutive part in reciprocal space, φ_2, given by:

$$\varphi = \varphi_1 + \varphi_2 \tag{2.22}$$

The real part, φ_1, consists of an array of point charges countered by an array of Gaussian charge distributions equal in magnitude but opposite in charges. Thus, each ion is effectively neutralised and neighbouring ions no longer interact. The reciprocal part, φ_2, consists of an array of Gaussian charge distributions, φL, with equivalent charge and magnitude as the original point charge array. Ewald summation is a special case of the Poisson summation formula, it replaces the summation of interaction energies in real space with an equivalent summation in Fourier space. The advantage of this method is the rapid convergence of the energy compared with that of a direct summation. This means that the method has high accuracy and reasonable speed when computing long-range interactions. The method requires charge neutrality of the molecular system to calculate accurately the total Coulombic interaction [73].

(ii) Short Range Interactions

The short-range interactions are given in one or more ranges for each ion pair, up to a maximum range. At small distances, the electron cloud overlap leads to strong short-

range repulsive forces due to electron density and as a result, the nuclear shielding is reduced. This increases the Columbia repulsion between the positively charged nuclei. This force prevents a crystal lattice from collapsing on itself. However, before the nuclear repulsion becomes significant there is also a quantum mechanical effect because the electrons are forced to occupy a smaller portion of space. Since the electrons must maintain orthogonal orbitals, the energy states increase in energy. This is known as orthogonalisation or Pauli repulsion. There is a contrasting longer-range attractive interaction at larger interatomic distances arising from the formation of instantaneous dipoles between adjacent electron clouds. This effect (Van Der Waals interaction) is also quantum mechanical in origin. By only adjusting the much smaller short-range contribution the whole spectrum of crystal structures can be reproduced. Below some of the possible descriptions for the short-range interaction are discussed. The most basic form would be a simple harmonic interaction, given by:

$$\Phi_{sr}\left(r_{ij}\right) = \frac{1}{2}K(r_{ij} - r_0)^2 \ , \tag{2.22}$$

where r_{ij} is the distance between two atoms i and j, r_0 is the equilibrium bond distance and K is the harmonic force constant. This model is quite sufficient for systems that only deviate slightly from r_0 and for which interactions can realistically be confined to adjacent pairs of ions [73].

(a) Buckingham potential

The Buckingham potential describes the exchange repulsion, which originates from the Pauli exclusion principle, by a more realistic exponential function of distance. It is a formula that describes the van der Waals energy $\Phi(r_{ij})$ for the interaction of two atoms that are indirectly bonded as a function of the interatomic distance (r). It is used to model two body non-bonded interactions in ionic solids. The general form of Buckingham potential is:

$$\Phi(r_{ij}) = A_{ij*}\, exp^{-\frac{r_{ij}}{\rho_{ij}}} - \frac{C_{ij}}{r^{6}_{ij}} \tag{2.23}$$

where A_{ij} is the size of the ions, ρ_{ij} is the hardness and C_{ij} is the dispersion parameter. The first term is called the Born-Mayer potential and the attraction term was added to it to form the Buckingham potential. For the cation-anion interactions, the attractive term is often ignored due to its small contribution to the short-range potential.

(b). Three-body potentials

The three-body potentials are mostly valence angle forms. They are primarily included to permit the simulation of amorphous materials. The potential forms available are as follows.

$$U(\theta_{jik}) = \frac{k}{2}(\theta_{jik} - \theta_0)^2 \quad (2.24)$$

where k_{ijk} is the three-body force constant and θ_0 is the equilibrium angle.

2.7. Simulation codes

2.7.1. GULP

GULP is a cross-platform, streaming task runner (code-based) program for performing a variety of types of simulations on materials using boundary conditions of 0-D (molecules and clusters), 1-D (polymers), 2-D (surface, slabs and grain boundaries), or 3-D (periodic solids). The code focuses on analytical solutions, through the use of lattice dynamics. A variety of forces fields are used within the GULP spanning the shell model for ionic materials, molecular mechanics for organic systems. It includes analytical derivatives up to at least second order for most force fields and third-order for many [74].

2.7.2. DL_POLY

DL_POLY is a general-purpose molecular dynamics (MD) simulation package developed at Daresbury Laboratory [75]. Its general design provides scalable performance from a single processor workstation to a high-performance parallel computer, provided MPI2 instrumentation is available on the parallel machine. It is supplied in source form under license and can be compiled as a serial application code [75].

(i) INPUT FILES

DL POLY_2.0 requires six input files named: CONTROL, CONFIG, FIELD, TABLE, TABEAM, and REVOLD. The first three files are mandatory, while files TABLE and TABEAM are used only to input certain kinds of pair potential, as a result, they are not always required. RE D is required only if the job represents a continuation of a previous job.

(ii) OUTPUT FILES

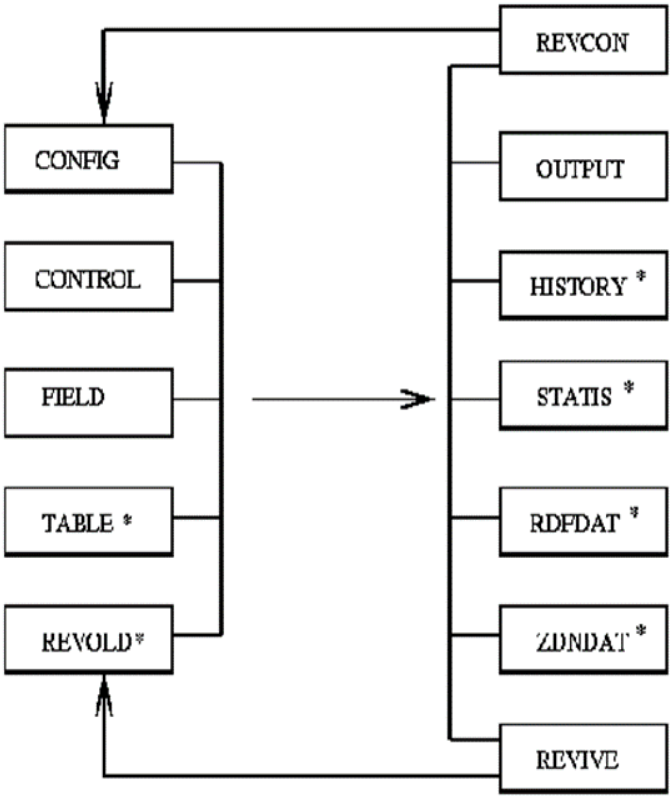

Figure 2.6. Schematic representation of DL_POLY input and output files.

After the execution, the DL POLY code produces up to eight output files: HISTORY, OUTPUT, REVCON, REVIVE, RDFDAT, ZDNDAT, STATIS and CFGMIN. These respectively contain a dump file of atomic coordinates, velocities and forces; a summary of the simulation; the restart configuration; statistics accumulators; radial distribution data, Z-density data, a statistical history, and the configuration with the lowest configurational energy. Some of these files are optional and appear only when certain options are used. The schematic representation of the DL_POLY input and output files is shown in figure 2.6 above.

2.8 Approximation Methods

Physical systems are described by complicated equations with detailed exact solutions; the details of the solution may obscure easy interpretation of results, rendering the solution to be of small aid in discerning trends or identifying the most important causal agents [76]. As such a carefully crafted approximate solution will yield a result that exposes the important driving physics and filters away extraneous features of the solution. This gives rise to the use of approximation methods to

generated approximate solutions. The approximation methods rely on some form of linearization to capture the behaviour of some local nonlinearity [76].

2.8.1 Local Density Approximation

The local density approximations (LDAs) are a set of approximations to the E_{xc} functional in DFT which is determined by the electronic density at a point in space. They demonstrate that E_{xc} is similar to that of a locally uniform electron gas with similar density in regions where there is slow variation in charge density [77]. The approximation is mainly used where the E_{xc} density is local of an inhomogeneous system substituted be that of an electron gas evaluated at local density. The LDA is based on two basic assumptions, (1) the exchange and correlation effects are from the immediate locality of point r. (2) the correlation effects are slightly dependent on the alteration of the electron density in the locality *r* [78]. The fulfilment of these two conditions results in the same contribution from the volume element dr as the volume element was surrounded by a constant electron density ρ(r) of the same value as within d(r). The exchange-correlation energy density of the homogenous electron gas, $E_{XC}^{hom}(\rho_0)$ in this approximation is dependent on the homogeneous density ρ_0 and it replaces for the inhomogeneous system with density ρ(r) by

$$E_{XC}^{LDA}\big(\rho(r)\big) = E_{XC}^{hom}(\rho_0)|_{\rho_0}, \tag{2.25}$$

For spin-unpolarised system (where the functional only depends on the density) the LDA for the E_{XC} is given as,

$$E_{XC}^{LDA}[\rho] = \int p(r)\mathcal{E}_{XC}(\rho)dr, \tag{2.26}$$

and

$$\frac{\delta E_{XC}(\rho(r))}{\delta\rho(r)} = \frac{\partial[\rho(r)\mathcal{E}_{XC}(r)}{\partial\rho(r)}, \tag{2.27}$$

Although the approximation is not effective for systems with slowly varying densities, such as weakly perturbed electronic gas, it is effective for systems with inhomogeneous electron densities such as atoms and molecules. Considering the exchange-correlation hole and the pair correlation function, the exchange-correlation energy density becomes.

$$\rho_{XC}^{LDA}(r_1, r_2) = \rho(r_1)[g^{hom}([\rho]; |r_1 - r_2|]\,, \tag{2.28}$$

where $g^{hom}[\rho]$ is the coupling constant integrated pair-correlation part of the pair-correlation function which is unaffected by the coupling constant integration given by,

$$g_{xc}^{LDA}([\rho];\, r_1, r_2) = 1 - \frac{9}{2}\left[\frac{sin\,(k_F(r_1)|r_1-r_2| - k_F(r_1)|r_1-r_2| cos\,((k_F(r_1)|r_1-r_2|)}{(k_F(r_1)|r_1-r_2|)^3}\right]^2 \quad (2.29)$$

where $k_F(r)$ represents a position-dependent local Fermi wave vector denoted by:

$$k_F(r) = (\frac{3}{\pi})^{\frac{1}{3}}\rho(r)^{\frac{1}{3}} \quad (2.30)$$

The E_{XC} is fragmented linearly into exchange and correlation terms as:

$$E_{XC} = E_X + E_C, \quad (2.31)$$

So that the discrete expressions for E_x and E_c can be evaluated. Hence the exchange term transforms to an analytic form for the homogeneous electron gas (HEG). Furthermore, the exchange term is applied under approximation that exchange-energy within a particular system where density is not homogeneous and it is obtained from employment of the HEG results, leading to the expression [79, 80]

$$E_x^{LDA}[\rho] = -\frac{3}{4}(\frac{3}{\pi})^{\frac{1}{3}}\int \rho(r)^{\frac{4}{3}}dr, \quad (2.32)$$

The equation satisfies correct exchange scaling. There are corresponding equations for the correlation part of $[\rho]$ and for $E_C^{LDA}[\rho]$. The LDA exchange-correlation hole is spherical around the reference electron.

$$\rho_{XC}^{LDA}(r_1, r_2) = \rho_{XC}(r_1, s), \quad (2.33)$$

Where $s = |r_1 - r_2|$ and it satisfies the sum rule,

$$\int \rho_{XC}^{LDA}(r_1, r_2)dr_2 = 4r\int_0^\infty \rho_{XC}^{LDA}(r_1, s)\, s^2 ds = -1, \quad (2.34)$$

These equations provide a fundamental understanding of the unlikely success of LDA in intensely inhomogeneous systems. Conversely, the coupling constant averaged exchange-correlation hole can be approximated using LDA. On the other hand, the analytic expressions for the correlation energy of the HEG are only defined in the high-density and low-density limits corresponding to infinitely weak and infinitely strong correlation, respectively. The high-density limit of the correlation energy density is written as [79]

$$\mathcal{E}_0 = Aln(r_s) + B + r_s(Cln(r_s) + D), \quad (2.35)$$

and the low limit

$$\varepsilon_0 = \frac{1}{2}\left(\frac{g_0}{r_s} + \frac{g_1}{r_s^{\frac{3}{2}}} + \ldots ....\right), \tag{2.36}$$

The Wigner-Seitz radius is related to the density as

$$\frac{4}{3}\pi r_s^3 = \frac{1}{\rho}, \tag{2.37}$$

The local density approximations are important as an appropriate property of any approximate E_{XC} functional in the construction of more sophisticated approximations to the E_{XC} including the GGA and hybrid functionals. Hence, the LDA component entails the functional explicitly [80]. Moreover, the LDA explicitly approximates the true density energy through the energy of a local constant's density. However, it fails to approximate in systems where density variations are rapid like in molecules. On the other hand, the local spin density (LSD) is not adequate for most chemical applications which particularly requires the determination of energy variations with considerable precisions. This LSD has been used mainly to calculate the electronic structure in solid-state physics [81, 82]. The LSD approximation is given by

$$E_{XC}^{LSD}\left[\rho_{\uparrow,}\ \rho_{\downarrow}\right] = \int d^3 r \rho(r) \varepsilon_{XC}^{unif}\left[\rho_{\uparrow}(r), \rho_{\downarrow}(r)\right], \tag{2.38}$$

where $\varepsilon_{XC}^{unif}(\rho_{\uparrow,}\ \rho_{\downarrow})$ is the exchange-correlation energy per particle of a uniform electron gas [83, 84, 85].

2.8.2 Generalised Gradient Approximation

The GGA extends the exchange-correlation functional with terms containing gradients of the electron density. Moreover, the GGA provides several distinct parameterisations as compared to the LDA [86]. Hence, since the LDA is limited in approximating the exchange-correlation hole, the solution is the functional exchange correlation with terms containing an electron density gradient. These gradients take measurements of the changes of the electron density and use them to advance the LDA. The theory of the gradient function is based upon the weakly varying electron gas [87]. These approximations are called gradient expansion approximation (GEA) and are denoted by.

$$E_X^{GEA}[\rho] = E_X^{LDA}[\rho] + \beta \int \frac{(\nabla\rho)^2}{\rho^{\frac{4}{3}}} dr + \cdots, \tag{2.39}$$

$$E_C^{GEA}[\rho] = E_C^{LDA}[\rho] + C\int \frac{(\nabla\rho)^2}{\rho^{\frac{4}{3}}} dr + \cdots , \tag{2.40}$$

where β is a constant, and $C(\rho)$ is a function determined by the response theory. However, the rapid difference of realistic densities in atoms and molecules obstructs systematic improvements of GEA over LDA. The analysis of the gradient expansion of the exchange-correlation hole shows that the short-range part (near the reference electron) is enhanced, yet the long-range is worsened [88]. Moreover, the corresponding approximations of the GEA are the generalized gradient approximations (GGA) given by:

$$E_{XC} = E_{XC}[\rho(r), \nabla\,\rho(r)] \ , \tag{2.41}$$

which introduces improvements on the LDA results, and it is superior to the correlated wavefunction methods such as MP2. GGA offers distinct parameterisations relative to the LDA. Hence, the GGA with gradient-corrected functional is written as

$$E_{XC}^{GGA}\left[\rho_{\uparrow,}\ \rho_{\downarrow}\right] = \int d^3 r f(\,\rho_{\uparrow}(r), \rho_{\downarrow}(r), \nabla\,\rho_{\uparrow}, \nabla\,\rho_{\downarrow}) \ , \tag{2.42}$$

This kind of expression decreases LSD atomization energy errors by a factor of approximately 5 [89] . The most used GGA's are the Becke GGA [90] for the exchange energy, and the exchange and correlation GGA's by Perdew [91] and Perdew and Wang [88, 92, 93, 94]. The form of the Becker GGA correlation to the LDA is given as

$$E_x^{GGA}[\rho_{\uparrow}, \rho_{\downarrow}] = E_X^{LDA} - \beta\int \sum_{\sigma} \frac{\rho_{\sigma}(r)^{\frac{4}{3}} x_{\sigma}^2}{1+6\beta x_{\sigma}\, sinh^{-1} x_{\sigma}} d^3 r, \tag{2.43}$$

and

$$E_X^{LDA} = -C_{X\sigma}\sum \rho_{\sigma}^{\frac{4}{3}}(r) d^3(r) \ , \tag{2.44}$$

where $C_X = \frac{3}{2}\left(\frac{3}{4\pi}\right)$, $X_{\sigma} = \frac{|\nabla\rho|}{\rho_{\sigma}^{\frac{4}{3}}}$ and σ denotes electron spins, that is either spin-up (↑) or spin-down (↓). The constant (β) is a parameter used to obtain the correct exchange energy for the nobble gas.

2.9. Plane-wave Pseudopotential

The plane-wave pseudopotential method is a scientific technique used to perform the variation self-consistent solution with relatively high accuracy. The method has been advanced and perfected to reliably predict the static and dynamic properties of

molecules and crystalline solids [94]. The complex many-body problem with strongly correlated electrons and nuclei had been embodied within the framework of the Born-Oppenheimer approximation. On the other hand, the DFT is being mapped to a single-particle problem moving in an effective external potential for a set of fixed nuclei. Moreover, the development of a practical numerical scheme to solve the resulting single-particle Kohn-Shan equation for extended systems such as crystalline solids or liquids have been included in the method [95]. It expands the wavefunction of the single-particle eigenstates of the Kohn-Sham equations into a set of basic functions. Hence, the Schrodinger equation transforms into an algebraic equation for the expansion coefficient solved by the numerical performed method. In short, the plane-wave pseudopotential method deals with weak pseudopotentials and is responsible to perform complete structure optimization, particularly the relaxation of internal parameters. Furthermore, the method can simulate the electronic ground-state for metals, insulators, and semiconductors [95].

2.9.1 Plane-wave Basis Sets

The plane-wave basis sets are mainly utilized in the calculations that involve the boundary conditions. The sets are coupled with pseudopotential or 'effective core potential' in practical performance, to be used as particularly for valence charge density. These plane-wave basis sets are relatively more efficient than the comparative Gaussian-type basis, due to that they are guaranteed to converge to the target wave function. Since there is an infinite number of electrons, a wave function is required for each electron. However, the basis set required for the expansion of each wave function needs to be infinite also. Bloch's theorem offers a solution, by starting with the periodicity of the crystal lattice. The theorem defines that the crystal momentum k is a good quantum number and provides the boundary condition for the single-particle wave function, ϕ_k. Bloch's theorem is often stated in an alternative form:

$$\phi_k(r + R_L) = e^{ik.R_L}\phi_K(r), \tag{2.45}$$

It is equivalent to the statement that all eigenfunction ϕ_{ki} of a single-particle Schoedinger equation with periodic potential can be expressed as a periodic function u_{ki} modulated by a plane wave vector k [96], where R_L is a direct lattice vector.

$$\phi_{kj}(r) = e^{ikr}u_{kj}(r)\ , \tag{2.46}$$

u_{ki} can be expanded as a set of plane-wave basis.

$$u_j(r) = \sum_G C_G^j e^{iG.r} \ , \tag{2.47}$$

and G are reciprocal lattice vectors and the functions u_{ki} are periodic, they can be expanded in a set of plane-waves. Hence the exponential prefactor with the electronic wavefunction is written as:

$$\phi_{kj}(r) = \sum_G C_G^{kj} e^{i(K+G)r} \ , \tag{2.48}$$

where C_G^{kj} is the coefficient of the periodic plane-waves. The number of wavefunctions utilised is controlled by the largest wavefunction in the expansion of equation (2.49). This is equivalent to introducing a cut-off on the kinetic energy of an electron with a wave-vector **k** given by

$$E_K = \frac{\hbar^2|K+G|^2}{2m} \tag{2.49}$$

For only the plane-wave that obeys:

$$E_K = \frac{\hbar^2|K+G|^2}{2m} < E_{cut} \tag{2.50}$$

Are included in the basis. However, the plane-wave set at finite cut-off leads to an error in the computed total energy, therefore the energy must be increased throughout until the calculated energy has converged.

2.9.2 Pseudopotentials

A pseudopotential or an effective potential is used as an approximation of complex systems in physics. They were brought into practice in the year 1930 by Hans Hellmann [103]. Many chemical and physical properties depend mainly on the valence electrons distribution, while the core electrons do not participate in a chemical bonding. However, they are strongly localised around the nucleus, and their wave function overlaps less with the core electron's wave function of the next neighbouring atoms. As a result, the electron core distribution is the same despite the chemical environment an atom is experiencing [102]. Therefore, the core electrons are declared "frozen" and the core electron distribution is kept in the crystal environment. This is adventitious that few electrons must be treated, and few eigenstates of the Kohn-Sham equation must be calculated. Moreover, the removal of core electrons from the calculation reduces the total energy scale which calculates the energy difference between atomic configurations more stable. The introduction of the pseudopotential approximation is an attempt to solve the complex effects of the core electrons in motion and they are nuclear with pseudopotential or an effective potential [97, 98, 99]. Hence the

Schrodinger equation now contains a modified effective term instead of the coulombic potential term for core electrons. Thus, in the pseudopotential approach, only the valence electrons are explicitly dealt with [100, 101, 102, 103, 104]

Figure 2.7 below shows the schematic representation of an atomic all-electron wave function and the corresponding atomic pseudo wave functions, demonstrating the properties of the pseudopotentials. The strong ionic potential causes the valence wave functions to oscillate rapidly in the region occupied by the core electrons. These oscillations maintain the orthogonality between the core electrons and valence electrons. The pseudopotential is contracted in a way that the pseudo wave function has no radial nodes within the core region and the pseudo wave functions and potential agreement with the true wave function and the potential outside the cut-off radius (r_{cut}). The pseudopotential preserves the atomic properties of the elements, with the phase shifts included in the scattering across the core. Generally, the pseudopotential is non-local. Hence it has projectors for different angular momentum states. The general form of the pseudopotential is given by

$$V_{ion} = \sum |lm\rangle V_i \langle lm|, \tag{2.51}$$

where $|lm\rangle$ are spherical harmonics, and V_i is the pseudopotential for angular momentum (l) [96]. The pseudopotentials used in electronic structures are mainly generated from all-electron atomic calculations. The norm-conserving pseudopotential is one of the examples of non-local pseudopotential. It makes use of the different potentials for each angular momentum components of the wave function. The pseudopotential that uses the same potentials for all angular momentum components of the wave function is named local pseudopotential. The local pseudopotential is relatively computationally efficient as compared to the non-local pseudopotential [105, 106]

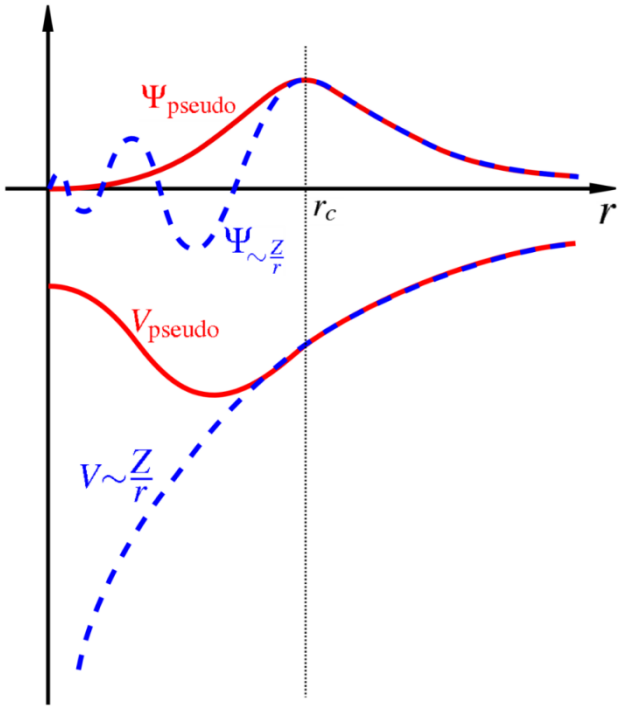

Figure 2.7 Schematic representation of an atomic all-electron wave function and the corresponding atomic pseudo wave functions [107].

(i) Norm-conserving Pseudopotentials

The use of pseudopotentials is important for performing the ab initio calculations. The norm-conserving pseudopotential type, which is non-empirical allows obtaining the pseudo wave functions that are identical to real wave functions beyond a chosen core radius, whose eigenvalues agree with the real eigenvalue [107]. The property gives a correct description of bonding in pseudopotential calculations. Moreover, it corrects the exchange-potentials and self-consistent electrostatics. The Norm-conserving pseudopotentials also produce the scattering power of the full atom potential, correctly at energies away from the bound valence state energy to the first order in the energy difference. As such, the Norm-conserving pseudopotentials reduce all-electron electronic structure calculations with a higher degree of accuracy [108].

(ii) Ultrasoft Pseudopotentials

The ultrasoft pseudopotentials attain smoother pseudo wave function. It is a radical departure from the norm-conserving pseudopotentials. The pseudo wave functions are required to be equal to all-electron wave functions outside the radius. The ultrasoft pseudopotential is capable to reduce the plane-wave cut-off required in calculations, due to large values of radius which can be used in their scheme. Hence the

complication that emerges is two-fold. Those are (1) the equality of the pseudopotentials to the all-electron wave functions in the interstitial while they have different norm inside, the topological complexity, as such they are not normalised. (2) The pseudo charge density is not obtained from computing $\sum \phi^* \phi$ as in the Norm-conserving pseudopotentials; thus, produces incorrect charge. Lastly, the pseudopotentials become less transferable by relaxing the Norm-conservation, however, this is less important.

2.10. Implementation of Plane-wave Pseudopotential Codes

The plane-wave pseudopotential code has been utilised to solve quantum mechanical problems. Some of the used codes include VASP, CASTEP, Win2k and quantum expresso. CASTEP, and VASP [109] (PHONON [110]) codes implemented in Material Studio and MedeA [111] interfaces, respectively. VASP is designed to perform ab initio quantum mechanical calculations, and the molecular dynamics (MD) simulations using pseudopotentials or the projector-augmented wave method and a wave basis set [109]. The implemented approach in VASP is based on the finite temperature with the free energy as a variational quantity and an exact evaluation of the instantaneous electronic ground-state at each MD time state. The package makes use of efficient matrix diagonalization schemes and efficient charge density mixing. The technique can avoid the problems occurring in the original that are based on the simultaneous integration of the electronic and ionic equation motion. The ultra-soft Vanderbilt pseudopotential (US-) [112] and augmented wave (PAW) method are used to describe the interaction between ions and electrons. The methods allow for a considerable reduction of the plane-waves numbers per atom for transition metals. Moreover, VASP can be used to perform calculations on the forces and the full stress tensor, and it can as well be used to relax atoms into their instantaneous ground-state. The VASP code performs a convergence test as the initial test to establish the suitable energy cut-off and k-points sufficient to converge the total energy of the system under investigation. Thereafter properties such as heats of formation, density of states, elastic constants and phonon dispersion curves can be determined.

2.11. Theoretical Background of the Calculated Properties

2.11.1 Heats of Formations

The heats of formation (ΔH_f) and associated entropies provide a fundamental understanding of the stabilities of a compound and a phase diagram construction. The standard enthalpy of formation or standard heat of formation of a compound is the change of enthalpy that goes along with the formation of one mole of a substance in its standard state from its composite elements in their standard state (1 bar and 298K). The heat of formation is estimated from:

$$\Delta H_f = E_c - \sum_i x_i E_i, \tag{2.52}$$

where E_c is the calculated total energy of the compound, E_i is the calculated total energy of the element i in the compound. The heats of formations are used to predict the stability trend of the materials [113].

2.11.2 Density of States

The density of states (DOS) of a system describes the number of states per interval of energy at each available energy level. They further indicate how dense the packed quantum states are in a system. The integration of DOS over a range of energy gives several states as:

$$N(E) = \int_E^{\Delta E} g(Eg(E))dE\ , \tag{2.53}$$

Where $N(E)$ represents the carrier density and $g(E)dE$ denotes the number of states between E and dE. The DOS allows for the integration to be performed for the electron energy instead of the integration over the Brillouin zone. The presence of suppression in the electronic density of states (pseudo gap) at the Fermi level is established in the case of metal phosphates. This has led to a question in the study of complex metal phosphates systems, that how the pseudo gap forms in the electronic density of states at the Fermi level and their relations to the stability of structures. Hence, numerous contexts such as Jahn-Teller effects in molecules [114], the colouring patterns of atoms over the sites of a given lattice, [115] and Hume-Rother rule [116] have proposed the direct relations between the formation of a pseudo gap and stability of the structure.

Literature reveals that the density of states is essential in determining the stability trend of structures for the Fermi level (E_f). Conversely, the theory suggests a fundamental background that a structure with the highest density of states around the Fermi level is the least stable, while the structure with the lowest density of states is the most stable [117, 118].

2.11.3 Phonon Dispersion Curves

The phonon dispersion curves are defined as the k wave vector dependence of the frequencies $\omega(k,j)$ of the normal modes for all branches j and selected directions in a crystal. The phonon dispersion curves have an essential role in most physical properties of condensed matter physics. These include thermal conductivity, mechanical stability, and electrical conductivity. Moreover, they are an indication of an excited state in quantum mechanical quantization for the vibrational modes of elastic structures with interacting particles. The behaviour of phonon dispersion branches reflects some features of a crystal structure and its interatomic interactions. Hence, they provide the most comprehensive and detailed information about the dynamical properties of a crystal. The calculations of phonon vibrational frequencies are given as:

$$\omega = v_i q \tag{2.54}$$

where v_i is the speed and q is a wave-vector of the lattice vibrations; In cases where crystals consist of more than one types of atoms, two types of vibrational modes are displayed; that is: optical and acoustic.

The optical phonons come from the out of phase vibrations between neighbouring atoms within the unit cell, while the in-phase vibrations give rise to acoustic phonons. The acoustic modes have zero frequency at $q = 0$ (the centre of the Brillouin zone), and contrary to that, the optical modes have non-zero frequencies. The two modes (acoustic and optical) split into longitudinal and transverse modes named longitudinal acoustic (LA), transverse acoustic (TA), longitudinal optical (LO) and transverse optical (TO). The acoustic modes display a linear relationship between frequency and long wavelengths phonon wave-vector. The negative vibrational frequencies known as soft modes indicates mechanical instability of systems in the study, and positive vibrations indicate stability. More attention is paid along with the Γ point, where there are points of high symmetry. Table 2.1 below list and describe the critical k-points of

high symmetry line in the first Brillouin zone for certain Bravais lattice of BCC, FCC, and hexagonal lattice [119, 120]. Phonon dispersions curves for various crystal directions rely on this notation. These demotions describe the direction and symmetry of a crystal.

Table 2.1 Critical k-points in the first Brillouin zone [113]**.**

Symbol	**Description**
Γ(0,0,0)	Centre of the Brillouin zone
Simple cube	
M (1/2,1/2,0)	Centre of an edge
R (1/2,1/2,1/2)	Corner point
X (0,1/2,0)	Centre of a face
Body-centred cubic	
H (-1/2,1/2,1/2)	Centre point joining four edges
P (1/4,1/4,1/4)	Corner point joining four edges
N (0,1/2,0)	Centre of a face
Face-centred cubic	
K (3/8,3/4,3/8)	Middle of an edge joining two trigonal faces
L (1/2,1/2,1/2)	Centre of a trigonal face
U (1/4,5/8,5/8)	Middle of an edge joining a trigonal and a square face
W (1/4,4/8,1/2)	Corner point
X (0,1/2,1/2)	Centre of the square face
Hexagonal	
A (0,0,1/2)	Centre of a hexagonal face
K (2/3,1/3,1/2)	Middle of an edge joining two rectangular face
H (1/2,0,0)	Corner point
L (1/2,0,1/2)	Middle of ab edge joining a hexagonal and a rectangul face
M (1/2,0,0)	Centre of a rectangular face

2.11.4 Elasticity

The elastic properties relate to different fundamental solid-state properties. These properties include phonon spectra, lattice constants, equation of states and interatomic

potentials. They provide crucial information about the strength of materials against an externally applied strain. They also act as stability criteria to probe mechanical stability and structural transformation [121, 122]. The elastic constants of a material provide detailed information about the response of the material to the externally applied strain required to maintain a given deformation. Furthermore, they provide more information with the strength of a material by characterizing it from bulk modulus (B), shear modulus (G), Young's modulus (E), shear anisotropy factor (A) and Poisson's ration (v).

The calculations of elastic constants were initiated by Born [123]. The Born stability criteria are a set of conditions for the elastic constants (C_{ij}) that are related to the second-order change in the internal energy of a crystal under formation. However, the range of Born stability is more sensitive to the choice of coordinates [124]. Moreover, it was suggested that Born conditions are not effective for the stressed systems and they are effective for only the unstressed systems [125]. On the other hand, Barron and Klein indicated that the definition of the elastic constants derived the Helmholtz free energy, and they cannot be applied directly to the study of the stress-strain relationship in a stressed system [126]. However, it was demonstrated that the elastic constants cannot be used as a stability criterion for stressed systems [125, 127]. They suggested the use of elastic stiffness coefficients as stability criteria for isotropic stress. They further obtained a more general form for anisotropic stress, from the path-dependent finite displacement. The stability criteria are framed in terms of the elastic stiffness coefficients which governs proper relations of stress and strain at finite strain by considering both internal and the external work was done during the process of deformation [128]. This indicates that the stability analysis can be determined by an appropriate generalization of the zero-stress elastic constants valid for arbitrary stress.

Since bulk modulus can measure the degree of stiffness or the energy required to produce a given volume deformation, it is one of the significant parameters to characterise the physical property of a material. Shear modulus describes the resistance to shape change caused by shearing force. Young modulus reflects the resistance of a material against uniaxial tension [129]. Moreover, bulk modulus depicts a bonding character within a material. Hence is it used as an indicator for strength and hardness of the material, and it is an inverse of compressibility [130]. The ration of bulk to shear modulus (B/G) of polycrystalline phases, states that the shear and bulk moduli signify the resistance to plastic deformation and the resistance to fracture, respectively [130]. A high B/G value is

associated with ductility, and a low B/G is related to brittleness. The critical value separating ductility and brittleness is 1.75 [131].

(i) Elastic Stability Criteria

Many criteria have been introduced to deduce the elastic stability of crystals and they vary for difference lattice crystals. That is, the stress and strain for an individual material have three tensile and three strain shear components, leading to six components in total. As such, a relationship between stress and strain is then defined by a 6x6 symmetry matrix with 36 elements; where only 21 elements are independent and given by the equation: $\sigma_1 = C_{ij}\varepsilon_j$, where σ is for stresses and ε for strain. The structural symmetry of the crystal uses some of the matrix elements that are equal and others fixed at zero. Cubic crystals consist of three independent elastic constants (C_{11}, C_{12}, and C_{44}). The bulk, shear, Young's modulus and Poisson's ration for the cubic crystal are given by [79, 85].

$$E = \frac{9BG}{3G+G}, \qquad v = \frac{E}{2G-1}, \qquad G_v = \left[\frac{C_{11}-C_{12}+3C_{44}}{5}\right], G_R = \left[\frac{C_{44}(C_{11}-C_{12})}{4C_{44}+3(C_{11}+C_{12})}\right],$$

$$G = G_H = \left[\frac{G_V+G_R}{2}\right], \qquad B = \left(\frac{c_{11}-2c_{12}}{3}\right), \qquad c' = \frac{c_{11}-c_{12}}{2},$$

$$A = \frac{2C_{44}}{C-C_{12}}, \qquad v = \frac{C_{12}}{C_{11}+C_{12}} \tag{2.55}$$

where E is Young's modulus, v Poisson's ratio, G isotropic shear modulus, B bulk modulus, c' tetragonal shear modulus, and A the Zener anisotropic factor. The Hill average is selected as the estimation of bulk modulus and shear modulus.

The mechanical stability requirements for cubic crystal yield the conditions for stability on the elastic constants, these conditions are as follow:

$$(c_{11}-c_{12})>0, \quad (c_{11}+2c_{12})>0, \ c_{11}>0, \ and \quad c_{44}>0 \tag{2.56}$$

The requirements for mechanical stability in hexagonal structures are [132]:

$$C_{11}>0, C_{11}-C_{12}>0, C_{44}>0, C_{11}+C_{12}-\frac{2C_{13}^2}{C_{33}}>0 \ and \ C_{66}=\frac{C_{11}-C_{12}}{2}>0 \tag{2.57}$$

for orthorhombic crystals, the mechanical stability conditions are given by [133]

$$C_{11}+C_{12}+C_{33}+2C_{12}+2C_{23}>0, \qquad C_{22}+C_{33}-2C_{13}>0,$$
$$C_{11}>0, \ C_{22}>0, \ C_{33}>0,$$
$$C_{44}>0, \ C_{55}>0, \ C_{66}>0 \tag{2.58}$$

Lastly, the mechanical stability conditions for trigonal crystal are [134]

$$C_{44} > 0, \quad C_{66} > 0, \qquad C_{11} > 0, \; C_{33} > 0, C_{11} - C_{12} > 0, \qquad (C_{11} + C_{33} - 2C_{13}) > 0,$$
$$(2C_{11} + C_{33} + 2C_{12} + 4C_{13}) > 0 \tag{2.59}$$

Chapter 3: Structural, Electronic and Vibrational Properties of $LiMO_2$ (M: Mn, Ni and Co)

3.1 Introduction

This chapter presents results obtained from the first-principles density functional theory (DFT) calculations with an aid of Hubbard correction (DFT+U) performed on $LiMnO_2$, $LiNiO_2$ and $LiCoO_2$ structures cathode materials. The DFT has provided a convenient first principle framework for investigating the convergence test of the structures particularly the cut-off energy, k-points and convergence parameters. Moreover, it is critical to calculating structural parameters such as lattice parameters.

The structural properties provide detailed information about the materials crystal nature. The electronic properties particularly the band structures, Density of States (DOS) and phonon dispersion curves will be analysed and discussed to enable better understanding of the electrical conductivity and vibrational stability of the structures. The significance of the Hubbard U parameter on the electronic density of states (DOS), band structures and the crystal structure will be discussed. Moreover, the electronic properties calculations on the materials help mainly in understanding the conductivity of the materials. On the other hand, mechanical properties give details about the vibrational stability of the structures. These properties are evaluated from the electronic band structure, density of states and phonon dispersion curves. The calculations of the properties in the study provide insight into the crystal nature of the materials under investigation. Furthermore, they provide insight into the conductivity behaviour of the materials, together with the electron contributions constituting the behaviours. The electronic band structures provide the electronic levels in crystal structures, which are characterized by two quantum numbers, the Bloch vector k and the band index n and structures [135]. Many electrical, optical and even magnetic properties of crystals can be explained in terms of the band structure. the density of states (DOS) of a system help in describing the number of states that are to be occupied by the system at each level of energy. They are an average over space and time domains of the various states occupied by the system. For mechanical stability, phonons dispersion curves describe an elementary vibrational motion in which a lattice of atoms or molecules uniformly oscillates at a single frequency [136]. Elastic

constants describe properties of material undergoing stress, deforms, and their recoveries and return to its original shape after the stress ceases.

3.2 Structural Properties of $LiMO_2$ (M: Mn, Ni and Co)

The layered parent bulk structures ($LiMO_2$: M=Mn, Ni, and Co) in this work have a Bravais lattice of rhombohedral centred hexagonal with the space group symmetry $R\bar{3}m$. The bulk structure has alternative layers of Li^+ and $(MO_2)^-$ in which a transition metal (M) is stable as low-spin M^{3+} and situated at the centre of an octahedron formed by oxygen atoms. The illustrated structure in figure 3.1 below is for $LiMO_2$ (M: Co, Mn and Ni). The material is ordered with Li^+, M^{3+} and O^{2-} [137]. The structural properties are tabulated in table 3.1. The vectors that describe the positions of atomic nuclei within the crystal structure are illustrated in table 3.2.

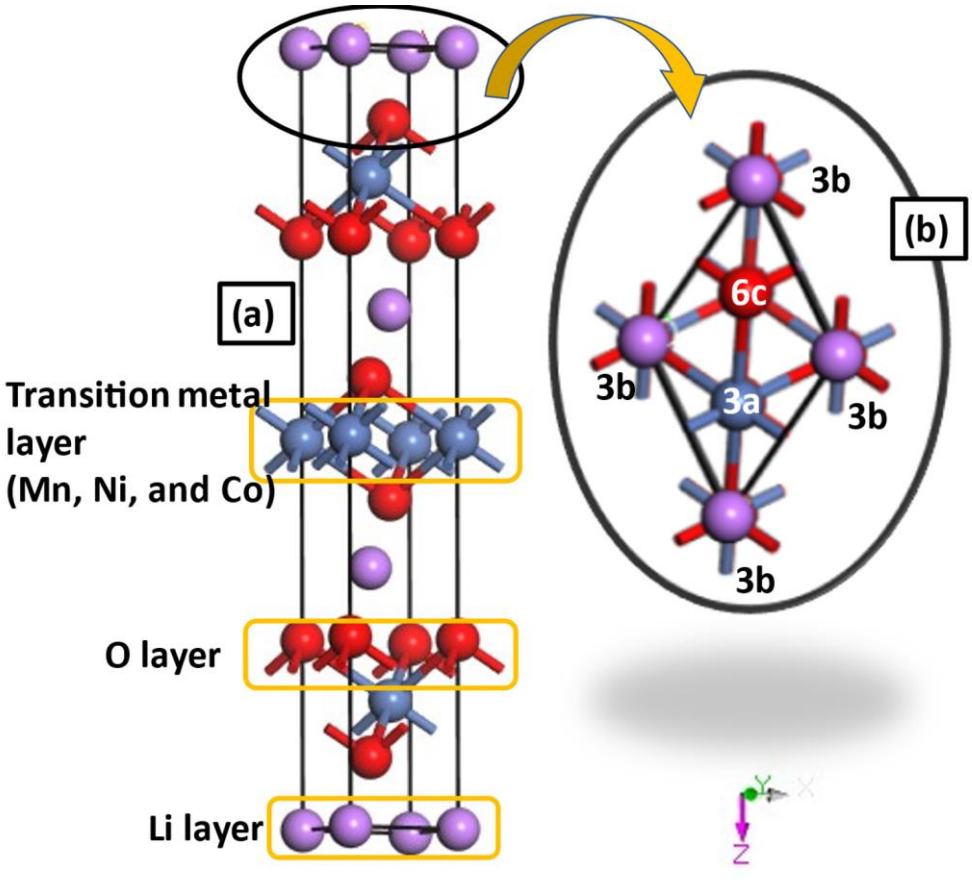

Figure 3.1 (a) The 3D layered parent bulk of $LiMO_2$ (M: Mn, Ni and Co) with Bravais lattice of rhombohedral cantered hexagonal and (b) top view representation of co-ordinated sites for $LiMO_2$ (M: Mn, Ni and Co).

Table 3.1 Structural properties of $LiMO_2$ (M: Mn, Ni, and Co)

Structure	$LiMnO_2$	$LiNiO_2$	$LiCoO_2$
Lattice Parameters(Å)	a=3.002 [138] c=14.550 [138]	a=2.881 [139] c=14.198 [139]	a=2.830 [140] c=14.119 [140]
Volume ($Å^3$)	105.345 [141]	102.057 [139]	96.466 [140]
Space Group	$R\bar{3}m$ [142]	$R\bar{3}m$ [142]	$R\bar{3}m$ [142]

Table 3.2 Fractional coordinates and atomic positions of $LiMO_2$ (M: Mn, Ni, and Co) [190]

Atoms	Positions	x	y	z
Li	3b	0	0	1/2
Mn	3a	0	0	0
Ni	3a	0	0	0
Co	3a	0	0	0
O	6c	0	0	0.2584

3.3 Method

3.3.1 Convergence Test

A convergence test establishes the suitable energy cut-off and k-points sufficient to converge the total energy of a system under consideration [113]. Thereafter properties such as heats of formations, density of states, elastic constants and phonon dispersion curves can be calculated. The cut-off energy provides more information about the cut-off on the number of plane waves functions being utilized as basic functions to represent the wave function. It is used to fix the number of plane waves in the basis set, rather than a straightforward option of choosing the number of plane waves. The k-points are sampling points in the first Brillouin zone of material, they help in converging the total energy of a system [113].

(i) Kinetic Energy Cut-off

To ensure the appropriate cut-off energy of the structures, the single point energy were calculated at fixed k-points of 5x5x2 for both the $LiMnO_2$ and $LiNiO_2$ and 4x4x2 for

$LiCoO_2$. All calculations were performed within the GGA-PBE embedded within the CASTEP code. Figure 3.2 depicts the curves for total energy per atom against the kinetic energy cut-off for(a) $LiMnO_2$, (b) $LiNiO_2$ and (c) $LiCoO_2$ materials. The cut-off energy of 550 eV was chosen for $LiNiO_2$ and $LiCoO_2$, and 500 eV for $LiMnO_2$ because they were energies that gave a zero slope [143].

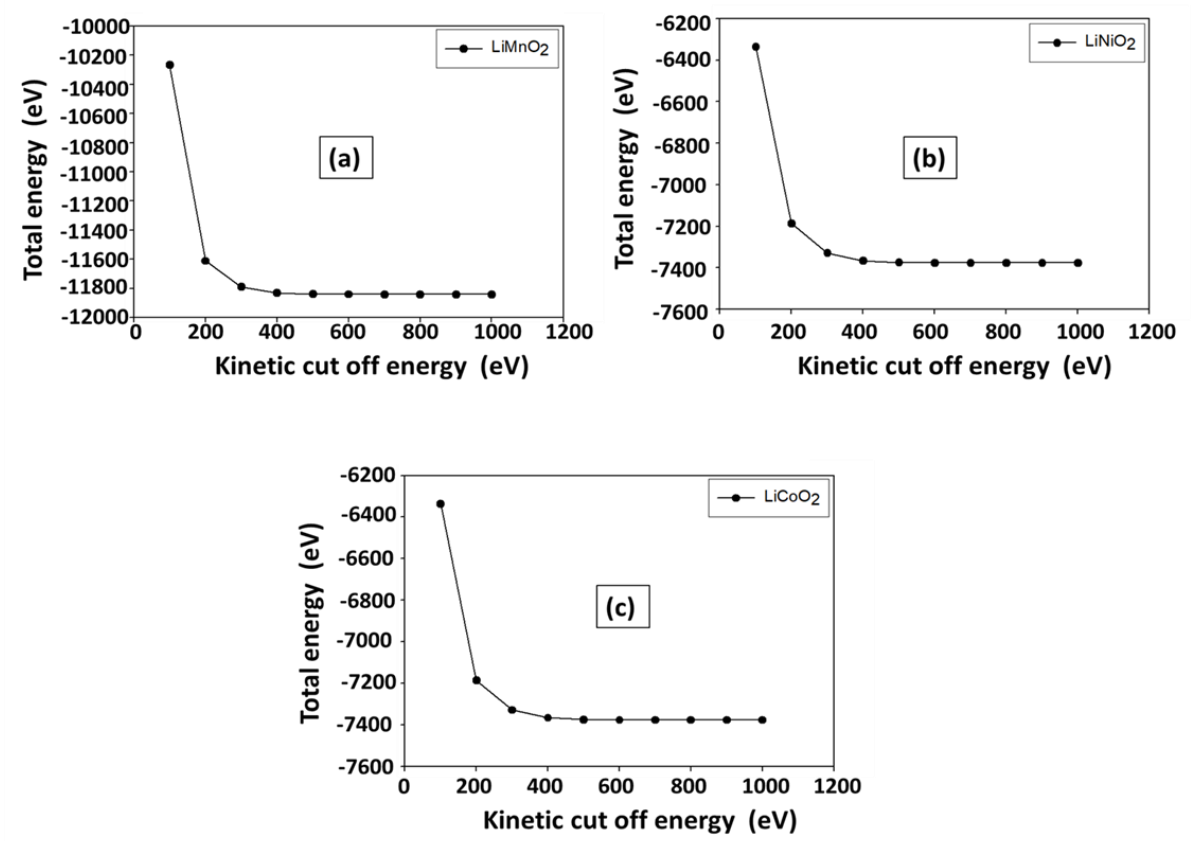

Figure 3.2 Graphical representation of total energy per atom versus kinetic cut-off energy of (a) $LiMnO_2$, (b) $LiNiO_2$ and (c) $LiCoO_2$.

(ii) K-Points

This subsection outlines the convergence of the final energies with the k-point sampling set size. The energy calculations were performed using fixed cut-off energies, thus 550 eV for $LiNiO_2$ and $LiCoO_2$ and 500 eV for $LiMnO_2$. The graphical representation of the final energy versus k-points is shown in figure 3.3 below.

On the other hand, the convergence test calculations were performed with the same energy varying the k-points. The final energy for the number of k-points for all materials converged when the final energy per atom (final energy difference between two consecutive points) was less than 0.5 eV. As a result, the k-points mesh of 5x5x2

converged for $R\bar{3}m$ $LiMnO_2$ and $LiNiO_2$ materials, and the k-point mesh of 4x4x2 converged for $R\bar{3}m$ $LiCoO_2$ material. The cut-off energy of 550 eV and the k-mesh of 5x5x2 will be employed to perform the electronic properties of the $LiNiO_2$, 550 eV with 4x4x2 k-mesh for $LiCoO_2$ and 500 eV with 5x5x2 for $LiMnO_2$.

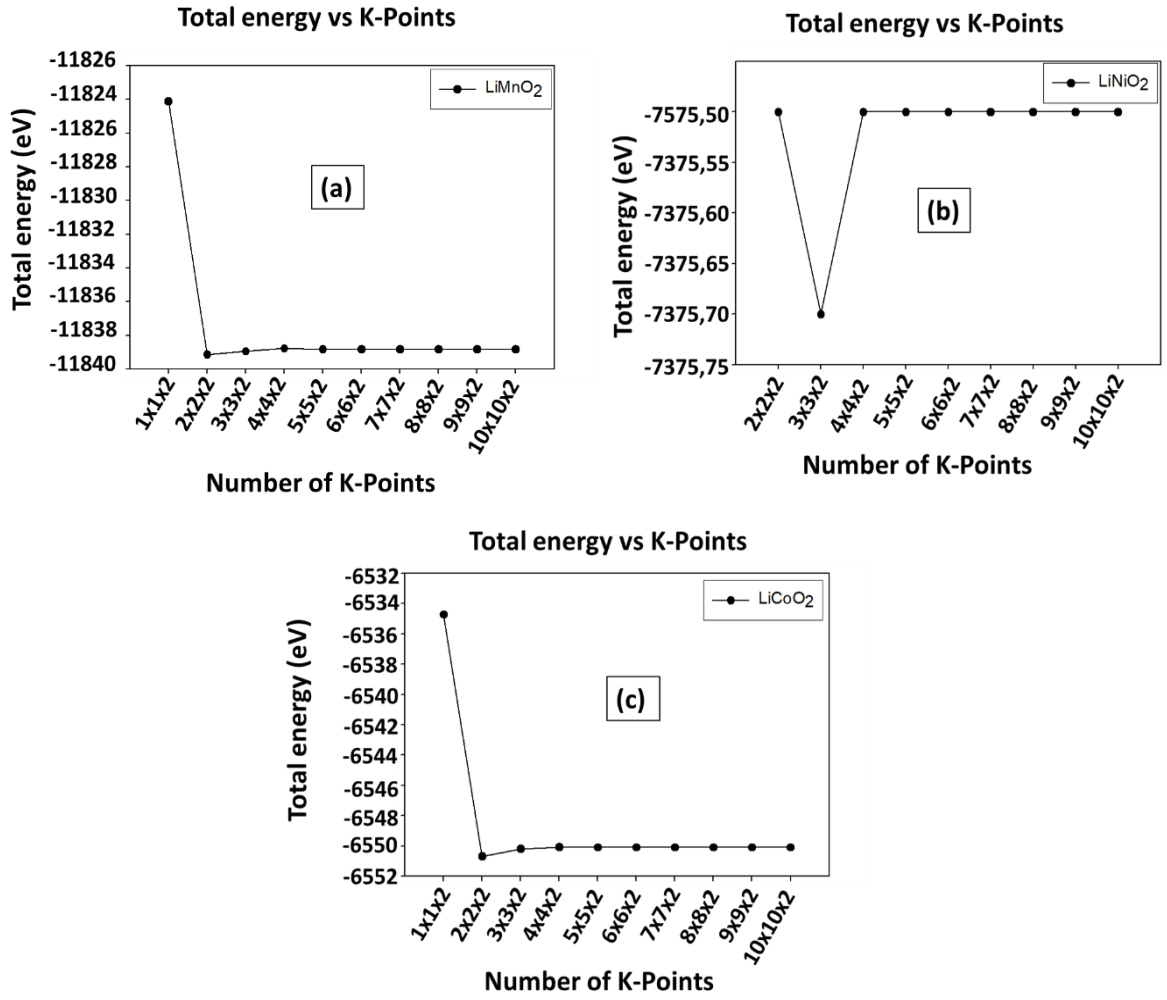

Figure 3.3 Graphical representation of final energy versus k-points for (a) $LiMnO_2$, (b) $LiNiO_2$ and (c) $LiCoO_2$.

3.4 Results

3.4.1 Geometry Optimization

Structural relaxation (optimization) was performed, during which the lattice and cell volume of the structure were allowed to change until the structures were fully relaxed. This is significant to obtain a ground state structure or minimum total energy of the crystal structure before the determination of other properties. The structural optimization was performed using the CASTEP code [144] discussed in chapter 2

using the cut-off energy and k-points mesh as stated in the above section. The parameters of the relaxed structures are shown in table 3.3 below.

Table 3.3 The parameters for optimised and experimental structures

Structures	Optimised Structures			Experimental Structures	
	Lattice Parameters (Å)	**Cell volume (Å^3)**	**Cell Angles (°)**	**Lattice Parameters (Å)**	**Cell volume (Å^3)**
$LiNiO_2$	a=b= 2.890 c=14.222	102.891	Alpha=beta=90 Gamma=120	a=b= 2.881 [139] c=14.198 [139]	102.057 [139]
$LiMnO_2$	a=b= 2.841 c=14.488	102.258	Alpha=beta=90 Gamma=120	a=b=3.002 [138] c=14.550 [138]	105.345 [141]
$LiCoO_2$	a=b= 2.850 c= 13.992	98.992	Alpha=beta=90 Gamma=120	a=b= 2.830 [140] c= 14.119 [140]	96.466 [149]

3.4.2 Derivation of Hubbard U Parameters

The Hubbard U parameter is mainly used to correct the electron self-interactions in DFT by localizing electrons in strongly correlated systems [145]. However, the correct U parameter must be derived per element. It is not the same for oxidation states of a given element and it significantly perturbs the electronic structure of material [146, 147]. As such, the choice of U parameters was initiated to produce a relative bandgap in agreement with the experimental data range. The process of determining the suitable U parameter is a trial and error process guided by the cut-energy and the k-points which allows a complete optimization of the structures. The cut-off energy and k-mesh for each structure as stated above were not varied in table 3.3, only the U parameter was changed. This is represented in table 3.4 below. In this case, the 500 eV with 5x5x2 k-mesh for the $R\bar{3}m$ $LiMnO_2$ material was sufficient to the U of 4.25 eV in Mn^{3+} transition metal. The 550 eV with 5x5x2 k-mesh on $R\bar{3}m$ $LiNiO_2$ matched the U of 2.45 eV in Ni^{3+} transition metal, and 550 eV with 4x4x2 k-mesh on $LiCoO_2$ matched to U of 6.10 eV in Co^{3+} transition metal.

Table 3.4 Representation of Hubbard U parameters per transition metal.

Transition metals	Mn^{3+}	Ni^{3+}	Co^{3+}
U (eV)	4.25	2.45	6.10

The use of these U parameters produced band gaps in good agreement with the experimental gaps, and they had a relatively small difference as compared to other theoretical findings. The comparison of the U parameters results to theoretical and experimental U is displayed in table 3.8 below.

3.4.3 Structural Properties of $LiMO_2$ (M: Mn, Ni and Co)

The equilibrium structural properties were performed from the geometry optimisation calculation within the generalised gradient approximation. The calculations were performed using an energy cut-off of 500 eV for $LiMnO_2$ and 550 eV for $LiNiO_2$ and $LiCoO_2$. The k-points of 5x5x2 for $LiMnO_2$ and $LiNiO_2$, and 4x4x2 for $LiCoO_2$. Lastly, the U parameters used in the d state of the materials were 4.25 eV, 2.25 eV and 6.10 eV for $LiMnO_2$, $LiNiO_2$ and $LiCoO_2$, respectively.

(i) $LiMnO_2$

Table 3.5 lists the calculated and experimental lattice parameters, cell volumes and heats of formation for $LiMnO_2$. The orthorhombic $LiMnO_2$ (space group $R\bar{3}m$) gave lattice parameters; a=b=2.841 **Å** and c=14.488 **Å** at an ambient pressure that corresponds to the cell volume of 101.258 **Å^3**. The calculated lattice parameters are in good agreement with the experimental results (a=b=3.002 **Å** and c=14.550 **Å**) [138] with a percentage difference of 5.51% for *a,b* and 0.43% for *c*. Moreover, the calculated volume (101.258 **Å^3**) is well predicted and compares well to the experimental volume (105.345 **Å^3**) [141], to within 3.96% which is typical for the DFT for transition metal phosphates [148]

Table 3.5 Calculated and experimental lattice parameters, volume, and heats of formation for orthorhombic $LiMnO_2$.

Structure $LiMnO_2$ (Space group $R\bar{3}m$)		
Properties	**Simulated**	**Experimental**
Lattice Parameters (Å)	a=b= 2.841	a=b=3.002 [138]
	c=14.488	c=14.550 [138]
ΔH_f (eV/atom)	-0.330	
Volume ($Å^3$)	101.258	105.345 [141]

The calculated heat of formation is given in table 3.5. The lower the heat of formation, the more stable the structure. That is at ambient pressure, the o-$LiMnO_2$ structure gives the heat of formation of -0.330 eV/atom. This implies that the o-$LiMnO_2$ is energetically favourable since it displays the negative ΔH_f value. The ΔH_f value suggests the stability of o-$LiMnO_2$. The lattice parameters and the heat of formation suggest structural stability on the o-$LiMnO_2$ structure.

(ii) $LiNiO_2$

Table 3.6 is a list of the calculated and experimental lattice parameters, cell volumes and heats of formation for $LiNiO_2$. The orthorhombic $LiNiO_2$ (space group $R\bar{3}m$) gave lattice parameters; a=b=2.890 **Å** and c=14.222 **Å** at an ambient pressure that corresponds to the cell volume of 102.891 $Å^3$. The calculated lattice parameters give a good agreement to the experimental results (a=b=2.881 **Å** and c=14.198 **Å**) [139] with a percentage difference of 0.31% for *a,b* and 0.17% for *c*. Moreover, the calculated volume (102.891 $Å^3$) is well predicted and compares well to the experimental volume (102.057 **Å**^{3}) [139], to within 0.81% which is typical for the DFT for transition metal phosphates [148].

Table 3.6 Calculated and experimental lattice parameters, volume, and heats of formation for orthorhombic $LiNiO_2$

Structure $LiNiO_2$ (Space group $R\bar{3}m$)		
Properties	**Simulated**	**Experimental**
Lattice Parameters (Å)	a=b= 2.890	a=b= 2.881 [139]
	c=14.222	c=14.198 [139]
ΔH_f (eV/atom)	-0.455	
Volume ($Å^3$)	102.891	102.057 [139]

The predicted heat of formation is given in table 3.6. The lower the heat of formation, the more stable the structure [113]. That is at ambient pressure, the o-$LiMnO_2$ structure gives the heat of formation of -0.455 eV/atom. This implies that the o-$LiMnO_2$ is energetically favourable since it displays the negative ΔH_f value. The ΔH_f value suggests the stability of o-$LiNiO_2$. The lattice parameters and the heat of formation suggest structural stability on the o-$LiNiO_2$ structure.

(iii) $LiCoO_2$

Table 3.7 lists the calculated and experimental lattice parameters, cell volumes and heats of formation for $LiCoO_2$. The orthorhombic $LiCoO_2$ (space group $R\bar{3}m$) gave lattice parameters; a=b=2.850 Å and c=13.992 Å at an ambient pressure which corresponds to the cell volume of 98.992 $Å^3$. The calculated lattice parameters give a good agreement to the experimental results (a=b=2.830 Å and c=14.119 Å) [140] with a percentage difference of 0.70% for *a,b* and 0.90% for. Moreover, the calculated volume (98.992 $Å^3$) is well predicted and compares well to the experimental volume (96.466 $Å^3$), to within 2.58% which is typical for the DFT for transition metal phosphates [148]

Table 3.7 Calculated and experimental lattice parameters, volume, and heats of formation for orthorhombic $LiCoO_2$

Structure $LiCoO_2$ (Space group $R\bar{3}m$)		
Properties	**Simulated**	**Experimental**
Lattice Parameters (Å)	a=b= 2.850	a=b= 2.830 [140]
	c= 13.992	c= 14.119 [140]
ΔH_f (eV/atom)	-0.432	
Volume ($Å^3$)	98.992	96.466 [149]

The predicted heat of formation is given in table 3.7. The lower heat of formation, the more stable the structure. That is at ambient pressure, the o-$LiCoO_2$ structure gives the heat of formation of -0.432 eV/atom. This implies that the o-$LiCoO_2$ is energetically favourable since it displays the negative ΔH_f value. The ΔH_f value suggests the stability of o-$LiCoO_2$. The lattice parameters and the heat of formation suggest structural stability on the o-$LiCoO_2$ structure.

3.4.4 Electronic Properties

The focus of this section is on the band gaps, which represents a range of energy levels in the materials that do not allow electrons to possess. Although materials may have different band gaps within their electronic structure, it is essential to pay much attention to the Fermi level band gaps. This is an energy level where electrons exist when a material is at absolute zero temperature (E_f = 0 eV). The band gap sizes are used to classify the nature of materials, either being a metal, semiconductor, or insulator. Moreover, the influences of the band gaps on materials conductivity are discussed.

Herein, the electronic properties of $LiMnO_2$, $LiNiO_2$ and $LiCoO_2$ with the $R\bar{3}m$ space group are outlined, particularly the band structures, the density of states and phonon dispersion graphs. As the initial point, the same cut-off energy and the k-mesh are used as fundamental parameters although the energy gap is the centre of focus. The Hubbard U parameter is adjusted to obtain a bandgap that falls within the experimental range of the same materials. This will have a major impact when doping the materials. The comparison of the simulated conductivity results (band gaps), with the simulated bandgaps from other works and the experimental data is shown in table 3.8.

Table 3.8 Comparisons of simulated and experimental band gaps (eV) using the density functional theory.

Systems	Our work	Other works (eV)				Experimental (eV)
		PBE+U	PBE+U+D3	SCAN	SCAN+D3	
$LiMnO_2$	1.64	1.42 [150]	1.42 [150]	1.19 [150]	1.11 [150]	1.64 [151]
$LiNiO_2$	0.40	HM[a] [150]	HM[a] [150]	HM[a] [150]	HM[a] [150]	0.40 [152]
$LiCoO_2$	2.22	2.22 [150]	2.26 [150]	1.74 [150]	1.96 [150]	2.10-2.27 [153]

HM[a] = half-metal [150]. The bandgap is zero.

3.4.5 Band Structures

To understand and find the possible synthesizing routes for $LiMnO_2$, $LiNiO_2$, and $LiCoO_2$, it is critical to probe their electronic structures. Figure 3.4 depicts the calculated electronic band structures around the Fermi level (E_f) set at 0 eV for the antiferromagnetic (low spin) state. These electronic band gaps are produced from the same cut-off energy, k-mesh and U parameters. Presented by the graphs in figure 3.4 are energy electrons in different bands versus high symmetry k-points (wave vector). For comparisons purposes, the band dispersion is plotted along with the high symmetry points G→A→H→K→G→M→L→H.

Figure 3.4 (a) illustrate the electronic band structure of $LiMnO_2$ material. The graph represents energy electrons in different bands versus high symmetry k-points. The electronic band structure of $LiMnO_2$ consists of 51 bands and the bands originate from 3d orbitals of the transition metals Mn. The bottom bends predominantly form the 2p orbitals of the two O atoms in the compounds. On the other hand, the top levels denote Mn-3d bands, and the bottom levels as O-2p bands respectively in the structures as bonding properties. These bonding properties are split by the ligand field (Fermi level, E_f at 0 eV) into upper antibonding e_g bands and nonbonding t_{2g} bands with distinct energy gap Δ_0 [45, 46, 47]. In the valence band, the Mn-3d states are shifted to below -75 eV, and they are shifted to higher energy in the conduction band. The conduction and the valence bands are unoccupied with a bandgap of 1.64 eV in good agreement

with the experimental value of 1.64 eV [151]. This value (1.64 eV) can be attributed to insulator behaviour and low electrical conductivity in $LiMnO_2$.

The electronic band structure of $LiNiO_2$ is shown in figure 3.4 (b), the structure contains 39 bands. The bands mainly originate from 3d orbitals of the transition metals Ni. Moreover, the bottom bends predominantly form the 2p orbitals of the two O atoms in the compounds. The top levels denote Ni-3d bands and the bottom levels as O-2p bands in the structures as bonding properties. These bonding properties are split by the ligand field (Fermi level, E_f at 0 eV) into upper antibonding e_g bands and nonbonding t_{2g} bands with distinct energy gap Δ_0 of 0.40 eV. The bandgap is in good agreement with the experimental value of 0.40 eV [152]. The small bandgap in the material suggests that the $LiNiO_2$ structure has a semiconductor behaviour characteristic with high electrical conductivity [45, 46, 47].

Figure 4.3 (c) is the electronic band structure of $LiCoO_2$ material. The plot representing the structure has 42 bands, where the bands mainly originate from 3d orbitals of the transition metals Co. The bottom bands of the structure predominantly form the 2p orbitals of the two O atoms in the compounds. Thus, the top levels denote Co-3d bands and the bottom levels as O-2p bands as bonding properties. Moreover, these bonding properties are split by the ligand field (Fermi level, E_f at 0 eV) into antibonding e_g bands and nonbonding t_{2g} bands with distinct energy gap Δ_0 of 2.22 eV [45, 46, 47]. The energy gap falls within the experimental range of energy gaps 2.10-2.27 eV [153], which suggests an insulator behaviour characteristic in the structure with low electrical conductivity.

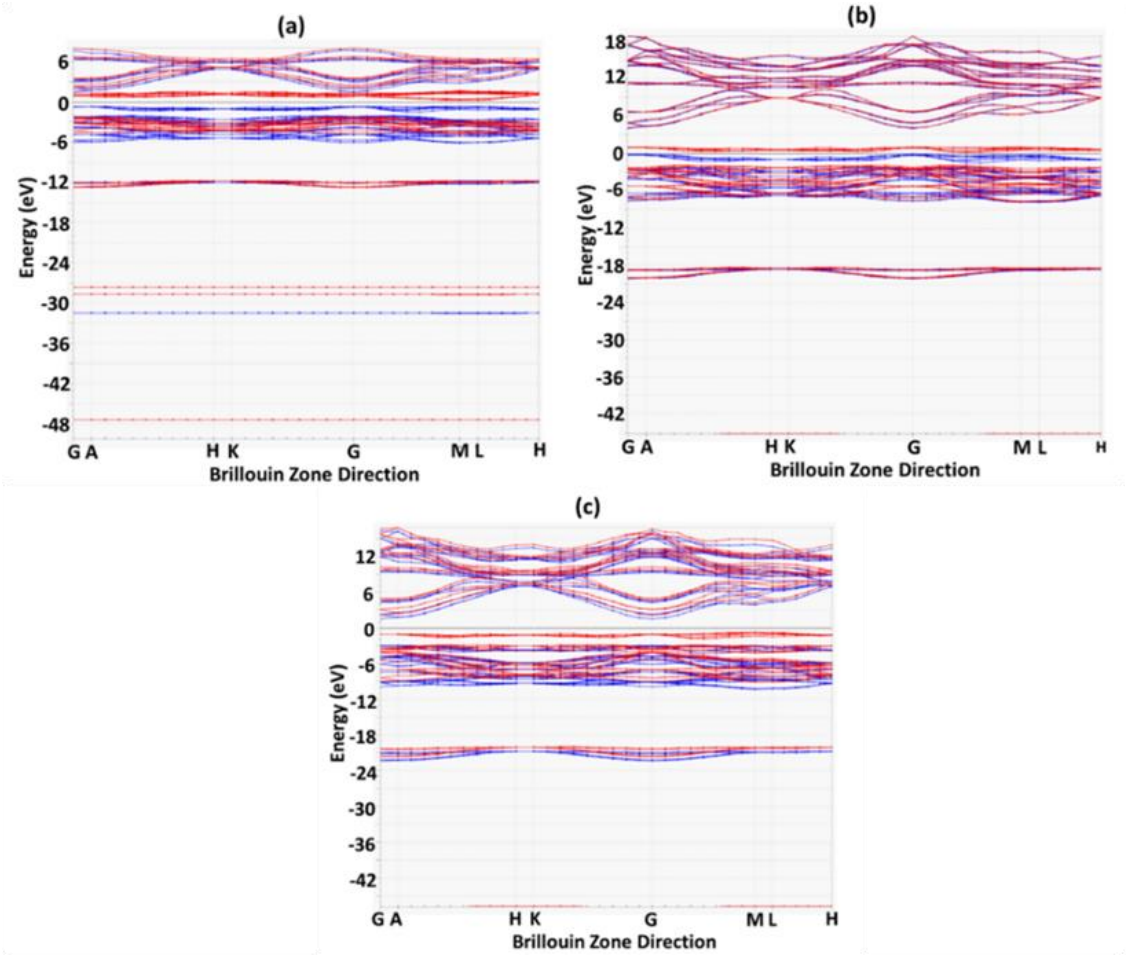

Figure 3.4 Graphical representation of band structures for (a) $LiMnO_2$, (b) $LiNiO_2$ and (c) $LiCoO_2$ material with low spin state.

3.4.6 Density of States

Structural conductivity is fundamentally related to details of the Fermi surfaces. For conductivity examination of the $LiMnO_2$, $LiNiO_2$ and $LiCoO_2$ structures, the electronic density of states is considered, from which the differences of electronic structures in these materials are analysed. The TDOS (total density of states) and the PDOS (partial density of states) graphs of the $LiMnO_2$, $LiNiO_2$, and $LiCoO_2$ are represented in figure 3.5. The graphs are expressed in numbers of states per atom for each energy interval. They are plotted to compare the conductivity of these crystal structures.

The DOS graphs shown in figure 3.5 depict the relatively exact trend in all the structures. Conversely, the DOS is characterized by two distinguishable patterns, i.e. valence band and conduction band. More importantly, the DOS and the band structure are calculated using the same cut-off energy, K-mesh points, and U parameters.

(i) The density of States for $LiMnO_2$

Figure 3.5 (a) shows the density of states for $LiMnO_2$ structure, the valence band close to the Fermi level in DOS is occupied by a set of peaks coming from O-p states and Mn-d states. On the other hand, the conduction band is occupied by a set of peaks mainly from p state of Mn, p state of O, and s state of Li. The peaks at the Fermi level are due to the p state of O and d state of Mn contributions. The PDOS in figure 3.5 (a) exposes high electron contribution in the valence band as compared to the conduction band. In the valence band of $LiMnO_2$, the p state of O and Mn-contribution increases gradually, and the d state contribution of Mn gradually decreases. Moreover, the s state contribution of O and Li is moderate. This contribution is seen also in the transition metal where it is higher in Mn. As such the TDOS depicts moderate electron contribution in the conduction ban. The moderate electron contribution is mainly by the s and p states of O; s, p, and d of Mn and s of Li which have lower peaks.

The conduction band of $LiMnO_2$ is dominated by the exceedingly small contribution of p states in O, p states of Mn and s states of Li. There is no s states contribution in O and Mn, no p state contribution in Mn. As a result, this causes a gradual decrease in peak accumulation in the conduction band. As a result, the TDOS of $LiMnO_2$ has a bandgap of 1.64 eV indicating an insulator characteristic in the material.

(ii) The density of States for $LiNiO_2$

Figure 3.5 (b) shows the density of states for the $LiNiO_2$ structure, the E_f lies in between the peaks that are in the valence and conduction bands. The gap from the E_f to the peak in both energy regions is relatively smaller. These peaks are due to the contribution of p states of O and d states of Ni. The PDOS in figure 3.5 (b) expose high electrons contribution in the valence band as compared to the conduction band. In the valence band, the p state of O and Ni-contribution increases moderately. On the other hand, the d state contribution of Ni increases relatively. The s state contribution of O and Li in $LiNiO_2$ is higher. Furthermore, this contribution is seen also in the transition metals where it is extremely low with approximately the same amount in Ni.

In the conduction band, TDOS depicts low electron concentration in $LiNiO_2$. The low electron contribution on $LiNiO_2$ material is mainly by the s and p states of O; s, p, and d of Ni, and s of Li, which have lower peaks. Moreover, there is no s state contribution of O, and relatively small p states contribution from O and Ni. As such, there is a small

contribution from s states of Ni and Li. Hence, this causes a lowering of peaks displayed in the TDOS figure 3.5 (b). As a result, the $LiNiO_2$ has a bandgap of 0.40 eV indicating a semiconductor behaviour.

(iii) The density of States for $LiCoO_2$

In figure 3.5 (c), is the density of states for $LiCoO_2$ structure, the E_f cuts a lower part of a peak in the valence band, leaving a relatively big gap between the E_f and the first peak in the conduction band. The contributing peaks at the Fermi level are due to the contribution of s and p states of O and d states of Co. The PDOS in figure 3.5 (c) exposes high electrons contribution in the valence band as compared to the conduction band. Thus, in the valence band, the p state of O and Co-contribution is exceptionally low. On the other hand, the d state contribution of Co is moderate, and the s state contribution of O and Li in $LiNiO_2$ is lower. This contribution is also observed in the transition metals where it is extremely low with approximately the same amount in Co.

From the conduction band, TDOS depicts high electron contribution in $LiCoO_2$. The high electron contribution on the $LiCoO_2$ is mainly by the s and p states of O; s, p, and d of Co, and s of Li which have intense peaks. As such the $LiCoO_2$ has a bandgap of 2.22 eV indicating an insulator characteristic behaviour

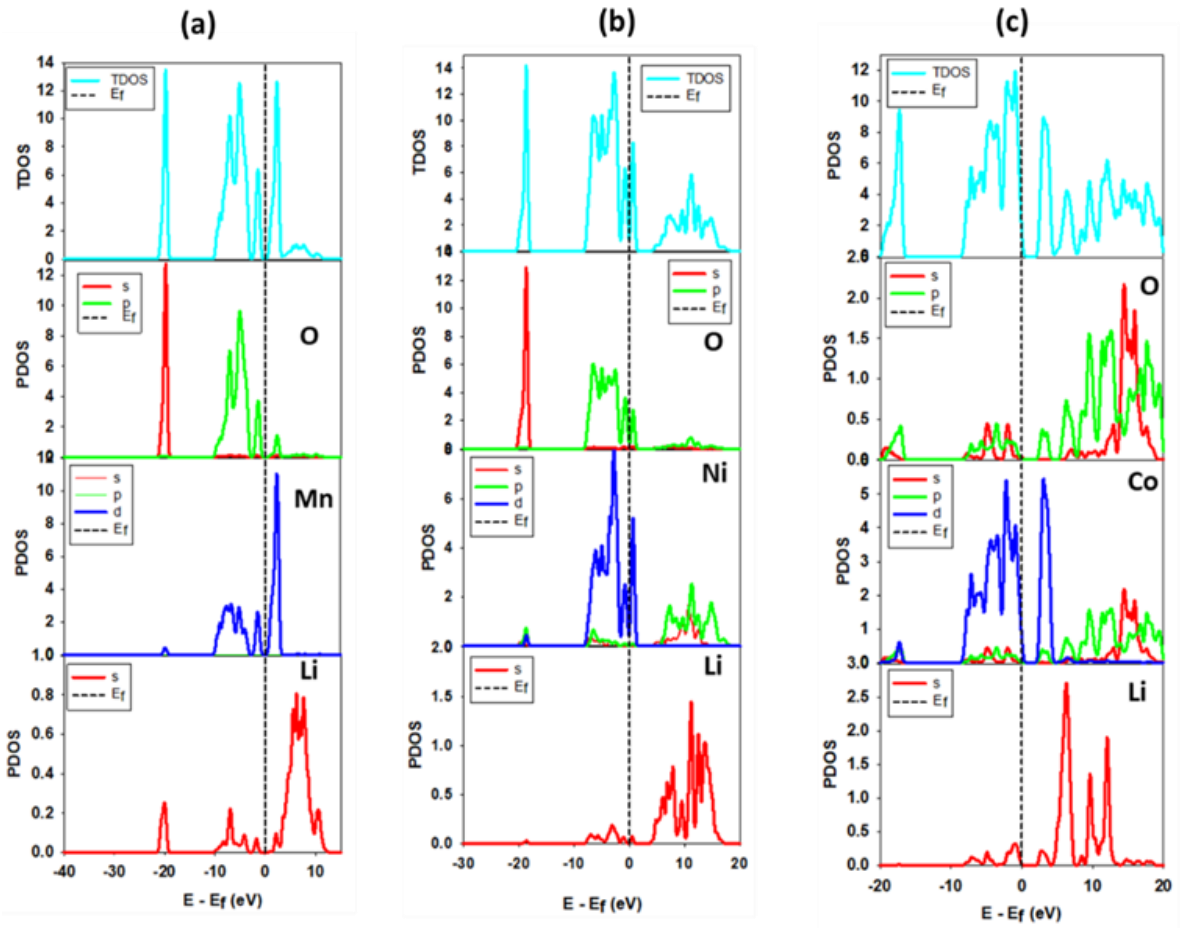

Figure 3.5 Graphical representation of the total and partial density of states for (a) $LiMnO_2$, (b) $LiNiO_2$ and (c) $LiCoO_2$.

3.4.7 Mechanical Stability

Mechanical stability of material provides a descriptive measurement of a material stiffness to withstand its structural nature under mechanical load. Mechanical stability is crucial for applications of low-density material. However, the mechanical properties of materials vary from material to material by order of magnitude with changing atomic composition and crystal structures [154]. Hence, the mechanical stability and elastic response of crystal systems are determined from properties such as elastic constants, bulk (B), shear (S), and Young's (Y) moduli. These are associated with changes that can occur on the crystal structure under excessive pressure. That is, a macroscopic distortion of a crystal structure is related to elastic constants, which are associated with structural stability, equation of state, interatomic potentials and phonon spectra [155].

(i) Phonon Dispersion Curves for $LiMnO_2$, $LiNiO_2$, and $LiCoO_2$

The phonon dispersion curves analyse in details the vibrational stability of a material. The term phonon draws an analogy between photon representing a quantum of electromagnetic radiation and quanta of lattice vibration [156]. The theory of phonons explains in details solid-state phenomena, such as thermal and electrical conductivity, which are unable to be outlined in the static lattice theory [156]. The phonon dispersion calculations in this subsection were performed to further compare in detail the structural stability of the $LiMnO_2$, $LiNiO_2$ and $LiCoO_2$ crystalline materials.

Figure 3.6 (a) is a phonon dispersion curve of $LiMnO_2$ structure at ambient pressure. The phonon dispersion curve does not have soft modes along with high symmetry directions in the Brillion zone. This behaviour suggests that $LiMnO_2$ is vibrationally stable. The phonon dispersion curve for the $LiNiO_2$ structure at ambient pressure is displayed in figure 3.6 (b). The phonon dispersion curve shows no evidence of soft modes along with the high symmetry directions in the Brillion zone. The behaviour of the curves suggests that the material is vibrationally stable.

Figure 3.6 (c) is a phonon dispersion curve for the $LiCoO_2$ structure. The phonon spectra display imaginary phonon branching down to -1THz. The phonon is observed along the high symmetry direction referred to as Z (1 ½ ½) and G (0 0 0) in the Brillion zone as discussed in chapter 2 section 2.11.3. Considering the absence of supporting evidence on the PDOS, the soft mode is regarded as imaginary. However, it is a reason that the structure is less stable than the $LiMnO_2$ and $LiNiO_2$ as proven by the density of states shown in figures 3.5. The vibrational stability of the materials is a reason for a larger energy bandgap in the material as shown in the energy band structures figure 3.4 (c).

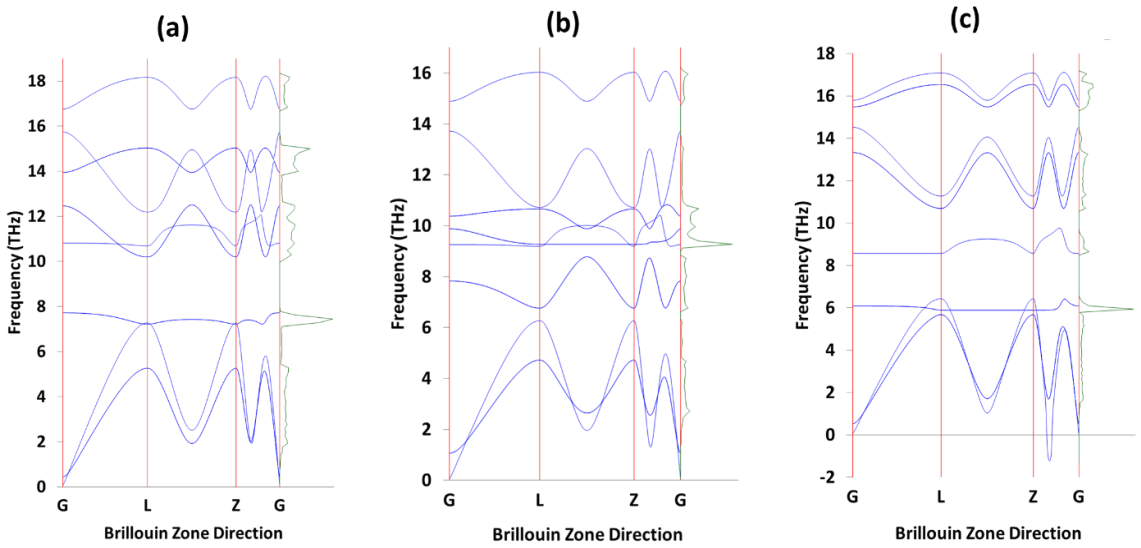

Figure 3.6 The graphic representation of phonon dispersions for (a) $LiMnO_2$, (b) $LiNiO_2$ and (c) $LiCoO_2$.

(ii) Elastic Properties

Elastic properties relate to fundamental aspects of solid-state, such as the equation of states, phonon dispersions, and thermal expansion [157, 158]. To further investigate the stability of $LiMO_2$ (M: Mn, Ni, and Co) structures, the elastic constants were calculated. These elastic constants are defined by the Taylor expansion of the total energy, and they are derived from the energy as a function of lattice strains [159]. In this section, the results of elastic constants, bulk, shear, and Young's moduli of $LiMO_2$ (M: Mn, Ni, and Co) are discussed. Studies have shown that smaller lattice parameters yield larger values of elastic constants, while larger lattice parameters yield smaller elastic constants.

On table 3.9 is the list of DFT results on elastic constants (C_{ij}), bulk (B), and Young's (E) moduli for $R\bar{3}m$ $LiMnO_2$ first column. All the independent elastic constants for the orthorhombic $LiMnO_2$ structure are positive and satisfy the stability conditions for mechanical stability. Moreover, there is a dependent elastic constant C'= (C_{11}-C_{12})/2 which also contributes to the stability of a material. This independent parameter confirms the stability of a particular material when it has a positive value (C'>0) [113]. Hence, the calculated C' for $LiMnO_2$ yields a value greater than 0, suggesting that the materials are stable. The elastic constant C_{66} for $LiMnO_2$ have the same values as the C'. This phenomenon suggests that the C_{66} on the structure is a dependent elastic constant. Moreover, from the calculated elastic constants, the macroscopic

mechanical parameters such as bulk, shear and Shear modulus have been calculated. The parameters show larger values of bulk and Young moduli on the $LiMnO_2$ structure, suggesting hardness and stiffness, respectively. That is, the bulk moduli value (145.91 GPa) suggests that the material is resistant to compression and Young's modulus (218.85 GPa) indicating that the material is not subjective to length elongation. Lastly the law value of shear modulus (87.54 GPa) suggesting that the material is subjected to deformation. Moreover, the experimental elastic constants shown in table 3.9 also display the same behaviour as the simulated elastic constants with a difference of 1.76%. The difference is relatively small, implying a fair agreement between the simulated and the experimental value.

Table 3.9 lists DFT results on elastic constants (C_{ij}), bulk (B), and Young's (E) moduli for $R\bar{3}m$ $LiMnO_2$, $LiNiO_2$, and $LiCoO_2$. All the independent elastic constants for the orthorhombic $LiNiO_2$ structure are positive and satisfy the stability conditions for mechanical stability. Moreover, the calculated C' for $LiNiO_2$ yields a value greater than zero, providing more evidence that the materials are stable. The elastic constant C_{66} for $LiNiO_2$ has the same values as the C'. This phenomenon suggests that the C_{66} on the structure is a dependent elastic constant. Moreover, from the calculated elastic constants, the macroscopic mechanical parameters such as bulk, shear and Shear modulus have been calculated. The parameters show larger values of bulk and Young moduli on the $LiMnO_2$ structure, suggesting hardness and stiffness, respectively. That is, the bulk moduli value (132.38 GPa) suggests that the material is resistant to compression and Young's modulus (122.25 GPa) suggesting that the material is not subjective to length elongation. Lastly the law value of shear modulus (45.41 GPa) suggesting that the material is subjected to deformation. The experimental elastic constants shown in table 3.9 also display the same behaviour as the simulated elastic

constants with a difference of 5.11%. The difference is relatively small, implying a fair agreement between the simulated and the experimental value.

Table 3.9 the comparisons of elastic constants (C_{ij}), bulk (B), and Young's (E) moduli of $LiMnO_2$, $LiNiO_2$, and $LiCoO_2$ with the experimental values.

Elastic Constants C_{ij} (GPa)	Calculated			Experimental		
	$LiMnO_2$	$LiNiO_2$	$LiCoO_2$	$LiMnO_2$ [160]	$LiCoO_2$ [160]	$LiCoO_2$ [161]
C_{11}	315.33	212.59	347.00	201	167	-
C_{12}	88.85	153.18	98.36	104	93	-
C_{13}	67.31	65.66	64.80	78	48	-
C_{22}	315.33	212.59	347.00	201	169	-
C_{23}	67.31	56.66	64.80	78	77	-
C_{33}	235.60	197.26	221.50	148	238	-
C_{44}	55.10	42.35	52.32	92	43	-
C_{55}	55.10	42.35	52.32	92	48	-
C_{66}	113.24	29.70	124.32	90	84	-
$C'=(C_{11}-C_{12})/2$	113.24	29.71	124.32	-	-	-
Bulk (B)	145.91	132.38	152.38	112.71	112.25	191
Shear (G)	87.54	45.41	91.63	65.75	28.46	80
Young's (E)	218.85	122.25	228.99	165.14	78.72	-

In table 3.9 the last column are DFT results on elastic constants (C_{ij}), bulk (B), and Young's (E) moduli for $R\bar{3}m$ $LiCoO_2$. All the independent elastic constants for the orthorhombic $LiMnO_2$ structure are positive and satisfy the stability conditions for mechanical stability. Moreover, the calculated C' for $LiCoO_2$ yields a value greater than

0, suggesting that the materials are stable. The elastic constant C_{66} for $LiCoO_2$ have the same values as the C'. This phenomenon suggests that the C_{66} on the structure is a dependent elastic constant. Furthermore, from the calculated elastic constants, the macroscopic mechanical parameters such as bulk, shear and Shear modulus have been calculated. The parameters show larger values of bulk and Young moduli on the $LiCoO_2$ structure, suggesting hardness and stiffness, respectively. That is, the bulk moduli value (152.38 GPa) suggests that the material is resistant to compression and Young's modulus (228.99 GPa) suggesting that the material is not subjective to length elongation. Lastly the law value of shear modulus (91.63 GPa) suggesting that the material is subjected to deformation. The experimental elastic constants for the $LiCoO_2$ were missing from the literature for comparisons.

(iii) Total Density of States

To investigate the stability of these materials in more detail, the TDOS is evaluated as shown in figure 3.7. The structure with the highest density of states at E_f is considered the least stable, whereas the structure with the lowest density of states at E_f is considered the most stable [162]. It was inferred that the $LiMnO_2$ represented by a red line in the plot has the lowest density of states as compared to $LiNiO_2$ which has the second-lowest density of states; the $LiCoO_2$ with the highest density of states at E_f. As a result, the $LiNiO_2$ is the most stable relative to $LiMnO_2$ and $LiCoO_2$.

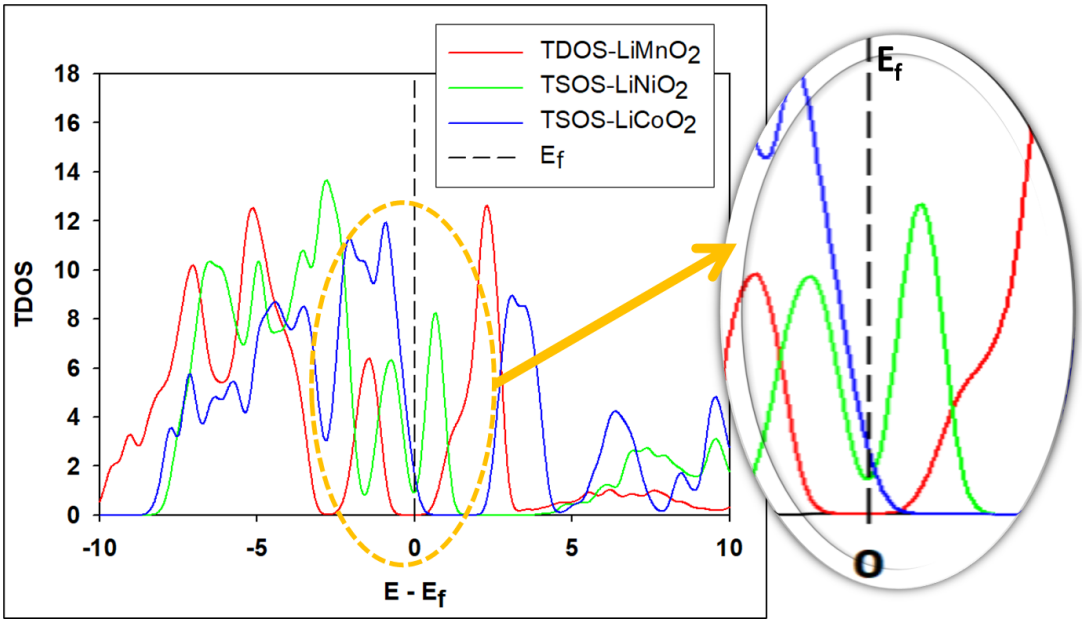

Figure 3.7 The comparisons of the total density of states.

3.5 Discussion

The work was probing the crystal nature of the $LiMO_2$ (M: Mn, Ni, and Co), the electronic calculations reveal the conductivity and the electron contribution in the conductivity behaviour of the materials. Furthermore, the materials vibrational stability was determined to provide the mechanical properties of the materials. The first principle calculation of the orthorhombic $R\bar{3}m$ space grouped $LiMO_2$ (M: Mn, Ni, and Co) was performed to determine the electronic band structure, density of states and phonon dispersions. All the calculations were performed using the Perdew-Burke-Ernzerhof (PBE) exchange-correlation function with Hubbard U-parameter to correct the correlated d electrons of the transition metals (Mn, Ni, and Co).

The band structures provided evidence that the $LiNiO_2$ has a semiconductor behaviour characteristic with high electrical conductivity, due to its exceedingly small energy gap. On the other hand, both $LiMnO_2$ and $LiCoO_2$ have an insulator behaviour characteristic with low electrical conductivity. Comparatively, the $LiNiO_2$ has the smallest bandgap amongst all the materials. On contrary, the $LiCoO_2$ has the largest bandgap compared to all materials. This phenomenon is confirmed by the density of states curves. The conduction bands of $LiMnO_2$, $LiNiO_2$, and $LiCoO_2$ materials are dominated by the contribution of p states in O, p states of transition metals (Ni, and Co) and s states of Li. There is no s states contribution in O and Mn, no p state contribution in Mn. As a result, this causes a gradual decrease in peak accumulation in the conduction band. The decrease in the s- and p-electrons number with increasing of electrons from oxygen ions to the transition metals d shell, corresponds to a $d^n \rightarrow d^{n+1}L$ transition or 2p →3d transition, it is a transition with charge transfer [163]. The partial density of states shows that the states associated with the transition metals are predominantly of 3d character while the states associated with O are predominantly of 2p character. Furthermore, the 3d states of transition metals are predominant with little contribution from O and Li s-orbital in all structures.

Relating to the bonding and non-bonding states, the occupied d bonding states are separated from the unoccupied antibonding states of the transition metals (Mn, Ni, and Co) by the Fermi level; this occurs as a result of the interaction of the transition metals (Mn, Ni, and Ni) with the O-p states which result in splitting the transition metals-3d states into valence and conduction bands [164]. In the conduction band, the transition metals-3d states are shifted to higher energy and they remain unoccupied, whereas

in the valence band the transition metals-3d states are shifted to a lower energy region. This allows for a gap at the Fermi level to be generated [164]. Hence, the overall band gaps for all materials are found to be considered in more fair agreement with the experimental results than the theoretical results [152, 153, 164, 150]. Hence the agreement between our results and the experimental results is satisfactory [152, 153, 164].

Considering the structural stability, all the independent elastic constants for the orthorhombic structures are positive and satisfy the conditions for mechanical stability. Moreover, the C' for $LiMnO_2$, $LiNiO_2$ and $LiCoO_2$ suggests that the materials are stable with C'>0 for all materials. The elastic constant C_{66} for $LiMnO_2$, $LiNiO_2$ and $LiCoO_2$ have the same values as the C'. This phenomenon suggests that the C_{66} on the structures is a dependent elastic constant. On the other hand, the larger values of bulk and Young moduli on all the three structures, suggests hardness and stiffness, respectively in all the materials.

Phonon dispersion curves outlined that the $LiCoO_2$ is the least stable material as compared to the other materials due to the imaginary negative frequencies contained in the phonon curves of this material. This situation is supported by the large bandgap size of the materials determined in the band structures. More evidently, the heats of formation declare $LiNiO_2$ as a thermodynamically stable material due to its lowest value. The energy of the position empty transition metals e_g, which mainly determines the band gaps strongly depends on the methods employed during the investigation. This is validated more by the compared total density of states for these materials; from which the $LiCoO_2$ presented the highest density of states at the Fermi level indicating that the material is comparatively the least stable. On the other hand, $LiNiO_2$ had the lowest density of state at the Fermi level implying that it is more stable than $LiMnO_2$ and $LiCoO_2$. These total densities of states support the findings from both band structures and the phonon dispersion curves. The material with the lowest band gap has a lower density of states at the Fermi level and hence it is more stable. Conversely, the material with a big band gap possesses the highest density of states and as a result, it is the least stable material. On the other hand, the three structures satisfy the stability criteria of the orthorhombic material, proving their stability.

Chapter 4: Derivation and Validation of Interatomic Potentials for NiO and CoO

In this section, the GULP derived interatomic potentials for NiO and CoO cubic crystals and their validation are discussed. The derived interactions between Ni-O, Ni-Ni, Co-O and Co-Co pairs were used as input parameters for the thermodynamic properties of both the of NiO and CoO systems, each containing 20 000 atoms. The lattice parameters, elastic constants, energy graphs, melting points and radial distribution curves were employed to analyse properties of these systems compared with experimental results.

4.1 Introduction

The molecular dynamic (MD) simulations require that the interatomic interactions (forces between atoms within a structure) are utilized at each step of performing a calculation particularly fitting interatomic potential. The nature of the interatomic bonding and atomic configuration is required before the calculations [165]. As such the description of the interatomic potential in this work is based on atomistic technique. This technique employs empirically derived equations to describe the interatomic interactions. Atomistic simulation technique makes it is possible to simulate large systems with thousands of atoms. As such the method is ideal for producing accurate statistical data from molecular dynamics simulations to allow efficient use of large simulation cells and long simulation time. Moreover, the accuracy and reliability of the generated force fields rely on the quality of the interatomic potentials [166]. As such, fit the interatomic interactions using corresponding oxides to improve the transferability and accuracy of our force fields.

In general, oxides possess complex crystal structures on which theories of thermal conductivity have been based, resulting in hindering the applications of the theories to various oxides [165]. This limits the understanding of the origin of the modest thermal conductivity [165]. In counter to that, we derive the potential parameter sets that describe atomic interactions in NiO and CoO crystal structures, particularly for utilization in MD calculations at high temperature to analyse if the dynamic motion of atoms is realistic in terms of the state transformation of the structures.

4.2 Procedure

The accuracy and reliability of the atomic simulations depend mainly on the quality of the derived interatomic potentials [167]. In this work, a simple two-body potential function based on the Born model of ionic solids was used. Although in most molecular dynamic simulations, the shell model used to approximate electronic polarization effects was not incorporated due to the significant increase in computational time; in this work, all particles were assumed to be rigid ions.

The derivation of interatomic potentials was carried out using a cross-platform, streaming task runner (code-based) GULP [168]. The code first performs the optical optimisation to minimise the energy of the structure under a temperature of 300K (considered as room temperature), thereafter performs the parameter fitting. The input parameters such as lattice parameters, elastic constants, space group number, dielectric constant and bulk modulus are provided from the experimental data before the fitting. The procedure fits the ionic size (A_{ij}), dispersion parameter (C_{ij}), and the hardness of ions (ρ_{ij}), according to the Buckingham potentials, where the interaction of two atoms are not directly bonded as a function of the interatomic distances. The atomic probing was based on Co^{3+}-O^{2-}, Co^{3+}- Co^{3+}, Ni^{3+}-O^{2-}, Ni^{3+}-Ni^{3+} and O^{2-}- O^{2-}.

Moreover, the resultant interatomic interactions are utilised as input data on the molecular dynamic (MD) simulation for validation. The MD calculations are performed on 20000 atomic crystal structures of NiO and CoO. The calculations are performed under temperature variations to point to the melting temperature of each material, under the amorphization technique. The process uses the micro-canonical ensemble (NVE), which fixed the total number of atoms, volume, and energy of material under investigation, however, permits the temperature to change.

4.3 Structural Properties of NiO and CoO

In figure 4.1 below, are the depictions of primitive unit cells for the body-centred cubic (BCC) crystal structures used for fitting interatomic potentials for both compounds NiO and CoO. The BCC unit cell consists of a net total of two atoms (Ni and O or Co and O), the one in the centre (O) and eight from the corners (Ni/Co). That is, each of the corner atoms is the corner of another cube, the corner atoms in each unit cell will be shared among eight-unit cells. Moreover, the volume of each atom occupying the corner is shared between eight adjacent cells, as such the BCC structure has the

equivalent volume of two atoms, at the central midpoint and the corner. Structures used in this work have the space group of Fm3M (225) with lattice parameter a=4.42 Å [169] and a=4.26 Å [169] for NiO and CoO, respectively. The structural equilibrium interatomic distances are provided through the lattice constants and the curvature around the equilibrium bond lengths is represented by the elastic constants. Moreover, the resistance measure of compression for the structures is represented by bulk moduli. These properties are shown in table 4.1 for NiO structure and table 4.2 for CoO structure.

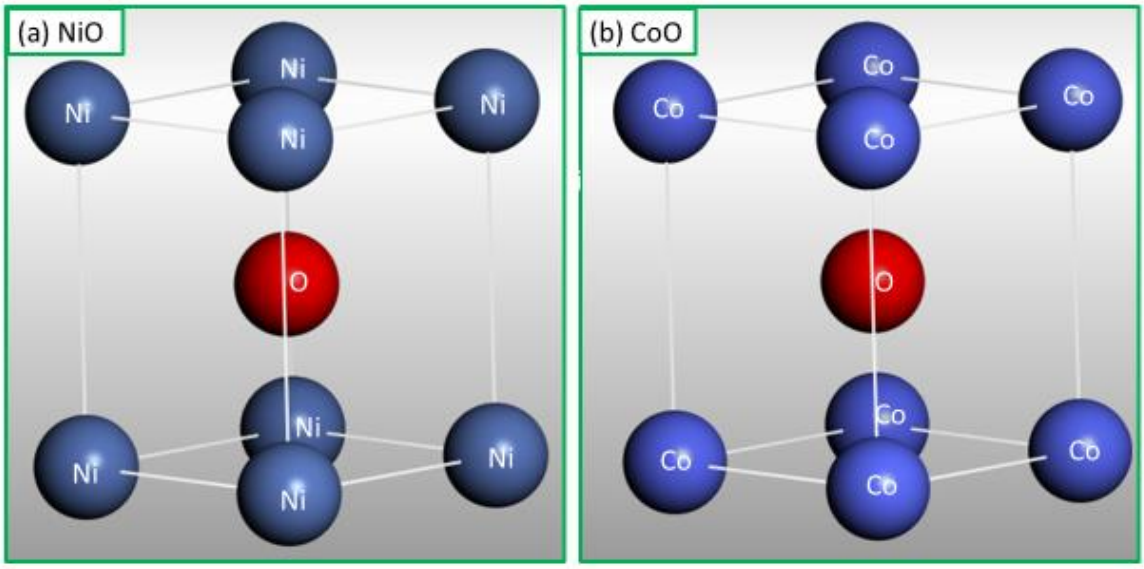

Figure 4.1 Body-cantered cubic unit cells of (a) NiO and (b) CoO.

Table 4.1 Structural properties of NiO

Structure	Lattice Parameters (Å)	Angles (°)		Elastic (GPa)	Constants	ume ($Å^3$)	Bulk Modulus (GPa)
NiO	A=4.415 [170]	Alpha	90.0	C_{11}	342.7 [171]	77.309	204.4
		Betta	90.0	C_{12}	141.3 [171]	[170]	[171]
		gamma	90.0	C_{14}	41.2 [171]		

Table 4.2 Structural properties of CoO.

Structure	Lattice Parameters (Å)	Angles (°)		Elastic Constants (GPa)		Volume ($Å^3$)	Bulk Modulus (GPa)
CoO	A=4.260 [172]	Alpha	90.0	C_{11}	307 [173]	77.309 [172]	224 [173]
		Betta	90.0	C_{12}	183 [173]		
		gamma	90.0	C_{14}	90 [173]		

4.4 Derivation of Interatomic Potentials

4.4.1 Introduction

In this section, the Buckingham interatomic potentials [174] of NiO and CoO are derived, where the interaction between two atoms that are not directly bonded as a function of the interatomic distances. The Buckingham-type potential function was employed for short-range interactions and the GULP (General Utility Lattice Package) code [175] was used to calculate the two-body interactions in each structure. To obtain appropriate potential parameters for both NiO and CoO, lattice parameters of the most stable structure, space group, and the elastic constants were used in the fitting procedure as inputs for the derivation of the potential model. The derived interatomic potentials were validated by comparison of the initial and ultimate results of the structures. Moreover, the molecular dynamics (MD) calculations based on the derived potentials were performed employing the DL_POLY [176] code to investigate the potentials accuracy at various temperatures and to determine the structural melting point.

4.5 Results

The O^{-2} - O^{-2} interactions are the dominant interactions in oxides, and the transferability of these interactions was considered vital by taking the actual interactions from the MD INPUT [165]. Hence, the short-range potentials parameters for Ni^{2+} - Ni^{2+}, Ni^{2+} - O^{2-}, Co^{2+} - O^{2-} and Co^{2+} - Co^{2+} pairs were derived. The derived Buckingham interatomic potentials are shown in table 4.3 and table 4.4 for NiO and CoO respectively. The calculated charges to maintain a neutrally charged system during fitting are shown in table 4.5. Lastly, the calculated elastic constants and bulk moduli

of the NiO and CoO structures with the generated interatomic interactions are illustrated in table 4.6 and 4.7 respectively.

Table 4.3 The derived Buckingham interatomic potentials for NiO

Ionic pair (ij)	A_{ij}(eV)	ρ_{ij} (Å)	C_{ij} (eV/ Å^6)
Ni^{2+} - Ni^{2+}	6393.86	0.27829	0.00
O^{2-}- O^{2-}	11782.88	0.23400	30.22
Ni^{2+} - O^{2-}	380400.00	0.15000	0.00

Table 4.4 The derived Buckingham interatomic potentials for CoO

Ionic pair (ij)	A_{ij}(eV)	ρ_{ij} (Å)	C_{ij} (eV/ Å^6)
Co^{2+} - Co^{2+}	80948.00	0.20000	10.00
O^{2-}- O^{2-}	11782.88	0.23400	30.22
Co^{2+} - O^{2-}	58856.82	0.18	0.00

Table 4.5 The partial charges used in deriving the interatomic potentials.

Species (ion)	Partial charge (e)	System
Nickel (Ni^{2+})	1.00	NiO
Cobalt (Co^{2+})	1.00	CoO
Oxygen (O^{2-})	-1.00	All

Table 4.6 The calculated elastic properties and bulk modulus NiO.

Elastic properties	GULP (Fitted) (GPa)	Experimental (GPa) [177]
C_{11}	344.65	342.7
C_{12}	86.60	141.3
C_{44}	86.60	41.2
Bulk modulus	172.62	204.4

Table 4.7 The calculated elastic properties and bulk modulus for CoO.

Elastic properties	GULP (Fitted) (GPa)	Experimental (GPa) [177]
C_{11}	275.27	307
C_{12}	188.26	183
C_{44}	188.26	90
Bulk modulus	217.26	224

4.6 Validation of the Interatomic Potentials

4.6.1 Comparison Between Calculated and Experimental Results

The accuracy of the derived interatomic potentials was first checked by comparing the experimental and calculated lattice parameters, volume and structural angles as illustrated in table 4.8 for NiO and table 4.9 for CoO. This confirmed the value of A_{ij} and ρ_{ij} for O^{2-}- O^{2-}, Ni^{2+} - Ni^{2+}, Co^{2+} - Co^{2+}, Ni^{2+} - O^{-2}, and Co^{2+} - O^{2-}. The comparison of the initial (experimental) and the final (fitted) elastic constants for NiO and CoO are represented in tables 4.10 and 4.11 respectively. The lattice parameters and structural angles obtained from the GULP are the same as the experimental parameters. However, there is a small difference between the experimental and the calculated volume.

Table 4.8 Comparison of initial and final parameters generated from the derived interatomic potentials in NiO.

Parameter	Exp [170]	Fitted	Difference	%Difference
Volume (Å^3)	86.06	86.06	0.00	0.00
A (Å)	4.42	4.42	0.00	0.00
B (Å)	4.42	4.42	0.00	0.00
C (Å)	4.42	4.42	0.00	0.00
Alpha (°)	90.00	90.00	0.00	0.00
Beta (°)	90.00	90.00	0.00	0.00
Gamma (°)	90.00	90.00	0.00	0.00

Table 4.9 Comparison of initial and final parameters generated from the derived interatomic potentials in CoO.

Parameter	Exp [172]	Fitted	Difference	%Difference
Volume (Å^3)	77.31	100.57	23.26	26.15
A (Å)	4.26	4.65	0.39	8.76
B (Å)	4.26	4.65	0.39	8.76
C (Å)	4.26	4.65	0.39	8.76
Alpha (°)	90.00	90.00	0.00	0.00
Beta (°)	90.00	90.00	0.00	0.00
Gamma (°)	90.00	90.00	0.00	0.00

Table 4.10 Comparison of experimental and derive elastic constants and bulk modulus for NiO.

Elastic properties	GULP (Fitted) (GPa)	Experimental (GPa) [177]
C_{11}	344.65	342.7
C_{12}	86.60	141.3
C_{44}	86.60	41.2
Bulk modulus	172.62	204.4

Table 4.11 Comparison of experimental and derive elastic constants and bulk modulus for CoO.

Elastic properties	GULP (Fitted) (GPa)	Experimental (GPa) [177]
C_{11}	275.27	307
C_{12}	188.26	183
C_{44}	188.26	90
Bulk modulus	217.26	224

4.7 MD Study of NiO and CoO Using the Derived Potentials

The derived interatomic potentials were fit into the input file of the molecular dynamics to determine the melting point of 20 000 atoms nanostructure of both NiO and CoO. Figures 4.2 and 4.3 are the representation NiO and CoO (respectively) of the structures generated from MD with the interatomic potentials.

4.7.1 NiO Bulk Structure

The NiO bulk was evaluated under the NVE ensemble, with 5000 steps, and 0.001 ns. The NiO with generated interatomic potentials remains in a crystalline form from the temperature of 0K-2000K, figure 4.2 (a). The structure changes from the crystalline form into an amorphous state, when heated with a temperature between 2250K and 2500K figure 4.2 (a and b). The actual melting point of the structure is determined from the curve of energy vs temperature shown in figure 4.3. The graph shows a point where the state change starts to take place that is the transformation from the crystalline to amorphous form starts at 2150K. This temperature is relatively close to the experimental melting point (2228K) of the NiO structure as shown in table 4.12 below [178].

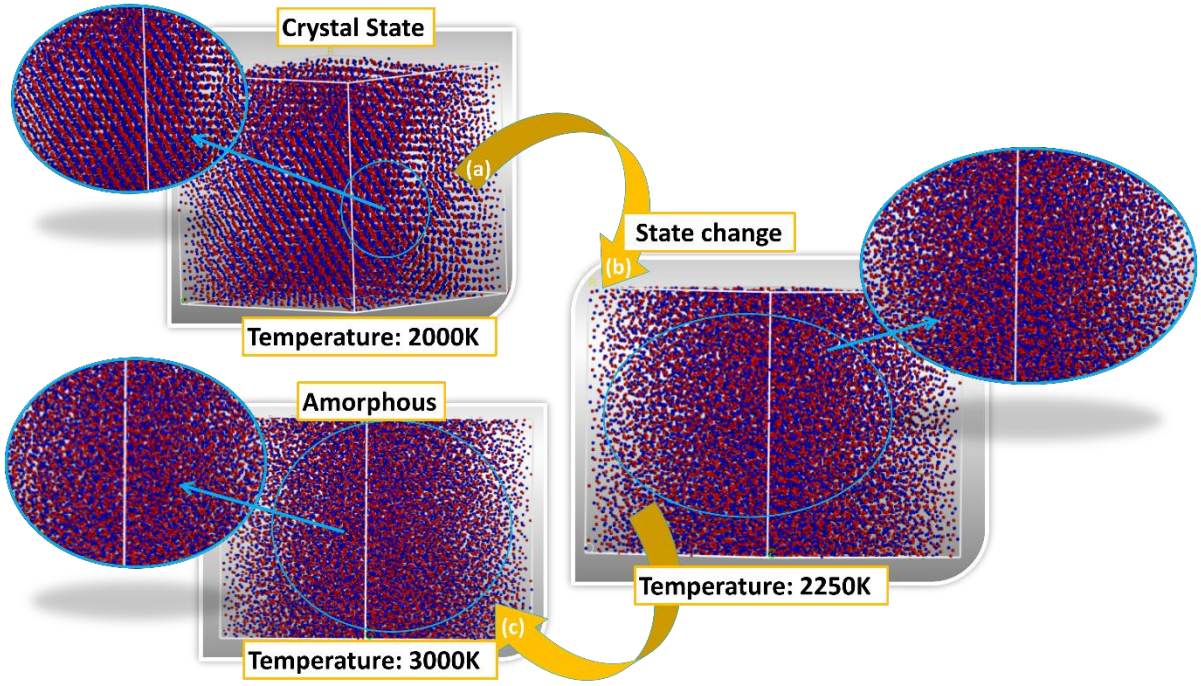

Figure 4.2 Representation of molecular dynamics results with the derived interatomic potentials in different temperatures. (a) NiO structure with 20 000 atoms in a crystalline form (before the melting point), (b) the structure at the melting temperature, and (c) the amorphous structures (after melting point)

Table 4.12 Comparisons of the melting temperatures for NiO structure.

Structure	Calculated Melting Temperature (K)	Structure melting Temperature (K) [178]
NiO	2250	2228

In figure 4.3 is the graph representing the relationship between energy and temperature in the NiO structure. The graph shows the structure has constant energy when heated between 2000K and 2100K. However, the energy of the structure increases at 2100K. This implies the elevation in the energy level of atoms above an arbitrary baseline energy state. At this level, the energy of a structure remains constant under the temperature range of 2150K to 2350K. Within this range, the experimental structure transforms from the crystalline to the amorphous state. At 2250K, the structure changes state. This point is regarded as a melting temperature.

The simulated melting temperature is relatively close to the experimental value of 2228K [178]. Moreover, the graph depicts another increase in energy of the structure which leads to the breaking point of the structure. That is the crystal breaks beyond 2350K. The structural break can lead to huge forecasting errors and unreliability of the model in general [179].

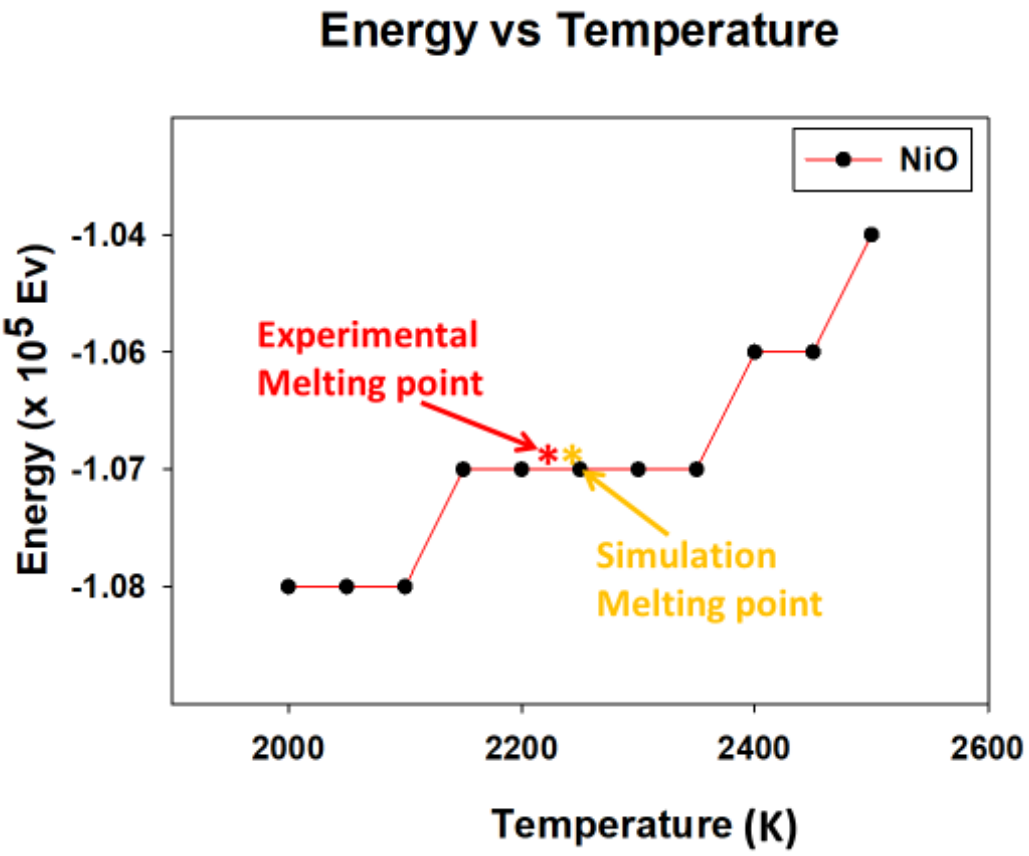

Figure 4.3 Energy vs temperature plot for NiO structure.

4.7.2 CoO Bulk Structure

The CoO bulk was evaluated under the NVE ensemble, with 5.0 Pa, 5000 steps, and 0.001 ns. Figure 4.4 is an illustration of structures generated with interatomic potentials for CoO. The MD results show that the structure remains in the crystalline form when heated between 0K to 1000K shown in figure 4.4 (a). The transition from crystalline to amorphous state is present from 1100K to 2000K illustrated in figures 4.4 (a, b and c). The actual melting point of the structure was determined from the energy vs temperature curve as shown in figure 4.5. The plot outlines the 1100K as the temperature at which a complete transformation from a crystalline state to an amorphous occurs. This is shown by the constant energy from the 1100K towards the

2000K. The validation of the melting point temperature for the CoO structure is shown in table 4.13.

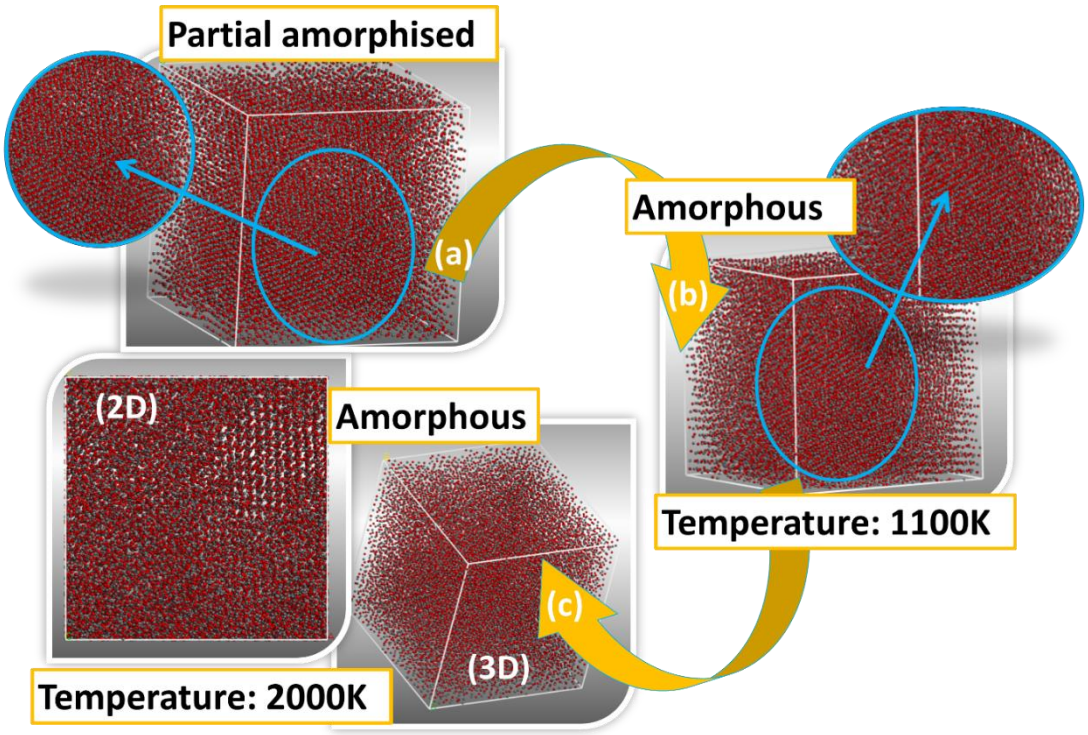

Figure 4.4 Representation of molecular dynamics results when run with the derived interatomic potentials in different temperatures. (a-c) CoO structure with 20 000 atoms at different temperatures. (a) The CoO structure with signs of state change (melting), (b) CoO structures in an amorphized state, and (c) the amorphous structures (after melting point).

Table 4.13 Comparisons of the melting temperatures for CoO structure.

Structure	Calculated Melting Temperature (K)	Structure melting Temperature (K) [178]
CoO	2000	2206

In figure 4.5 is the graph representing the relationship between energy and temperature in the CoO structure. The graph depicts a directly proportional relationship between energy and temperature at 300K and 600K, and also at 900K to

1400K. This implies the elevation in the energy level of atoms within the structure above an arbitrary baseline energy state. From 1400K, the energy of a structure remains constant. Within this range, the structure transforms from the crystalline to the amorphous state. At 1800K the structure starts to change state, however, the complete change of state is realised at 2000K. This point is regarded as the melting temperature. The simulated melting temperature is relatively close to the experimental value of 2206K [178].

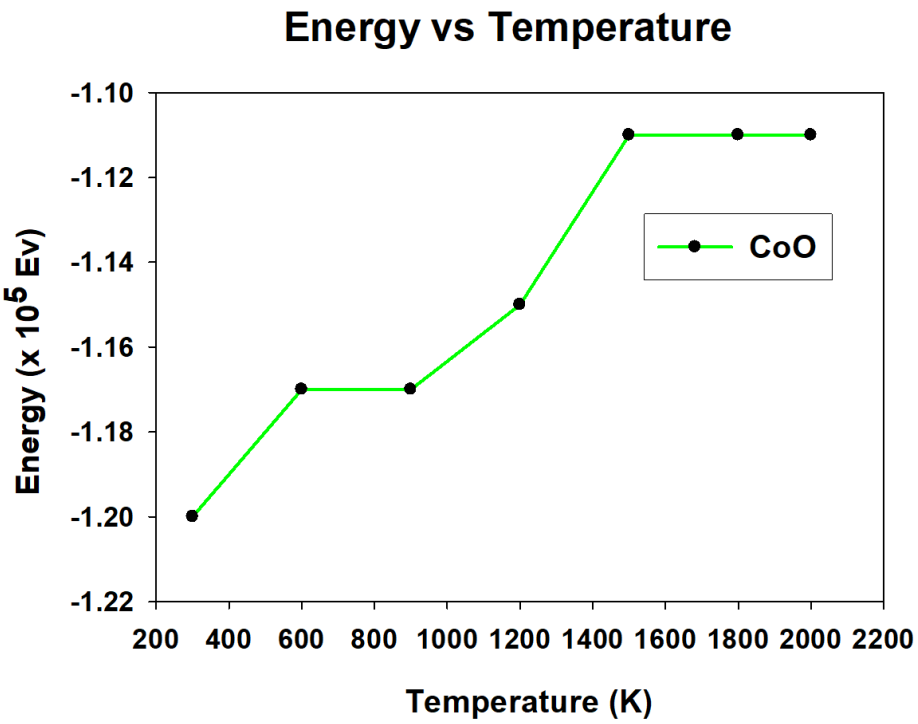

Figure 4.5 Energy vs temperature plots for CoO structure

4.8 Radial Distribution Function

The radial distribution function (RDF) defines the probability of finding a particle at a distance r from another particle. Moreover, the RDF describes how the density of surrounding matter varies as a function of the distance from a point. The RDF is strongly dependent on the type of matter under study; hence they vary greatly for solids, gases, and liquids. To demonstrate a phase change in NiO and CoO structures, the RDFs of amorphous and crystalline structures were calculated to represent bond lengths between relative atom species within the bulk material shown in figures 4.6 to 4.9, respectively.

4.8.1 NiO Structure

The RDFs for the NiO structure shown in figure 4.6, indicate that as the temperature increases, the peaks become broader, and the countable number of the peaks reduces for Ni-Ni, O-O and Ni-O interactions. The Ni-O were determined to have a bond length of 1.9 Å. The first maximum peak for Ni-Ni interaction is at ~ 2.2 Å, O-O and Ni-O is approximately 3.5 Å. The peaks beyond 3 Å for the structure at 2250K are relatively broader than that of the structure at 2000K. This suggests that the probability of finding the nearest neighbouring atom in NiO at 2250K is exceptionally low, and it is relatively high in the 2000K temperature. That is, the structure heated at 2000K has not changed its form, it is still in the crystalline form as shown by the snapshot of the bulk material in (b) with the atomic patterns; whereas the structure heated up to 2250K has changed to the amorphous state represented in (d).

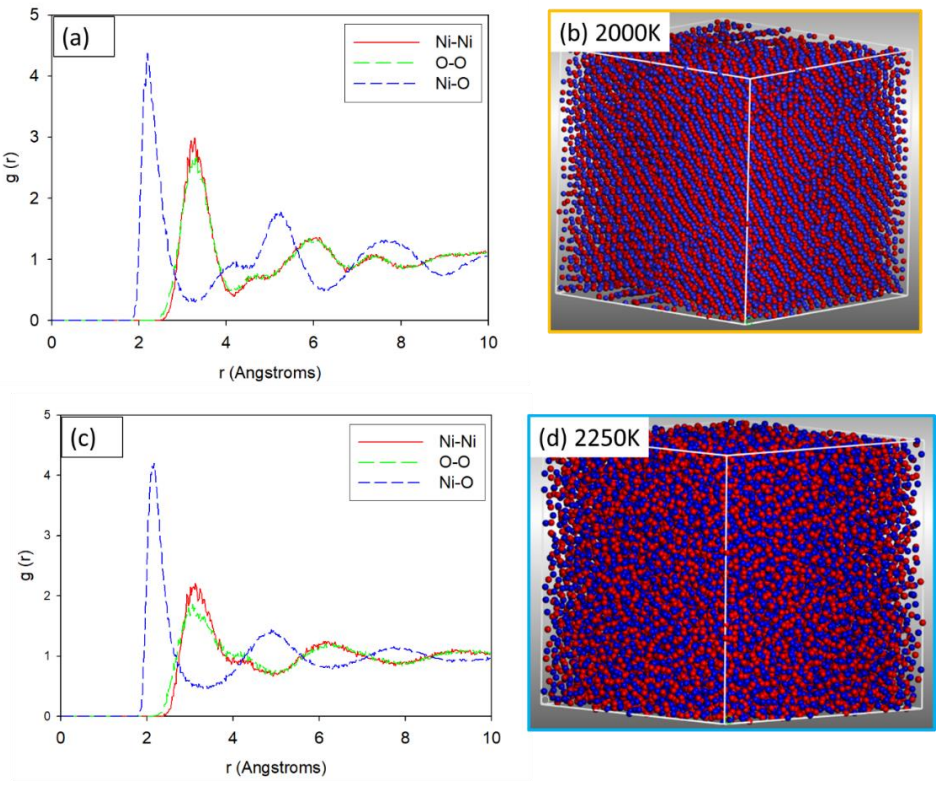

Figure 4.6 representation of the radial distribution curves for NiO in the crystalline state (a) and the snapshot of the bulk structure (b), the redial distribution function curves for NiO in amorphous forms and (d) its bulk structure.

To further probe the behaviour of the material under different temperatures, the radial distribution functions were calculated for the material at various temperatures. The

RDF curves are shown in figure 4.7 below. The magnified portion of the curves shows the broadening of the curves as the temperature increases. It is observed that from 300K to 1200K the peaks are sharper, suggesting that the atoms within the material area more ordered implying that the material is in the crystalline state. However, the peaks broaden from 1500K indicating the state change in the material. The peaks broaden even more when the temperature increases, suggesting that the material turns into an amorphous phase. The RDF show evidence of an amorphous phase at the experimental melting point [178].

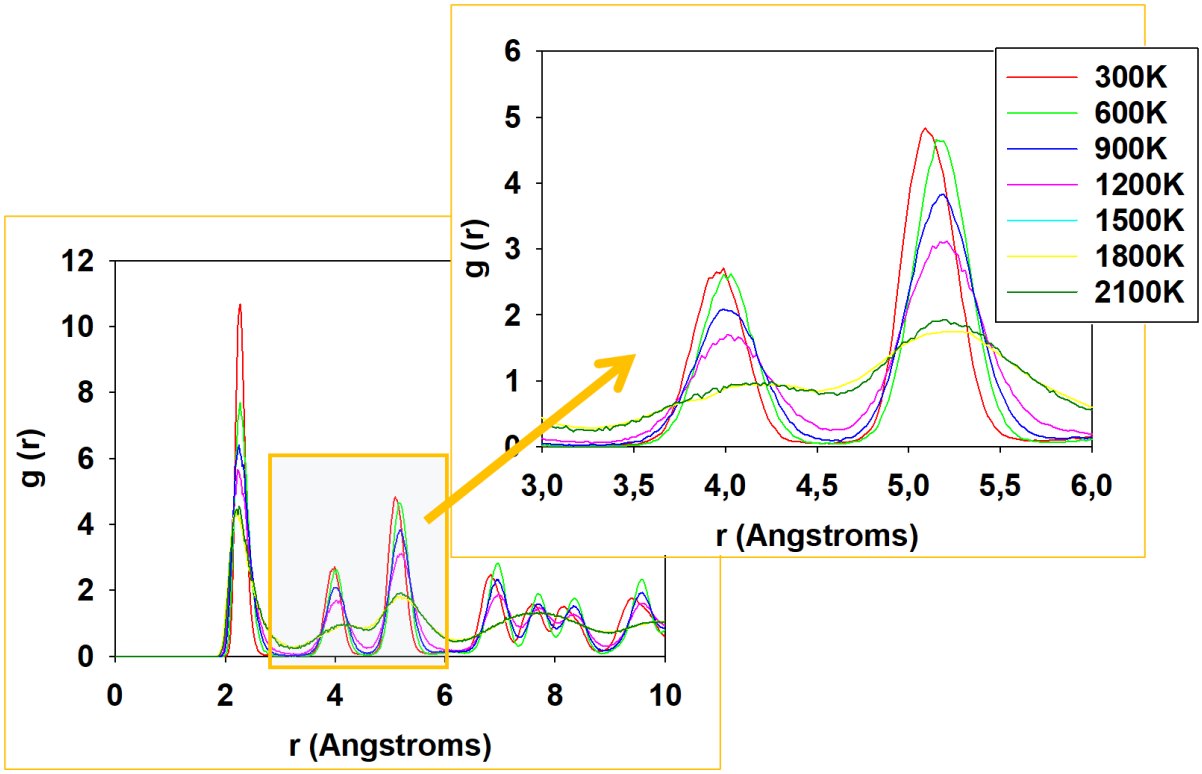

Figure 4.7 The radial distribution function curves for NiO under different temperatures; and the magnified portion on the top right corner.

4.8.2 CoO Structure

On figure 4.8 is the RDFs for CoO structure; from the plot, we observe that the increase in the simulation temperature results in the broadened peaks for Co-Co, O-O and Co-O atomic interactions and the decreased number of the peaks. The Co ions lie in positions having *m* symmetry with a mean of Co-O bond length of 2.10 Å, falling within a range of experimental bond length of the same elements [180]. The first maximum peak for Co-O interaction is at approximately 2.2 Å for O-O interaction and at approximately 3.5 Å for Ni-Ni interaction. The peaks beyond 2.2 Å for a structure

heated at 1500K are relatively more intense with a higher probability of finding the nearest neighbouring atom in CoO. This indicates that the structure is in the crystalline form as depicted in (b). However, the structure heated at 2000K has broader peaks beyond 2 Å with a lower probability of finding the nearest neighbouring atom in the structure. This suggests that the structure has changed its form into amorphous as shown by the snapshot of the material bulk in (d).

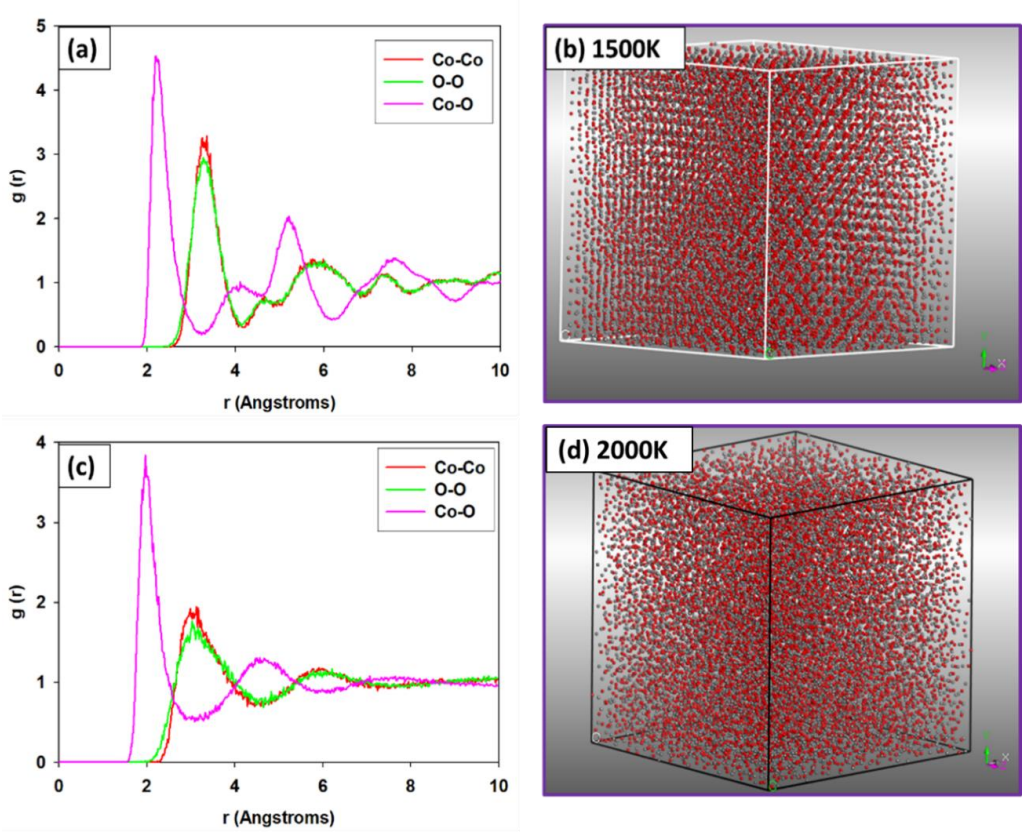

Figure 4.8 representation of the radial distribution curves for CoO in the crystalline state (a) and the snapshot of the bulk structure (b), the redial distribution function curves for CoO in amorphous forms and (d) its bulk structure.

To further investigate the behaviour of the material under different temperatures, the radial distribution functions were calculated for the material at various temperatures. The RDF curves are shown in figure 4.9 below. The zoomed portion of the curves shows the broadening of the curves as the temperature increases. It is observed that from 300K to 1500K the peaks are more intense, suggesting that the atoms within the material area more ordered implying that the material is in the crystalline state. However, the peaks broaden from 1800K indicating the state change in the material.

The peaks broaden even more when the temperature increases to 2000K, suggesting that the material turns into an amorphous phase. The RDF show evidence of an amorphous phase at the temperature close to the experimental melting point (2206K) [178].

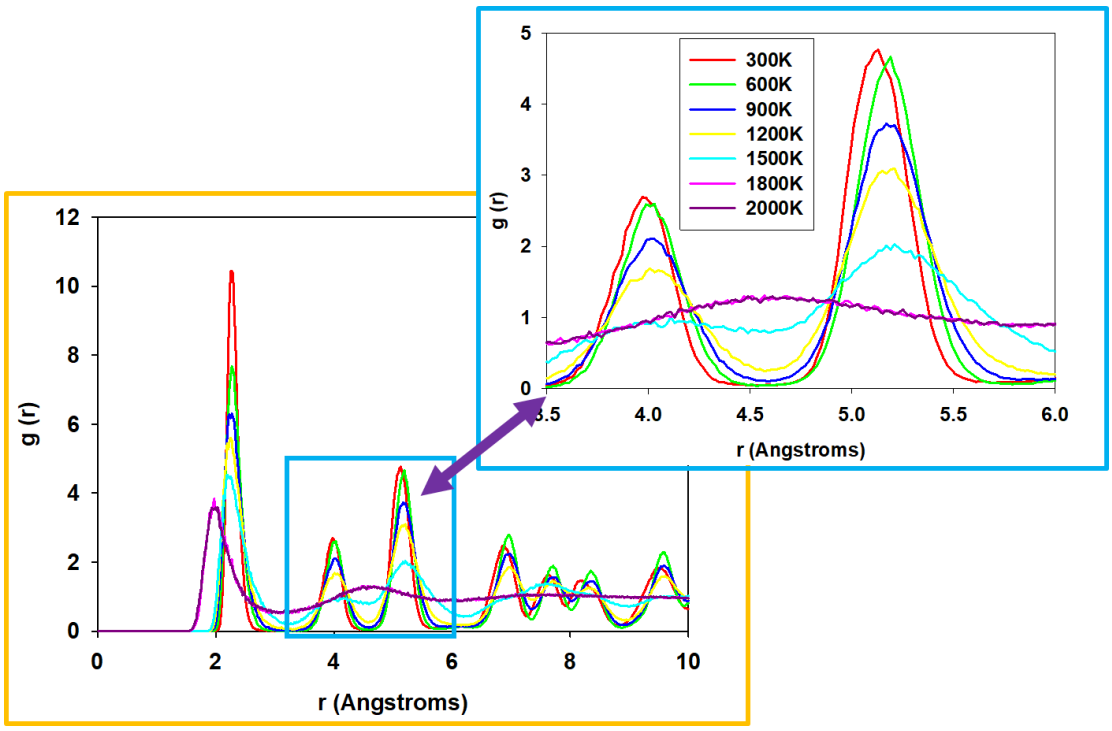

Figure 4.9 the radial distribution function curves for CoO under different temperatures; and the zoomed portion on the top right corner.

4.9 Discussion

The exact comparison of the lattice parameters provided the same equilibrium interatomic distances in the structure. On the other hand, the agreement between elastic constants of NiO provided an average percentage difference of 1.41 % which provides a small difference. Conversely, the CoO elastic constants produced an average percentage difference of 11.66%. The distinctive elastic constants provide smaller curvatures around the equilibrium bond lengths [165].

The fundamental aspect of this section is to derive the forces between the atoms to determine the conditions of the favourable simulation in probing these materials and other relative structures. Moreover, the results are fundamental in the doping process of various compounds. The computational modelling investigations of LMO (M: Ni and Co) are currently based on molecular dynamics simulations. However, the accuracy

of the method is limited by the inability of the method to accommodate thermal effects. As the counterpart to the concern, the empirical interatomic potentials for NiO and CoO crystal structures were derived in the present work, the task possesses challenges in the classical simulation methods [181]. The task is based on nickel and cobalt oxides since the nature of oxides possess complex crystal structures on which theories of thermal conductivity have been based [165]. The published interatomic interactions for LMO (M: Ni and Co) which are fundamental for performing atomic simulation on doped systems were not available, hence they were derived in the present work. The derived interatomic potentials for both NiO and CoO were validated in the bulk form, directed by accurate determination of the calculated lattice parameters and the volume of both structures which compared well to the experimental lattice parameters.

Moreover, the derived interatomic parameters were further validated by their ability to reproduce high-temperature structural change of the NiO and CoO bulk at a relatively adequate temperature as that of the experimental melting temperature for both structures; which compares well to the similar phenomenon observed from Brillouin scattering [182], lattice dynamics [183] and DFT molecular dynamics methods [184].

To further estimations of the melting point of the structures, the change in total energy with temperature was monitored together with radial distribution functions. The calculated radial distribution curves from molecular dynamics simulation provided more evidence of phase change from 2250K and 2000K for NiO and CoO, respectively. It was inferred from the curves that the generated structure for both NiO and CoO had a phase change at a lower temperature than the experimental structures. This was validated by the RDFs with a lower probability of finding the nearest neighbouring atom when the NiO structure is heated at 2250K and when the CoO is heated at 2000K. The stiffness of the materials was detected from the bulk moduli of the structure, with a percentage difference of 19.86% in NiO. The success of the interatomic potentials in large systems was demonstrated by perming the MD calculation with the derived potentials for NiO and CoO on 20 000 atomic nanostructures, respectively.

Chapter 5: Summary and Conclusions

The first principle density functional theory was used to probe the electronic properties of the layered $LiMO_2$ (M: Mn, Ni, and Co) bulk structures. The DFT with Hubbard correction U calculations within the exchange-correlation of GGA-PBE embodied in CASTEP, VASP, and PHONON codes were employed. Three isostructural layered materials with the space group $R\bar{3}m$ were considered in the work. The structures are orthorhombic $LiMnO_2$, $LiNiO_2$, and $LiCoO_2$. The energy and k-mesh configurations were determined to find minimal converging energy and k-points for each structure. Full structure optimisation has been performed on the structures to determine the equilibrium cell parameters. Moreover, the spin polarised local density approximation calculations were performed to calculate the electronic band structure, partial and total density of states, and the phonon dispersion curves.

The DFT+U yields satisfactory predictions of equilibrium lattice constants with a difference of less than 4% in $LiMnO_2$ with 3.96% in volume and less than 1% in $LiNiO_2$ and 0.81% in the volume of the structure and $LiCoO_2$ 2.58% in the volume of the structure. The Hubbard U parameters for $LiMnO_2$, $LiNiO_2$, and $LiCoO_2$ structures correct the electron self-interactions in DFT by localizing electrons in strongly correlated systems [145]. The Hubbard U values together with the low spin transition metal in 3+ charge state (Mn^{3+}, Ni^{3+}, and Co^{3+}) predicts the electrical conductivity of the materials. Hence, they produce band gaps that are in considerable agreement with the experimental data. The bandgap of the $LiMnO_2$ material (1.64 eV) is the same as the bandgap of the $LiMnO_2$ determined experimentally [151]. Conversely, the bandgap of $LiNiO_2$ (0.4 eV) is the same as the experimental band gap of the $LiNiO_2$ determined by Laubach, S. at. al [152]. Lastly, the bandgap of $LiCoO_2$ (2.22) material falls within the experimentally determined range of the $LiCoO_2$ (2.10 -2.27 eV) [153]. The small energy band in $LiNiO_2$ possess high conductivity, and the wide energy bandgaps in $LiMnO_2$ and $LiCoO_2$ possess low conductivity. Hence, the $LiNiO_2$ has a semiconductor characteristic; $LiMnO_2$ and $LiCoO_2$ have an insulator characteristic.

Furthermore, the density of states (DOS), for $LiMnO_2$, $LiNiO_2$, and $LiCoO_2$ structures were calculated to probe their electronic structure behaviour. The partial density of states depicted that, the electron contributions at the Fermi level of all three materials are due to the 3d states of the transition metals and 2s states of the O atoms per

material. The relationship between the DOS and the U value was that when increasing the U value, the contribution of the O 2p states near the Fermi increases, and therefore the occupied and unoccupied bands are more separated, which effectively increases the bandgap of the system, which affects the electronic properties of the structures.

Lastly, the phonon dispersion curves were calculated to evaluate the vibrational stability of the $LiMnO_2$, $LiNiO_2$, and $LiCoO_2$ systems with the same conditions. The phonon curves displayed that the $LiCoO_2$ material is relatively the least stable material with the imaginary frequencies contained in the phonon curves of this material. This is supported by the large bandgap size of the materials determined in the electronic band structures. Conversely, both $LiNiO_2$ and $LiMnO_2$ have no negative vibrations. Moreover, the $LiNiO_2$ material was found to be the most stable, predicted from the heat of formations.

The stability criteria of the materials were determined from the calculated total density of states. The TDOS share a valuable insight that the structure with the highest density of states at the fermi region (E_f) is considered the least stable, whereas the structure with the lowest density of states at E_f is considered most stable [162]. As such, the TDOS brought to attention that the $LiCoO_2$ has the highest density of states at the Fermi level, indicating that the material is comparatively the least stable; the $LiNiO_2$ had the lowest density of state at the Fermi level implying that it is more stable than $LiMnO_2$ and $LiCoO_2$. The total density of states results validates the findings from both band structures and the phonon dispersion curves. Phonon dispersion curves show that the $LiMnO_2$ and $LiNiO_2$ are vibrationally stable inconsistent with their calculated elastic constants, which satisfy all necessary stability criteria. Although the phonon dispersion curves show soft modes in $LiCoO_2$, the predicted heats of formation and elastic constants show that the structure can be thermodynamically favorable. As such, the $LiNiO_2$ material is more vibrationally stable than $LiMnO_2$ and $LiCoO_2$. On the other hand, the $LiCoO_2$ is relatively the least stable material. In conclusion, the DFT+U is a versatile function that provides good all-round performance for the relevant structural and electrical properties benchmarked in this study.

To the good interest of this work, it has been identified that the $LiNiO_2$ with predicted U values, be a recommendable material to perform the NMC doping. This can improve

the electrochemical performance of the Li-ion cathode materials and reduce the structural transformation during cycling.

Moreover, the GULP based script was employed to fit the interatomic potentials based on Buckingham potential. The initial attention is focused on simple cubic structures of NiO and CoO. Several experimental structures, elastic, and lattice dynamic properties which are classified as the key to fitting potentials were not available, hence they were calculated in the present study. The derived interatomic potentials for NiO and CoO were validated in their bulk form as evidenced by their reliable accuracy of determining the output structure, elastic constants, and moduli. The overall properties compared relatively well with the experiment data. However, the GULP script utilised in the study was two-body interaction, as such the C_{12} and C_{44} resulted in the same values. As a counterpart to that, the robustness of the derived interatomic potentials was further demonstrated by their ability to produce a high-temperature transition of 20000 atoms structures for both NiO and CoO. The state change temperature was compared to the experimental melting point of the same structures, which compared well with the acceptable percentage differences.

The change in radial distribution functions, direct observation of the structures, and the total energy with the temperature deduced from molecular dynamics simulations, depicted the material phase changes from low to higher temperatures. The interatomic potentials in NiO structures presented a melting point above 2250K. Conversely, the interatomic potentials for the CoO structure showed a melting point at 2000K. These melting points corresponded from the calculated RDF, atomic structures, and energy with temperature graphs, which were in convincing agreement with the experimental results.

Suggestion for future work

In future work, we intend to employ the parameters driven in this work in a large system of both pure and doped materials and monitor the cycling stability of the doped $LiMO_2$ cathode material. We further intend to carry out the amorphization and recrystallisation to generate a nano structural model of $LiMnO_2$, $LiNiO_2$, $LiCoO_2$, and $LiMn_xNi_yCo_zO_2$ (x+y+z=1) which are crucial for improvement of such cathode material for future lithium-ion battery applications.

References

[1] ByChang, L., Feng, L., Lai-Peng, M., and Hui-Ming, C., "Advanced Materials for Energy Storage," Advanced Energy Materials, 22, 28-62, 2010.

[2] Vikström, H., Davidsson, S. and Höök, M., "Lithium availability and future production outlooks," Applied Energy, 110, 252-266, 2013.

[3] Seo, D.H., Lee, J., Urban, A., Malik, R., Kang, S. and Ceder, G., "The structural and chemical origin of the oxygen redox activity in layered and cation-disordered Li-excess cathode materials," Nature chemistry, 7, 692, 2016.

[4] Ulvestad, A., "A Brief Review of Current Lithium-Ion Battery Technology and Potential Solid State Battery Technologies". 2018

[5] Hausbrand R, Cherkashinin G, Ehrenberg H, Gröting M, Albe K, Hess C, Jaegermann W., "Fundamental degradation mechanisms of layered oxide Li-ion battery," cathode materials: Methodology, insights and novel approaches, 192, 3-25, 2015.

[6] Sun, H. and Zhao, K., "Electronic structure and comparative properties of $LiNi_xMn_yCo_zO_2$ cathode materials.," The Journal of Physical Chemistry C, 121, 6002-6010, 2017.

[7] Tuccillo, M., Palumbo, O., Pavone, M., Muñoz-García, A.B., Paolone, A. and Brutti, S., "Analysis of the Phase Stability of $LiMO_2$ Layered Oxides (M= Co, Mn, Ni)," Crystals, 10, 526, 2020.

[8] Chakraborty, A., Dixit, M. and Major, D.T., "Accurate Cathode Properties of $LiNiO_2$, $LiCoO_2$, and $LiMnO_2$ Using the SCAN Meta-GGA Density Functional," 2018.

[9] Noh, H.J., Youn, S., Yoon, C.S. and Sun, Y.K., "Comparison of the structural and electrochemical properties of layered Li $[Ni_xCo_yMn_z]O_2$ (x=1/3, 0.5, 0.6, 0.7, 0.8

and 0.85) cathode material for lithium-ion batteries," Journal of power sources, 233, 120-130, 2013.

[10] Deng, D., "Li-ion," Energy Science and Engineering, 3, 385-478, 2015.

[11] Liu, C., Neale, Z.G. and Cao, G., "Understanding electrochemical potentials of cathode materials in rechargeable batteries," Materials Today, 19, 109-123, 2016.

[12] Li, T., Li, X., Wang, Z. and Guo, H.,, "A short process for the efficient utilization of transition-metal chlorides in lithium-ion batteries: a case of $Ni_{0.8}Co_{0.1}Mn_{0.1}O_1$ and $LiNi_{0.8}Co_{0.1}Mn_{0.1}O_2$," Journal of Power Sources, 342, 765-503, 2017.

[13] Wu, E.J., Tepesch, P.D. and Ceder, G., "Size and charge effects on the structural stability," PHILOSOPHICAL MAGAZINE B, 77, 1039-1047, 1998.

[14] Shi-xi, Z., Han-xing, L., Shi-xi, O. and Qiang, L., "Synthesis and performance of $LiMnO_2$ as cathodes for Li-ion batteries," Journal of Wuhan University of Technology-Mater. Sci. Ed., 18, 5-8, 2003.

[15] Wu, E.J., Tepesch, P.D. and Ceder, G., "Size and charge effects on the structural stability of $LiMO_2$ (M= transition metal) compounds," Philosophical Magazine B, 77, 1039-1047, 1998.

[16] Mishra, S.K. and Ceder, G., "Structural stability of lithium manganese oxides," Physical Review B, 59, 6120, 1999.

[17] Wu, E.J., Tepesch, P.D. and Ceder, G, "Size and charge effects on the structural stability of $LiMO_2$ (M= transition metal) compounds," Philosophical Magazine B, 77, 1039-1047, 1998.

[18] Jang, Y.I., Moorehead, W.D. and Chiang, Y.M., "Synthesis of the monoclinic and orthorhombic phases of $LiMnO_2$ in oxidizing atmosphere," Solid State Ionics, 149, 201-207, 2002.

[19] Jang, Y.I. and Chiang, Y.M, "Stability of the monoclinic and orthorhombic phases of $LiMnO_2$ with temperature, oxygen partial pressure, and Al doping.," Solid State Ionics, 130, 53-59, 2000.

[20] Orman, H.J. and Wiseman, P.J., "Cobalt (III) lithium oxide, $CoLiO_2$: structure refinement by powder neutron diffraction," Acta Crystallographica Section C, 2, 12-14, 1984.

[21] Ceder, G. and Mishra, S.K., "The Stability of Orthorhombic and Monoclinic-Layered $LiMnO_2$," Electrochemical and solid-state letters, 2, 550-552, 1999.

[22] Wu, L., Lee, W.H. and Zhang, J., "First principles study on the electrochemical, thermal and mechanical properties of $LiCoO_2$ for thin film rechargeable battery," Materials Today: Proceedings,1, 82-93, 2014.

[23] Ohzuku, T. and Makimura, Y., "Layered lithium insertion material of $LiCo_{1/3}Ni_{1/3}Mn_{1/3}O_2$ for lithium-ion batteries," Chemistry Letters, 30, 642-643, 2001.

[24] Lee, M.H., Kang, Y.J., Myung, S.T. and Sun, Y.K., "Synthetic optimization of Li $[Ni_{1/3}Co_{1/3}Mn_{1/3}]O_2$ via co-precipitation," Electrochimica Acta, 50, 939-948, 2004.

[25] Kim, J.M. and Chung, H.T., "Role of transition metals in layered Li [Ni, Co, Mn]O_2 under electrochemical operation," Electrochimica Acta, 49, 3573-3580, 2004.

[26] Lee, M.H., Kang, Y.J., Myung, S.T. and Sun, Y.K., "Synthetic optimization of Li $[Ni_{1/3}Co_{1/3}Mn_{1/3}]O_2$ via co-precipitation," Electrochimica Acta, 50, 939-948, 2004.

[27] Liu, B., Xu, B., Wu, M.S. and Ouyang, C.Y., "First-principles GGA+ U Study on Structural and Electronic Properties in $LiMn_{0.5}Ni_{0.5}O_2$, $LiMn_{0.5}Co_{0.5}O_2$ and $LiCo_{0.5}Ni_{0.5}O_2$," International Journal of Electrochemical Science, . 11, 2016.

[28] Nakai, I., Takahashi, K., Shiraishi, Y., Nakagome, T. and Nishikawa, F., "Study of the Jahn–Teller Distortion in $LiNiO_2$, a Cathode Material in a Rechargeable Lithium Battery, byin SituX-Ray Absorption Fine Structure Analysis," Journal of solid state chemistry, 140, 145-148, 1998.

[29] Park, K.S., Cho, M.H., Park, S.H., Nahm, K.S., Sun, Y.K., Lee, Y.S. and Yoshio, M., "The effects of Ni and Li doping on the performance of lithium manganese oxide material for lithium secondary batteries," Electrochimica acta, 47, 2937-2942, 2002.

[30] Ko, S., Lee, S.C., Lee, C.W. and Im, J.S., "A Co-free layered $LiNi_{0.7}Mn_{0.3}O_2$ cathode material for high-energy and long-life lithium-ion batteries," Journal of Alloys and Compounds, 613, 96-101, 2014.

[31] Zhong, S.K., Wei, L., ZUO, Z.G., Xin, T.A.N.G. and LI, Y.H., "Synthesis and electrochemical performances of $LiNi_{0.6}Co_{0.2}Mn_{0.2}O_2$ cathode materials," Transactions of Nonferrous Metals Society of China, 19, 1499-503, 2009.

[32] Chakraborty, A., Dixit, M. and Major, D.T., "Accurate Cathode Properties of $LiNiO_2$, $LiCoO_2$, and $LiMnO_2$ Using the SCAN Meta-GGA Density Functional," 2018.

[33] Park, K.S., Cho, M.H., Park, S.H., Nahm, K.S., Sun, Y.K., Lee, Y.S. and Yoshio, M., "The effects of Ni and Li doping on the performance of lithium manganese oxide material for lithium secondary batteries," Electrochimica Acta, 47, 2937-2942, 2002.

[34] P. Education, "Band Gap," 26 September 2015. [Online]. Available: http://www.pveducation.org/pvcdrom/pn-junction/band-gap. [Accessed 16 January 2021].

[35] "Band Theory of Solids," HyperPhysics, 26 September 2015. [Online]. Available: http://hyperphysics.phy-astr.gsu.edu/hbase/solids/band.html. [Accessed 16 January 2021].

[36] "Wikimedia Commons," 26 September 2015. [Online]. Available: Band Gap Comparison.

[37] "HyperPhysics," Conductor Energy Bands, 26 September 2015. [Online]. Available: http://hyperphysics.phy-astr.gsu.edu/hbase/solids/band.html#c6.

[38] "HyperPhysics," Semiconductor Energy Bands, 26 September 2015. [Online]. Available: http://hyperphysics.phy-astr.gsu.edu/hbase/solids/band.html#c5.

[39] Yue, P., Wang, Z., Peng, W., Li, L., Guo, H., Li, X., Hu, Q. and Zhang, Y., "Preparation and electrochemical properties of submicron $LiNi_{0.6}Co_{0.2}Mn_{0.2}O_2$ as cathode material for lithium ion batteries," Scripta materialia, 65, 1077-1080, 2011.

[40] Li, L.J., Li, X.H., Wang, Z.X., Guo, H.J., Yue, P., Chen, W. and Wu, L., "A simple and effective method to synthesize layered $LiNi_{0.8}Co_{0.1}Mn_{0.1}O_2$ cathode materials for lithium ion battery," Powder Technology, 206, 353-357, 2011.

[41] Wu, E.J., Tepesch, P.D. and Ceder, G., "Size and charge effects on the structural stability of," PHILOSOPHICAL MAGAZINE B, 77, 1039-1047, 1998.

[42] Liu, B., Xu, B., Wu, M.S. and Ouyang, C.Y., "First-principles GGA+U Study on Structural and Electronic Properties in $LiMn_{0.5}Ni_{0.5}O_2$, $LiMn_{0.5}Co_{0.5}O_2$ and $LiCo_{0.5}Ni_{0.5}O_2$," International Journal of ELECTROCHEMICAL science, 11, 432 - 445, 2016.

[43] "Defect Chemistry in Layered $LiMO_2$ (M = Co, Ni, Mn, and $Li_{1/3}Mn_{2/3}$) by First-Principles Calculations," Chemistry of materials, 24, 3886−3894, 2012.

[44] Kwon, N.H. and Fromm, K.M., "Enhanced Electrochemical Performance of <30," Food Chem, 133, 38-44, 2012.

[45] Aydinol, M. K, Kohan, S. F. Ceder, G. Cho, K. and Joannopoulos, J., Physics Review B, 56, 1354, 1997.

[46] Huang, Z. F., Meng, X. Wang, C. J., Sun, Y. and Chen, G., Journal of Power Sources, 158, 1394, 2006.

[47] Amriou, T., Khelifa, B., Aourag, H., Aouadi, S.M., and Mathieu, C., Materials chemistry and physics, 92, 499-504, 2005.

[48] Blundell, S.J. and Blundell, K.M., Concepts in Thermal Physics, 2nd ed, New : Oxford University Press, 2010.

[49] Kittel, C., Introduction to Solid States Physics, New york: Wiley, 2004.

[50] Carson, J.S., "Introduction to modeling and simulation," in InProceedings of the Winter Simulation Conference, 8, 2005.

[51] Kitchenham, B. and Brereton, P., "A systematic review of systematic review process research in software engineering," Information and software technology, 55, 2049-2075, 2013.

[52] Hoang, K., Lee, M.S., Mahanti, S.D. and Jena, P., "Clusters: An Embryonic Form of Crystals and Nanostructures," In Science and Technology of Atomic, Molecular, Condensed Matter & Biological Systems, 1, 37-70, 2010.

[53] Payne, M.C., Teter, M.P., Allan, D.C., Arias, T.A. and Joannopoulos, A.J., "Iterative minimization techniques for ab initio total-energy calculations: molecular dynamics and conjugate gradients," Reviews of modern physics, 64, 1045, 1992.

[54] Jayaraman, A., "Diamond anvil cell and high-pressure physical investigations," Reviews of Modern Physics, 55, 65, 1983.

[55] Thomas, L.H., "The Calculation of Atomic Fields," In Mathematical proceedings of the Cambridge philosophical society, 23, 542-548, 1927.

[56] Fermi, E, “Fermi E. Statistical method to determine some properties of atoms," Rend. Accad. Naz. Lincei, 6, 602-607, 1927.

[57] Hohenberg, P. and Kohn, W., "Inhomogeneous Electron gas," Physical review, 136, 871, 1964.

[58] Kohn, W. and Sham, L.J., "Self-Consistent Equations Including Exchange and Correlation Effects," Physical review, 140, A1133, 1965.

[59] Evarestov, R.A., "The LCAO First-Principles Treatment of Crystals," Quantum Chemistry of Solids, 153, 232, 2007.

[60] Parr, R.G., and Yang, W.T., "Density-Functional Theory of Atoms and Molecules," Oxford University Press,5-15, 1994.

[61] Koch, W., Holthausen, M.C. and Kaupp, M., "A Chemist’s Guide to Density Functional Theory, 2nd ed," Willey-VCH, 113, 989-989, 2001.

[62] Sham, L.J. and Kohn, W., "One-Particle Properties of an Inhomogeneous Interacting Electron Gas," Physical Review, 145, 531, 1966.

[63] Mattsson, A.E., Schultz, P.A., Desjarlais, M.P., Mattsson, T.R. and Leung, K., "Designing Meaningful Density Functional Theory Calculations in Materials," Modelling and Simulation in Materials Science and Engineering, 13, 1, 2005.

[64] Zhang H. and Banfield J.F., "Aggregation, coarsening, and phase transformation in ZnS nanoparticles studied by molecular dynamics simulations.," Nano Letters, 4, 713–718, 2004.

[65] Cai W., Li J. and Yip S., "Chapter 128 Molecular Dynamics," Comprehensive Nuclear Materials, 1-36, 2010.

[66] Allen M.P., "Introduction to Molecular Dynamics Simulation," Computational Soft Matter, 23, 1-28, 2004.

[67] Atkins P. W., Physical Chemistry 6th Edition, Oxford : Oxford University Press, 1998.

[68] "Molecular Simulation," WIKIBOOKS, [Online]. Available: https://en.wikibooks.org/wiki/Molecular_Simulation/Thermodynamic_ensembles. [Accessed 17 January 2021].

[69] Hernández, E.R., "Molecular Dynamics: from basic techniques to applications (A Molecular Dynamics Primer)", 1077, 95-123, 2008.

[70] Allen M.P., and Tildesley D.J., Computer Simulation of Liquids, Oxford: Clarendon Press, 1987.

[71] D. L. R.S, "PHD Thesis," 2015.

[72] Catlow C. R. A., Ackermann L., Bell R. G., Corà F. , Gay C.D. H., Nygren M. A., J. C. Pereira,G. Sastre, C.B. Slater and P.E. Sinclair, "Computer Modelling as a technique in solid state chemistry," Faraday Discussions, 92, 433, 1997.

[73] Mkhonto D, "PhD Thesis," University of Limpopo, 2005.

[74] Gale, J., "GULP manual," 1998.

[75] Smith W. and Forester T.R., "DL_POLY_2. 0: A general-purpose parallel molecular dynamics simulation package," Journal of molecular graphics, 14, 136-141, 1996.

[76] Powers, J.M. and Sen, M., "Mathematical Methods in Engineering," 219-279, 2015.

[77] Chakraverty, M., Kittur, H.M. and Kumar, P.A., "First Principle Simulations of Various Magnetic Tunnel Junctions for Applications in Magnetoresistive Random Access Memories," IEEE Trans. Nanotechnol, 12, 975, 2013.

[78] Horn, K., and Scheffler, M., "In Electronic Structure (Handbook of Surface Science)," 2, 2000.

[79] Robert, G.P., and Weitao, Y.,"Density-Functional Theory of Atoms and Molecules," 1994.

[80] Dirac, P., "Note on Exchange Phenomena in the Thomas-Fermi Atom," Mathematical proceedings of the Cambridge philosophical society, 26, 376-385, 1930.

[81] Dreizler, R.M. and Gross, E.K., Gross, "Density Functional Theory," 1990.

[82] Yang, W. and Parr, R.G., "Density Functional Theory of Atoms and Molecules," 1989.

[83] Vosko, S.H., Wilk, L. and Nusair, M., "Accurate Spin-Dependent Electron Liquid Correlation Energies for Local Spin Density Calculations: A Critical Analysis," Canadian Journal of physics, 58, 1200-1211, 1980.

[84] Perdew, J.P., and Zunger, A., "Self-Interaction Correction to Density-Functional Approximations for Many-Electron Systems," Physical Review B, 23, 5048, 1981.

[85] Perdew, J.P. and Wang, Y., "Accurate and Simple Analytic Representation of the Electron Gas Correlation Energy," Physical Review B, 45, 13244, 1992.

[86] Perdew, J.P. and Wang, Y., "Erratum: Accurate and simple analytic representation of the electron-gas correlation energy," Physical Review B, 98, 079904, 2018.

[87] Geldart, D.J.W. and Rasolt, M., "Exchange and Correlation Energy of an Inhomogeneous Gas at Metallic Densities," Physical Review B, 13, 1477, 1976.

[88] Perdew, J., "Generalized Gradient Approximations for Exchange and Correlation: A Look Forward and Backward," Physical Review B, 172, 6, 1991.

[89] Politzer, P., and Seminario, J.M., "Modern Density Functional Theory: A Tool for Chemistry," 1995.

[90] Becke, A., "Density-functional Exchange-Energy Approximation with Correct Asymptotic Behaviour," Physical review A, 38, 3100, 1988.

[91] Perdew, J., "Density-Functional Approximation for the Correlation Energy of the Inhomogeneous Electron Gas," Physical review B, 33, 8824, 1986.

[92] Perdew, J.P., and Wang, Y., "Accurate and Simple Density Functional for the Electronic Exchange Energy: Generalized Gradient Approximation," Physical review B, 33, 8800, 1986.

[93] Perdew, J.P., Ziesche, P. and Eschrig, H., "In Electronic Structure of Solids," 1991.

[94] M.C. Payne, M.P. Teter, D.C. Allan, T.A. Arias, and J.D. Joannopoulos, ""Iterative Minimization Techniques for Ab ilitio Total-Energy Calculations: Molecular Dynamic and Conjugate Gradients," Physical review, 64, 1045, 1992.

[95] Meyer, B., "The Pseudopotential Plane Wave Approach," NIC Series, 31, 71-83, 2006.

[96] Ashcroft, N.W., and Mermin, N.D. "On Introductory Concepts," Solid State Physics, 1976.

[97] Blakemore, J.S. "Solid State Physics, 2nd ed," 1985.

[98] Phillips, J.C. and Kleinman, L., "New Method for Calculating Wave Functions in Crystal and Molecules," Physical Review, 116, 287, 1959.

[99] Cohen, M.L. and Heine, V., "The Fitting of Pseudopotentials to Experimental Data and their Subsequent Application," Solid State Physics, 24, 37, 1970.

[100] Hellmann, H., "A New Approximation Method in the Problem of Many Electrons," The Journal of Chemical Physics, 3, 61-61, 1935.

[101] Pickett, W.E., "Pseudopotential Methods in Condensed Matter Applications," Computer Physics Reports, 9, 97-115, 1989.

[102] Heine, V., "The Pseudopotential Concept," Solid State Physics (Academic Press), 24, 1-36, 1970.

[103] Brust, D.A.V.I.D. and Alder, B., "The Pseudopotential Method and the Single-Particle Electronic Excitation Spectra of Crystals, Methods in Computational Physics," Academic Press, 8, 61, 1968.

[104] Harrison, W.A., "Pseudopotentials in the Theory of Metals, Frontiers in Physics," 1966.

[105] Srivastava, G.P. and Weaire, D., "The Theory of the Cohesive Energies of Eolids," Advances in Physics, 26, 463-517, 1987.

[106] Bachelet, G.B., Hamann, D.R. and Schlüter, M., "Pseudopotentials that Work: From H to Pu," Physical Review B, 26, 1494, 1982.

[107] Hamann, D.R., Schlüter, M. and Chiang, C., "Norm-Conserving Pseudopotentials," Physical Review Letters, 43, 1494, 1979.

[108] Hamann, D.R., "Generalised Norm-conserving Pseudopotentials," Physical Review B, 40, 2980, 1989.

[109] Kresse, G., Marsman, M. and Furthmüller, J., "VASP the GUIDE, Computational Physics," 8, 2009.

[110] Parlinski, K., Li, Z.Q. and Kawazoe, Y., "First-Principles Determination of the Soft Mode in Cubic ZrO_2," Physical Review Letters, 78, 4063, 1997.

[111] [Online]. Available: http://www.materialsdesign.com..

[112] Vanderbilt, D., "Soft Self-Consistent Pseudopotentials in Generalized Eigenvalue Formalism," Physical review B, 41, 7892, 1990.

[113] Lethole, N.L., " Computer Modelling Studies of MPO_4, $LiMPO_4$ and $NaMPO_4$ (M: Fe, Co, Mn) Polymorphs (Doctoral dissertation, University of Limpopo)," 2016.

[114] Inoshita, T., Nakao, K. and Kamimura, H., "Electronic Structure of PotassiumGraphite Intercalation Compound: C8K," Journal of the Physical Society of Japan, 43, 1237-1243, 1977.

[115] Bancel, P.A. and Heiney, P.A., "Icosahedral Aluminum-Transition Metal Alloys," Physical Review B, 88, 7917, 1986.

[116] Matsuda, T., Ohara, I., Sato, H., Ohashi, S. and Mizutani, U., "Electronic Properties for Icosahedral and Amorphous Phases in the Mg-Zn-Al Alloy," J. Journal of Physics: Condensed Matter, 1, 4087, 1989.

[117] Gornostyrev, Y.N., Kontsevoi, O.Y., Maksyutov, A.F., Freeman, A.J., Katsnelson, M.I., Trefilov, A.V. and Lichtenshtein, A.I., "Negative Yield Stress Temperature Anomaly and Structural Istability of Pt3Al," Physical Review B, 70, 014102, 2004.

[118] Pankhurst, D.A., Nguyen-Manh, D. and Pettifor, D.G., "Electronic Origin of Structural Trends Across Early Transition-Metal Disilicides: Anomalous Behaviour of $CrSi_2$," Physical Review B, 69, 075113, 2004.

[119] Harald, I., and Lüth, H., "Solid-State Physics: An Introduction to Principles of Materials Science 2nd ed," 1996.

[120] Vasileska, D., Goodnick, S.M. and Klimeck, G., "Computational Electronics: Semiclassical and Quantum Device Modelling and Simulation," 2010.

[121] Zhou, Z. and Joós, B., "Stability Criteria for Homogeneously Stressed Materials and the Calculation of Elastic Constants," Physical Review B, 54, 3850, 1996.

[122] Beckstein O, Klepeis JE, Hart GL, Pankratov O, "First-Principles Elastic Constants and Electronic Structure of α-Pt_2Si and PtSi," Physical Review B, 63, 134112, 2001.

[123] Born, M. and Huang, K., "Dynamical Theory of Crystal Lattices," Acta Cryst, 9, p. 837, 1956.

[124] Hill, R., Hopkins, H. G., and Sewell, M. J., "Mechanics of Solids 1st ed," 1982.

[125] Tang, M. and Yip, S., "Lattice Instability in β-SiC and Simulation of Brittle Fracture," Journal of applied physics, 76, 2719-2725, 1994.

[126] Barron, T.H.K. and Klein, M.L., "Second-Order Elastic Constants of a Solid under Stress," Proceedings of the Physical Society, 85, 523, 1965.

[127] Wang, J., Li, J., Yip, S., Phillpot, S. and Wolf, D., "Mechanical Instabilities of Homogeneous Crystals," Physical Review B, 52, 627, 1995.

[128] St.-Amant, A., Cornell, W.D., Kollman, P.A. and Halgren, T.A., "A Study of Geometries, Conformational Energies, Dipole Moments and Electrostatic Potential Fitted Charges Using Density Functional Theory," Journal of computational chemistry, 16, 1483-1506, 1995.

[129] Kittle, C., "Introduction to Solid State Physics, 5th ed," 1976.

[130] Cohen, M.L., "Calculation of Bulk Moduli of Diamond and Zinc-Blende Solids," Physical Review B, 32, 7988, 1985.

[131] Pugh, S.F., "Relations Between Elastic Moduli and Plastic Properties of Polycrystalline Pure Metals," Philosophical Magazine and Journal of Science, 45, 823-843, 1954.

[132] Goumri-Said, S. and Kanoun, M.B., "Theoretical Investigations of Structural, Elastic, Electronic and Thermal Properties of Damiaoite $PtIn_2$," Computational materials science, 43, 243-250, 2008.

[133] Mayer, B., Anton, H., Bott, E., Methfessel, M., Sticht, J. and Schmidt, P.C., "The Elastic Anisotropy of Crystals," Journal of Physics., 38, 256-296, 2010.

[134] Langreth, D.C. and Perdew, J.P., "The Exchange Correlation Energy of a Metallic Surface," Solid State Communications, 17, 1425-1429, 1975.

[135] Wacker, A., "An Introduction to theConcept of Band Structure," 20 Noveber 2018.

[136] Ulvestad, A., "A Brief Review of Current Lithium Ion Battery Technology and Potential Solid State Battery Technologies," 2018.

[137] Hoang, K. and Johannes, M.D., "Defect chemistry in layered transition-metal oxides from screened hybrid density functional calculations," Journal of Materials Chemistry A, 2, 5224-5235, 2014.

[138] Tuccillo, M., Palumbo, O., Pavone, M., Muñoz-García, A.B., Paolone, A. and Brutti, S., "Analysis of the Phase Stability of $LiMO_2$ Layered Oxides (M= Co, Mn, Ni)," Crystals, 10, 526, 2020.

[139] Hirota K, Nakazawa Y and Ishikawa M, J. Phys.: Condens. Matter, 3, 4721-4730, 1991.

[140] Tian, S, " Materials Physical Properties.," 2004.

[141] Armstrong, A.R., Dupre, N., Paterson, A.J., Grey, C.P. and Bruce, P.G., " Combined neutron diffraction, NMR, and electrochemical investigation of the layered-to-spinel transformation in $LiMnO_2$," Chemistry of materials, 16, 3106-3118, 2004.

[142] Hoang, K. and Johannes, M.D., "Defect physics in complex energy materials," Journal of Physics: Condensed Matter, 29, 293001, 2018.

[143] Arroyo y de Dompablo M.E., Biskup N., Gallardo-Amores J.M., Moran E., Ehrenberg H., and Amador U., "Gaining Insights into the Energetics of FePO4 Polymorphs," Chemistry of Materials, 3, 994-1001, 2010.

[144] M.D. Segall, P. J.D. Lindan, M.J. Probert, C.J. Pickard, P.J. Hasnip, S.J. Clark, "“First-principles simulation: ideas, illustrations and the," Journal of physics: condensed matter, 14, 2744, 2002.

[145] Anisimov, V.I., Zaanen, J. and Andersen, O.K., "and theory and Mott insulators: Hubbard U instead of Stoner I," Physical Review B, 3, 943, 1991.

[146] Zhou, F., Cococcioni, M., Marianetti, C.A., Morgan, D. and Ceder, G., "First-principles prediction of redox potentials in transition-metal compounds with LDA+ U," Physical Review B, 23, 235121, 2004.

[147] Singh, V., Kosa, M., Majhi, K. and Major, D.T., "Putting DFT to the test: a first-principles study of electronic, magnetic, and optical properties of Co_3O_4," Journal of chemical theory and computation, 1, 64-72, 2014.

[148] Hellmann, H., " A new approximation method in the problem of many electrons," The Journal of Chemical Physics, 3, 61-61, 1935.

[149] Miyashiro, H., Yamanaka, A., Tabuchi, M., Seki, S., Nakayama, M., Ohno, Y., Kobayashi, Y., Mita, Y., Usami, A. and Wakihara, M., "Improvement of

degradation at elevated temperature and at high state-of-charge storage by ZrO_2 coating on $LiCoO_2$," Journal of the Electrochemical Society, 153, A348, 2005.

[150] Chakraborty, A., Dixit, M. and Major, D.T., "Accurate Cathode Properties of $LiNiO_2$, $LiCoO_2$, and $LiMnO_2$ Using the SCAN Meta-GGA Density Functional," 2018.

[151] Kong, F., Longo, R.C., Park, M.S., Yoon, J., Yeon, D.H., Park, J.H., Wang, W.H., Santosh, K.C., Doo, S.G. and Cho, K., "Ab initio study of doping effects on $LiMnO_2$ and Li_2MnO_3 cathode materials for Li-ion batteries," Journal of Materials Chemistry A, 16, 8489-8500, 2015.

[152] Laubach, S., Laubach, S., Schmidt, P.C., Ensling, D., Schmid, S., Jaegermann, W., Thißen, A., Nikolowski, K. and Ehrenberg, H., "Changes in the crystal and electronic structure of $LiCoO_2$ and $LiNiO_2$ upon Li intercalation and de-intercalation," Physical Chemistry Chemical Physics, 17, 3278-3289, 2009.

[153] Van Elp, J., Wieland, J.L., Eskes, H., Kuiper, P., Sawatzky, G.A., De Groot, F.M.F. and Turner, T.S., "Electronic structure of CoO, li-doped CoO, and $LiCoO_2$," Physical Review B, 12, 6090, 1991.

[154] De Jong, M., Chen, W., Angsten, T., Jain, A., Notestine, R., Gamst, A., Sluiter, M., Ande, C.K., Van Der Zwaag, S., Plata, J.J. and Toher, C.," Charting the complete elastic properties of inorganic crystalline compounds" Scientific data, 2, 1-13, 2015.

[155] Tanaka, K. & Koiwa, M, " Single-Crystal Elastic Constants of Intermetallic Compounds," Intermetallics, 4, 29-39, 1996.

[156] Chen, H.S., "Anisotropy of elasticity about metal," Metal-lurgy Industry Press, Beijing,1996.

[157] Tian, S.K., Chen, Y., Hang, J., Tang, L., McDaid, P. and Deng, L., “Asymmetric organic catalysis with modified cinchona alkaloids", 37, 621-631, 2004.

[158] Zhang, L.Q., Cheng, Y. and Niu, Z.W., "Elastic Properties and Phonon Dispersion," J. At. Mol. Sci, 5, 81-94, 2014.

[159] Fast, L., Wills, J.M., Johansson, B. and Eriksson, O., "Elastic Constants of Hexagonal Transition Metals: Theory," Physical Review B, 51, 17431, 1995.

[160] Gaillac, R., Pullumbi, P. and Coudert, F.X., "LATE: an open-source online application for analysis and visualization of elastic tensors," Journal of Physics: Condensed Matter, 28, 275201, 2016.

[161] Cheng, E.J., Taylor, N.J., Wolfenstine, J. and Sakamoto, J., "Elastic properties of lithium cobalt oxide ($LiCoO_2$)," Journal of Asian Ceramic Societies, 5, 113-117, 2017.

[162] H. Chauke, " PhD Thesis," University of Limpopo, 26, 2005.

[163] Anisimov, V.I., Korotin, M.A. and Kurmaev, E.Z., "Anisimov, V.I., Korotin, M.A. and Kurmaev, E.Z., 1990. Band-structure description of mott insulators (NiO, MnO, FeO, CoO)," Journal of Physics: Condensed Matter, 17, 3973, 1990.

[164] Adebambo, P.O., Adetunji, B.I., Olowofela, J.A., Oguntuase, J.A. and Adebayo, G.A., "Structural, Electronic, Magnetic and Optical Properties of Ni, Ti/Al-based Heusler Alloys: A First-Principles Approach," Zeitschrift für Naturforschung A, 2, 129-134, 2016.

[165] Tada M., Yoshiya M. and Yasuda H., "Derivation of interatomic potentiasl from Ab-initio calculations for molecular dynamics simulations of Na_xCoO_2.," Tranactions of the Materials research Society of Japan, 2, 205-208, 2010.

[166] Fisher, C.A., "Molecular dynamics simulations of reconstructed NiO surfaces," Scripta Mat., 50, 1045-1049, 2004.

[167] C. Fisher, "Molecular dynamics simulations of reconstructed NiO surfaces," Scripta materialia, 50, 1045-1049, 2004.

[168] Gale, J., "GULP: A computer program for the symmetry-adapted simulation of solids," Journal of the Chemical Society, Faraday Transactions, 93, 629-637, 1997.

[169] Clendenen, R.L. and Drickamer, H.G., "Lattice parameters of nine oxides and sulfides as a function of pressure," The Journal of Chemical Physics, 44, 223-4228., 1966.

[170] Leineweber, A., Jacobs, H. and Hull, S., "Ordering of nitrogen in nickel nitride Ni_3N determined by neutron diffraction," Inorganic chemistry, 40, 5818-5822, 2001.

[171] Jifang, W., Fisher, E.S. and Manghnzmi, M.H., "Elastic constants of nickel oxide," Chinese Physics Letters, 8, 153, 1991.

[172] Wyckoff, R., "Interscience publishers, new york, new york rocksalt structure," Crystal structures, 1, 85-237, 1963.

[173] Wdowik, U.D. and Parlinski, K., " Lattice dynamics of CoO from first principles," Physical Review B, 75, 104306, 2007.

[174] Toennies, J., "On the validity of a modified Buckingham potential for the rare gas dimers at intermediate distances," Chemical Physics Letters, 20, 238-241, 1973.

[175] Gale, J.D. and Rohl, A.L., "The General Utility Lattice Program (GULP)," Molecular Simulation, 5, 291-341, 2003.

[176] Smith, W., Forester, T.R., Todorov, I.T. and Leslie, M., "The DL poly 2 user manual," 2006.

[177] Uchida, N. and Saito, S, "Elastic constants and acoustic absorption coefficients in MnO, CoO, and NiO single crystals at room temperature," The Journal of the Acoustical Society of America, 51, 1602-1605, 1972.

[178] Greenwood, Norman N.; Earnshaw, Alan, "Chemistry of the Elements," 1336–1337, 1984.

[179] Antoch, J., Hanousek, J., Horváth, L., Hušková, M. and Wang, S., "Structural breaks in panel data: Large number of panels and short length time series," Econometric Reviews, 38, 828-855, 2018.

[180] Krishnamachari, N. and Calvo, C., " Crystallographic studies of cobalt arsenates, I. Crystal structure of $Co_3(AsO_4)_2$", Canadian Journal of Chemistry, 48, 881-889, 1970.

[181] Atkinson, K.J.W., Atomic scale simulation of defects in bulk materials and monolayer surfaces, PhD Thesis, University of London, 2002.

[182] Mjwara, P.M., Comins, J.D., Ngoepe, P.E., Buhrer, W. and Bill, H., "Brillouin scattering investigation of the high temperature diffuse phase transition in Li_2S," Journal of Physics: Condensed Matter, 3, 4289, 1992.

[183] Bertheville, B., Bill, H. and Hagemann, H., “Experimental Raman scattering investigation of phonon anharmonicity effects in Li_2S," Journal of Physics: Condensed Matter, 10, 2155, 1998.

[184] Jand, S.P., Zhang, Q. and Kaghazchi, P., "Theoretical study of superionic phase transition in Li_2S," Scientific reports, 1-6, 5873, 2017.

[185] Born, M. and Huang, K., Dynamical Theory of Crystal Lattices, Oxford: Clarendon Press, 1954.

[186] H. Chauke, " PhD Thesis," University of Limpopo, 26, 2005.

[187] Bartell, L.S., "Molecular Geometry: Bonded Versus Nonbonded interactions," Journal of Chemical Education, 45, 754, 1968.

[188] Laubach, S., Laubach, S., Schmidt, P.C., Ensling, D., Schmid, S., Jaegermann, W., Thißen, A., Nikolowski, K. and Ehrenberg, H., "Changes in the crystal and electronic structure of $LiCoO_2$ and $LiNiO_2$ upon Li intercalation and de-intercalation," Physical Chemistry Chemical Physics, 17, 3278-3289, 2009.

[189] Croguennec, L., Deniard, P., Brec, R. and Lecerf, A., "Nature of the stacking faults in orthorhombic $LiMnO_2$," Journal of Materials Chemistry, 3, 511-516, 1997.

Outputs

Conference Presentations

N. Tsebesebe, K. Kgatwane, R.S. Ledwaba, and P.E. Ngoepe, “Atomistic simulation studies of layered $LiMnO_2$ nanospherical cathode materials”, South African Institute of Physics, 64th Annual Conference, July 2019, Polokwane

N.T. Tsebesebe, K.M. Kgatwane, R.S. Ledwaba and PE Ngoepe, “Atomistic Simulation of Nanospherical o-$LiMnO_2$ Cathodes Materials”, Faculty of Science and Agriculture Research Conference, September 2019, Polokwane

N. Tsebesebe, R.S. Ledwaba and P.E. Ngoepe, “First principle investigation of structural and electronic properties of $LiMO_2$ (M: Mn, Ni, Co) as potential cathode materials: A DFT+U study”, Annual Conference for High Performance Computing, December 2019, Boksburg.

N. Tsebesebe, K.M. Kgatwane, R.S. Ledwaba and P.E Ngoepe, “Structural investigation of pure $LiMnO_2$ and Li-Rich $Li_{1.2}Mn_{0.8}O_2$ cathode materials for Li-Ion batteries: An Atomistic Simulation Study”, International Conference on Defects in Insulating Materials, November 2020. An online conference hosted by the Federal University of Sergipe, Brazil.

Publication

N.T. Tsebesebe, K.M. Kgatwane, R.S. Ledwaba and P.E. Ngoepe, “Investigating the structural and electronic properties of $LiMO_2$ (M: Mn, Ni, Co) as potential cathode materials: A DFT study”, Submitted to Institute of Physics Conference Series: Materials Science Engineering